Thermodynamical characteristics of the secondary particles produced in $\pi^- C$ interactions at 40 GeV/c as a function of the cumulative number n_c

Ts. Baatar,* R. Togoo, B. Batgerel, G. Sharkhuu, B. Otgongerel, and T. Tulgaa
Department of Elementary Particles & Nuclear Physics,
Institute of Physics and Technology, Mongolian Academy of Sciences,
Peace Ave. 54b, Ulaanbaatar 13330, Mongolia

A.I.Malakhov
Veksler & Baldin Laboratory of High Energy Physics,
Joint Institute for Nuclear Research, 141980 Dubna, Russia

Multiparticle production process in $\pi^- C$ interactions at 40 GeV/c are studied by using a relativistic invariant parameter cumulative number n_c. Local values of temperature, pressure, volume and energy density in the interaction region are determined as a function of the cumulative number. This analysis gives us the possibility to study a space-time picture in the vicinity of the interaction point and the phase transition process at high energies.

I. INTRODUCTION

The investigation of the multiparticle production process in hadron-nucleus (hA) and nucleus-nucleus (AA) interactions at high energies and large momentum transfers plays very important role for understanding the strong interaction mechanism and inner quark gluon structure of nuclear matter.

According to the fundamental theory of the strong interaction, QCD [1], interactions between quarks and gluons become weaker as exchanged momentum increases. Consequently at large temperatures or densities, the interactions which confine quarks and gluons inside hadrons should become sufficiently weak to release them [2].

It is expected that QCD phase transition processes may be realized in (hA) and

*Electronic address: ts.baatar@ipt.ac.mn

(AA) interactions at high energies and large momentum transfers, in other words, these interactions give us possibility to study the nuclear matter under extreme conditions. During the last years the collective phenomena such as the cumulative particle production [3], the production of nuclear matter with high densities, the phase transition from the hadronic matter to the quark-gluon plasma state and color-superconductivity is widely discussed in the literatures [3-7].

In hA and AA interactions, in contrast to hN interactions, the secondary particles may be produced as a result of multi-nucleon interactions, in other words, the particles are produced in the region kinematically forbidden for hN interactions.

According to the different ideas and models, if these phenomena exist in the nature, then they will be observed in the above mentioned reactions and should influence the dynamics of interaction process, and would be reflected in the angular and momentum characteristics of the reaction products.

In this paper we are considered the next reactions:

$$\pi^- + C \to p + X \tag{1}$$

$$\pi^- + C \to \pi^- + X \tag{2}$$

at 40 GeV/c.

This paper is the continuation of our previous publications [4,8].

8791 $\pi^- C$ interactions are used in this analysis. 12441 protons and 30145 π^- -mesons are detected in these interactions.

II. EXPERIMENTAL METHOD

The experimental material was obtained with the help of Dubna 2-meter propane (C_3H_8) bubble chamber exposed to π^- -mesons with momentum 40 GeV/c from Serpukhov accelerator. All distributions in this paper are obtained in the condition of 4π geometry.

The average error of the momentum measurements is $\sim 12\%$, and the average error of the angular measurements is $\sim 0.6\%$.

All secondary negative particles are taken as π^- -mesons. The average boundary

momentum from which π^- -mesons were well identified in the propane bubble chamber is $\sim$ 70 MeV/c. In connection with the identification problem between energetic protons and π^+ -mesons, protons with momentum more than $\sim$ 1 GeV/c are included into π^+ -mesons. The average boundary momentum from which protons are detected in this experiment is 150 MeV/c. So, the secondary protons with momentum from $\sim$ 150 MeV/c to $\sim$ 1 GeV/c are used for proton distributions.

III. TEMPERATURE T AS A FUNCTION OF THE VARIABLE n_c

In our previous paper [4] we are studied the dependences of the temperature T on the variable n_c (or t) called the cumulative number. This variable n_c in the fixed target experiment is determined by the next formula:

$$n_c = \frac{(P_a \cdot P_i)}{(P_a \cdot P_b)} = \frac{E_i - \beta_a \cdot P_i^{||}}{m_p} \simeq \frac{E_i - P_i^{||}}{m_p} \tag{3}$$

Here P_a, P_b and P_i are the four-dimensional momenta of the incident particle, target and the considered secondary particles, correspondingly E_i is the energy and $P_i^{||}$ is the longitudinal momentum of the secondary particles, $\beta_a = \frac{P_a}{E_a}$ is the velocity of the incident particle, at high energy experiment $\beta_a \simeq 1$, so, may be omitted, m_p is proton mass. From formula (3) we see that this variable is relativistic invariant.

From the other hand side, the variable n_c at high energies is connected with the momentum transfer t by the next formula:

$$t = 2E_a \cdot m_p \left(\frac{E_c - \beta_a p_c^{||}}{m_p} \right) \simeq S_{hN} \cdot n_c \tag{4}$$

Where $S_{hN} = 2E_a m_p$ is the total energy square for hN interaction, which is constant in every experiment, so n_c may be used as the main variable.

For secondary particles produced in the region kinematically forbidden for hN interactions, this variable n_c takes the value more than 1, i.e.$n_c > 1$. This fact gives us the possibility to know which particles in the given event are produced in the region not allowed for hN interaction. This is another reason why we use this variable.

The transverse energy spectrum of the secondary particles produced in hA and AA interactions at high energies may reflect the dynamics of the interaction process more clearly. This is connected with the fact that the transverse effects are mainly

generated during the interaction process.

The effective temperature T of the secondary protons from reaction (1) as a function of the variable n_c is presented on FIG.1. This figure was taken from paper [4].

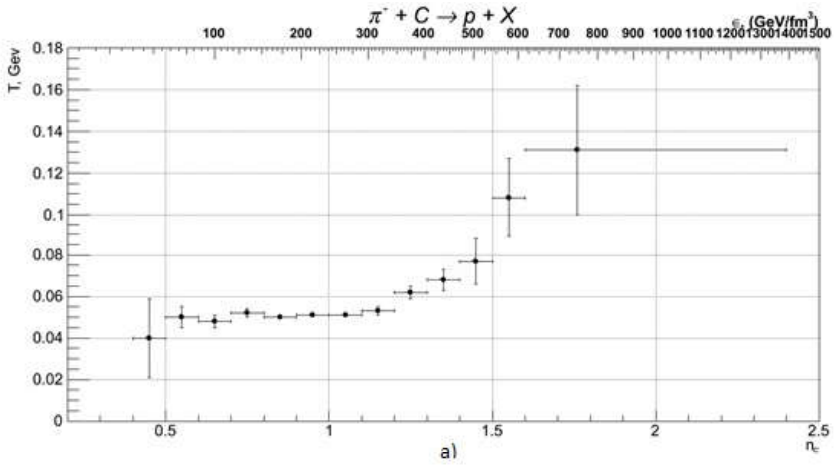

FIG. 1: Dependence of the effective temperature T on the variable n_c for the secondary protons.

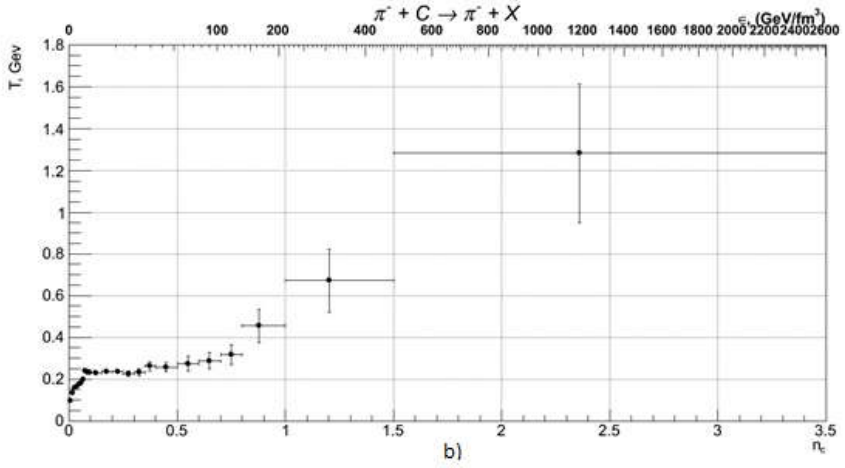

FIG. 2: Dependence of the effective temperature T on the variable n_c for the secondary π^- -mesons.

From FIG.1 we see that the effective temperature T remained practically constant on the level $T \simeq 50$MeV until $n_c \simeq 1.2$ and then increases. We note that we have no experimental points in $n_c < 0.4$ region. This connected with our difficulties of identification of protons with momentum $P_p > 1$GeV/c from energetic π^+ -mesons.

The similar dependence for π^- -mesons from reaction (2) is presented on FIG.2. From this figure we see that with increasing n_c the effective temperature T in the beginning is increasing until $n_c \simeq 0.07$, and then in the $(0.07 < n_c < 0.5)$ interval

the temperature T remains practically constant on the level $T \simeq 0.234$GeV and then essentially increases.

The strong changing of characters of the dependences of temperature T on the variable n_c may be an indication of the different mechanism of particle production in these regions. If so the first region with increasing T until T$\simeq$ 200MeV and $n_c < 0.07$ may correspond to the thermalization of the interacting objects (here the strongly interacting matter is in the thermally excited hadronic phase), the second region with approximately constant $T_c \simeq 234MeV$ in the $0.07 < n_c 0.5$ region for π^- -mesons and with constant $T_c \simeq 50MeV$ in the $0.5 < n_c < 1.2$ region for protons may be an indication of the equilibrium state formation (hadron + quarks, gluons) and the third region which shows the essential increasing of the temperature T in $n_c > 0.5$ for π^- -mesons and $n_c > 1.2$ for protons can be connected with the production of pure QGP state.

Our results show that the numerical characteristics for example, locations of the transition lines, temperatures in the QGP states of the phase transition processes for protons and pions are different.

IV. VOLUME AND ENERGY DENSITY ON THE VARIABLE n_c

The dependence of the energy density on the variable n_c may be determined by the next formula,

$$\epsilon(n_c) = \frac{\sqrt{S_{hN} \cdot n_c}}{V(n_c)} \tag{5}$$

Where $\sqrt{S_{hN} \cdot n_c}$ is the energy for producing of the secondary particles at given n_c and V(n_c) is the corresponding volume.

We would like to note that at summarizing the formula (3) by all secondary particles produced in the event, then we obtain the value of the total energy square determined on the basis of the energy-momentum conservation law, i. e.

$$Q^2 = S_{hN} \cdot M_t = S_{hN} \cdot \sum_{i=1}^{n} \frac{(E_i - \beta_a P_i^{||})}{m_p}; Q^2 \to S \tag{6}$$

We see that this formula is additive. If we detect all secondary particles produced in the event, then the total transferred momentum Q^2 determined by all secondary

particles tends to the total energy square S. This allows us to use the formula (4) to estimate the energy density.

Now we will consider the case of the dependence of the volume on n_c. To do this we are used our previous result on the particle emission region size, r [8]. This characteristic length r at high energies is determined by the formula,

$$r = \frac{1}{m_p\sqrt{n_c}} = \lambda_c^p = \frac{0.21[fm]}{\sqrt{n_c}} \tag{7}$$

We see that the parameter r is inverse proportional to the variable n_c. Here λ_c^p=0.21fm is the Compton wave length of proton. We also see that the secondary particles produced at n_C=1, the parameter r is equal to $\lambda_c^p(r = \lambda_c^p = 0.21fm)$, and if $n_c < 1$ then $r > \lambda_c^p$ and if $n_c > 1$ (for cumulative particles) then $r < \lambda_c^p$. In this case the time scale can be determined as $\Delta t = \frac{r(fm)}{c}$.

Now we have the possibility to determine the local V(n_c) from which the particle is emitted. In the first approximation V(n_c) is regarded as a spherical bubble with the parameter r calculated by the formula (7),

$$V(n_c) = \frac{4\pi}{3}r^3 = \frac{4\pi}{3} \cdot \frac{(0.21)^3}{n^{3/2}}[fm^3] \tag{8}$$

The dependence of the volume V on the variable n_c is shown on FIG.3. Experimental points for protons (black circles) and π^- -mesons (open triangles) from $\pi^- C$ interactions at 40 GeV/c calculated by formula (8) are also shown on this figure. We see that with increasing of the variable n_c the volume V is decreasing.

After the determination of the local volume V(n_c), we can calculate the local energy density $\epsilon(n_c)$ inserting formula (8) to formula (5) by the next formula,

$$\epsilon(n_c) = \frac{\sqrt{S_{hN}}n_c^2}{\frac{4\pi}{3}(0.21)^3}\frac{GeV}{fm^3} \tag{9}$$

This dependence was shown on FIG.4. Experimental values for protons (black circles) and π^- -mesons (open triangles) calculated by formula (9) are also shown on this figure. This dependence shows that with increasing n_c the energy density ϵ is essentially increased.

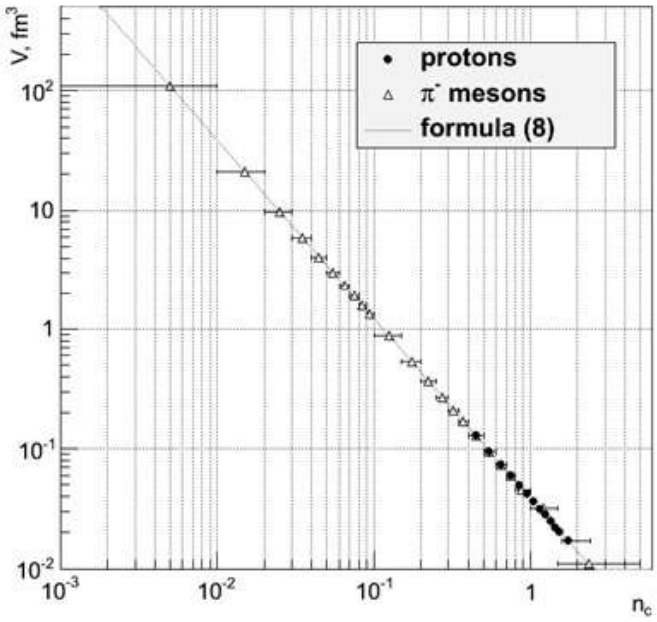

FIG. 3: Dependence of the volume V on the variable n_c.

From formula (9) we see that the local energy density $\epsilon(n_c)$ is determined by $\sqrt{S_{hn}}$ and n_c^2, in other words, by experimentally measurable quantities without model-depending assumptions. This is of course the main advantage of this formula.

So we have obtained the local energy density $\epsilon(n_c)$ and volume $\mathrm{V}(n_c)$.

Now we will consider the case of the pressure $\mathrm{P}(n_c)$. To do this we are used the Clapeyron equation for the ideal gas. This equation gives the connection between the pressure P, volume V and temperature T and can be written in the next form,

$$P(n_c) \cdot V(n_c) = k_B T(n_c) \tag{10}$$

Using the formula we can determine the pressure $\mathrm{P}(n_c)$.

$$P(n_c) = \frac{k_B T(n_c)}{V(n_c)} = \frac{k_B T(n_c) \cdot n_c^{3/2}}{\frac{4\pi}{3}(0.21)^3} \frac{GeV}{fm^3} \tag{11}$$

The pressure $\mathrm{P}(n_c)$ as a function of the variable n_c is shown on FIG.5. We see that with increasing n_c the pressure $\mathrm{P}(n_c)$ increases and at large values of the variable the pressure increases more rapidly.

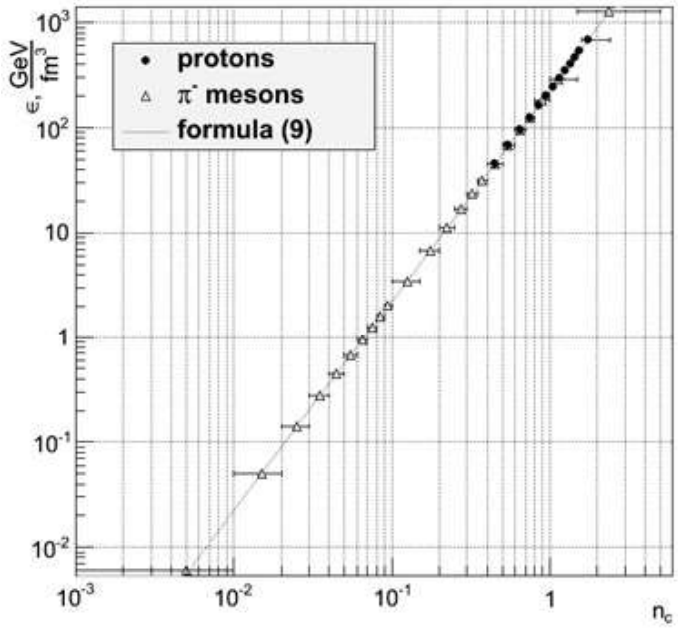

FIG. 4: The energy density ϵ as a function of the variable n_c.

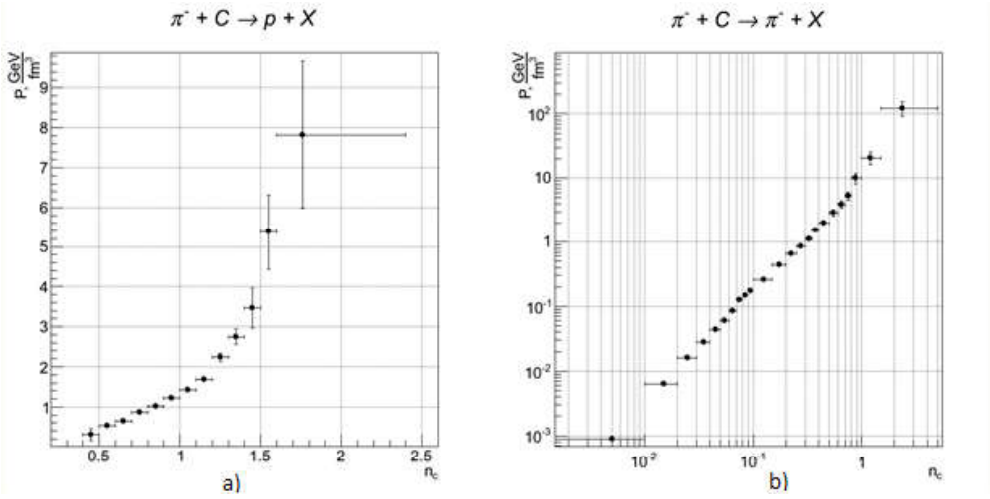

FIG. 5: (a, b) Dependences of the pressure P on the variable n_c for protons and π^- -mesons.

The dependence between the pressure P(n_c) and the temperature T(n_c) are presented on FIG.6(a,b). This dependence is called a curve of equilibrium of phases.

From FIG.6(b) we see that with increasing T(n_c) the pressure P(n_c) increases until $T = 0.200$GeV and then the temperature T is remained practically constant on the level $T = 0.234$GeV, while the pressure P(n_c) increases monotonously from $P_c^1(n_c) > 127.1 GeV/fm^3$ to $P_c^2(n_c) \simeq 1113.4 GeV/fm^3$ and then with the further

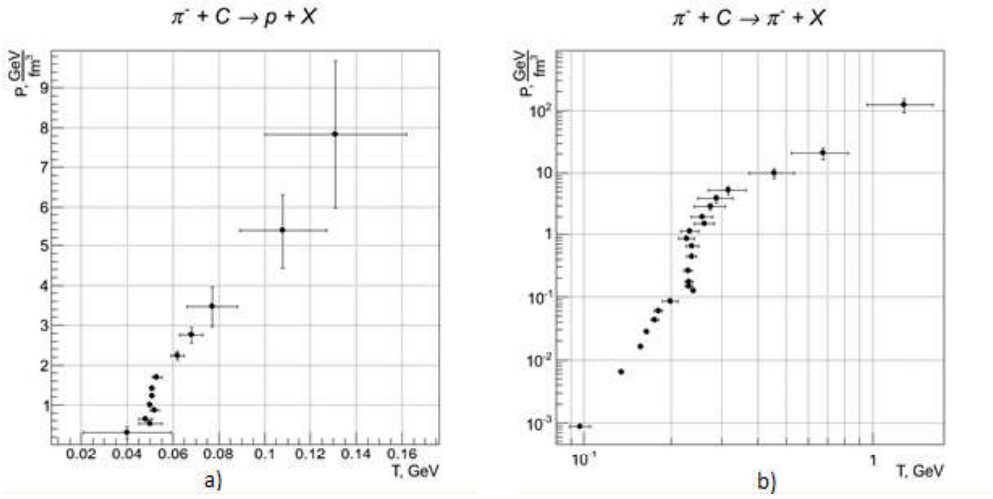

FIG. 6: (a, b) Dependences between the pressure P and the temperature T for protons and π^- -mesons.

increasing of T, the pressure rises again. So we can conclude that in the pressure interval $P_c^1(n_c) < P < P_c^2(n_c)$ with practically constant $T \simeq 0.234GeV$ is established the equilibrium state (or mixed phase).

The region with $T < T_c \simeq 0.234GeV$ and $p < P_c^1(n_c) = 127.1GeV/fm^3$ belongs to the thermally excited hadronic phase and the region with $T > T_c \simeq 0.234GeV$ and $P > P_c^2(n_c) = 1113.4GeV/fm^3$ belongs to QGP state.

In the case of the secondary protons the similar dependence between P and T is observed (FIG.6). The thermal equilibrium state is established at $T_c \simeq 50MeV$ in contrast to π^- -meson case. So the region with $T_c = 50$ and pressure interval $P_c^1(n_c) \simeq 526.0\frac{GeV}{fm^3} < p < P_c^2(n_c) \simeq 1685.7GeV/fm^3$ belongs to the thermal equilibrium state and the region with $T > T_c \simeq 50$MeV and $P > P_c^2 \simeq 1685GeV/fm^3$ corresponds to QGP state for protons.

We note that in connection with our identification problem of protons with momentum $P > 1$GeV/c we have no experimental points in the region with $T < T_c \simeq 50MeV$ and $P < P_c^1 = 526GeV/fm^3$.

We note also that with increasing of the temperature T the pressure P(n_c) increases and the volume V(n_c) decreases. So, at establishing of the equilibrium that two effects are mutually compensated each other for the both cases of protons and π^- -mesons from interactions at 40 GeV/c.

We would like to stress at last that the dependence of the pressure P on the temperature T is, of course, the consequence of the dependence of the temperature T on the variable n_c, but it gives us the additional information on the critical pressures P_c^1

and P_c^2.

V. CONCLUSION

In this paper we are determined the local energy density $\epsilon(n_c)$, temperature $T(n_c)$, pressure $P(T,n_c)$ and volume $V(n_c)$ of the interaction region. This gives us the possibility to study the space-time picture of the multiparticle production process at high energies including the phase transition from the hadronic state to the quark-gluon plasma.

Acknowledgments

We would like to express our thanks to the Ministry of Education, Culture and Science and and Foundation of Science and Technology for their financial support under the protocol 85A 018/14.

[1] D.J.Gross and F.Wilczek, Phys.Rev.Lett. 30(1973)1343, H.D.Politzer, Phys.Rev.Lett. 30(1973)1346

[2] J.C. Collins and M.J.Perry, Phys.Rev.Lett. 34(1975)1353

[3] A.M. Baldin, Particles and Nuclei, 1977, v.8.p.429

[4] Ts. Baataret al. JINR, E1-2012-13, Dubna, 2013, in Proceeding of XXI Int.Baldin.Seminar on High Energy Physics Problems, JINR, Dubna, Russia September 10-15, 2012

[5] K. Rajagopal, F.Wilczek, (2000) hep-ph/0011333

[6] Dirk H. Rischke, arxi:nucl-th/0305030 v2

[7] R. Hagedorn, Nouvo Cim.Suppl. 1965. v.3, p.147

[8] Ts. Baatar et al. Proceeding of XXII Inter. Baldin Seminar on High Energy Physics Problems, 064 15-20 September 2014, JINR, Dubna, Russia

Nonequilbrium Ising Bloch Transition in Forced Nonlocally Coupled Oscillators

Dorjsuren Battogtokh*

Department of Theoretical Physics, Institute of Physics and Technology, Mongolian Academy of Sciences, Peace Ave. 54b, Ulaanbaatar 13330, Mongolia and Department of Biological Sciences, Virginia Polytechnic and State University, Blacksburg, Virginia 24061, USA

We study phase and amplitude models for 2:1 resonant oscillators with nonlocal coupling and show that Ising Bloch transition - a bifurcation from standing to moving front - is dimmed by a regime with drifting frontal oscillators causing fluctuations of propagation direction. In the phase model, steady front propagation occurs only when the number of drifting oscillators is vanishing. In the amplitude model, front propagation failure occurs in an interval of a non-variational parameter, $\epsilon_1 < \epsilon < \epsilon_2$. At the lower limit of the parameter, ϵ_1, amplitude modulations are weak and Ising-Bloch bifurcation is similar to the front propagation in the phase model. At the upper limit of the parameter, ϵ_2, where amplitude modulations are significant, strong nonvariational effects leading to pattern formation impede the oscillators drifting and enforce Ising-Bloch transition.

I. INTRODUCTION

Insights into complexity can be acquired by monitoring its reactions to external perturbations. In this respect, oscillatory systems are particularly interesting because of resonance - nonlinear response at the forcing frequency rational multiple of the natural [1]. A very rich repertory of pattern formation, front turbulence, and nontrivial dynamics of spiral waves has been reported for distributed resonant oscillators [2–7]. A particularly well studied distributed system is the 2:1 resonant system with the forcing frequency twice of the natural [8–11].

Most of previously reported studies of 2:1 resonant systems were concentrated on locally coupled limit cycle oscillators. Direct local coupling, which is typical in chemical

*Electronic address: dbattogt@vt.edu

oscillations, implies diffusion of molecules displaying oscillatory kinetics. In biological systems, in addition to the direct local coupling, an effective coupling between molecular substances can be carried out by diffusive, coupling agents(ligands) - passive molecules not involved in the active kinetics, oscillatory or bistable dynamics [12]. If the time scale of coupling agents is much smaller than the oscillation period, the instant coupling range that the agents establish is greater than the range of local coupling that covers only the nearest neighbors. Hence, in the presence of fast, diffusive agents, active molecular substances located away from each other can instantly interact through the nonlocal field of the agents.

Recently, Kuramoto and colleagues, and other research groups studied nonlocally coupled oscillatory systems [13–19]. It was shown that nonlocally coupled systems display many interesting dynamics unknown in oscillatory systems with local coupling, such as coexistence of synchronization and desynchronization[16, 20], spiral waves without core [18], and power law scaling chemical turbulence [21, 22].

In externally forced systems with local coupling, the most fascinating phenomenon is the Ising-Bloch transition - a bifurcation from standing to moving front [8, 9]. When coupling is local, the frontal structures of both Bloch and Ising fronts are spatially continuous. In contrast, in nonlocally coupled systems, spatial coherence between the neighboring oscillators can be lost [12]; therefore, front profiles can be spatially discontinous. Thus, an interesting problem is propagation of a front subject to spatial discontinuity.

The subject of this work is front bifurcation in the 2:1 resonance system with nonlocal coupling. In the next section we will introduce the forced nonlocally coupled Ginzburg-Landau equation (CGLE). We will analyze nonlocally coupled phase model, which can be obtained from the forced CGLE in the weak coupling limit, in section III. In section IV we show Ising-Bloch transition in the forced CGLE in dimensions one and two. Discussion is in the last section.

II. THE MODEL

The Stuart-Landau equation is the normal form of a limit cycle oscillator near a Hopf bifurcation [24]. When the oscillator is externally forced, a new term is included in the Stuart-Landau equation. If the forcing frequency is twice of the original, the

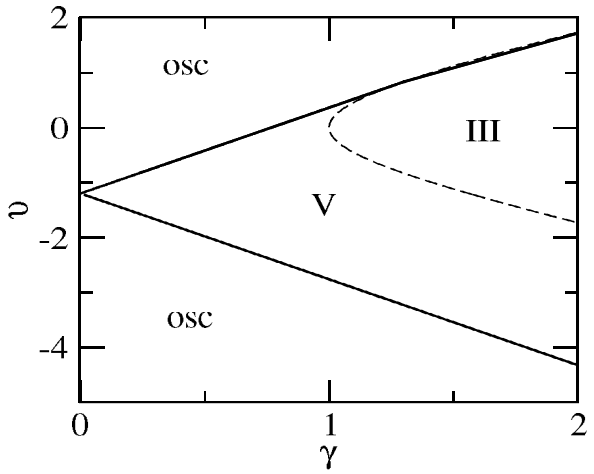

FIG. 1: A bifurcation diagram of Eq. (1) on the (γ, ν) plan for $\beta = -1.2$. Inside the solid lines there is a region of bistability, which is divided by the dashed lines into the subregions with three (III) and five (V) steady states. Outside the solid lines, Eq. (1) displays oscillatory dynamics.

modified model has the following form in the reference frame of the forcing frequency,

$$\dot{A} = (1 + i\nu)A - (1 + i\beta)|A|^2 A + \gamma A^*, \tag{1}$$

where, A is a complex function; ν, β, and γ are real parameters; and A^* is the complex conjugate of A. The last term represents the external forcing. Solutions of Eq. (1), oscillating at the frequency rational multiple of the forcing frequency are called the mode-locked solutions. There are two stable mode-locked solutions in Eq. (1), which differ from each other by the phase difference π. The mode-locked solutions, $A = \pm R\exp(i\psi)$, are given by the stationary solutions of Eq. (1),

$$\begin{aligned} \cos(2\psi) &= (R^2 - 1)/\gamma, \\ \sin(2\psi) &= (\omega - \beta R^2)/\gamma, \\ R^2 &= \frac{1 + \beta\omega + [\gamma^2(1 + \beta^2) - (\omega - \beta)^2]^{1/2}}{1 + \beta^2}. \end{aligned} \tag{2}$$

In addition to the stable solutions, depending on parameters ν, β, and γ, Eq. (1) displays also unstable steady states. On the parameter plane (γ, ν), the steady solutions are found inside the solid line which marks transitions from mode-locked solutions to quasiperiodic and complex oscillations, Fig. 1.

Let consider distributed in space forced oscillators. An interesting solution is when

oscillators split into two mode locked states with the phase difference π. If the oscillators are coupled locally, there is a front connecting the phase locked states, which depending on parameters displays very rich dynamics, including transition from standing to moving front, regular or chaotic front motions, and pattern formation instability [9].

In biological systems, coupling between the oscillatory elements is often carried out by diffusion of inactive molecules which are not involved directly in the active kinetics. Proteins regulating cell's life interact with each other through reaction networks which can display various complex dynamics, including oscillations. Cell membranes do not allow these macro-molecules freely diffuse between different cellular compartments and cells. For example, cyclin-dependent protein kinases interact with other proteins and genes through the reaction network called the cell cycle engine to regulate the cell cycle rhythm. The engine operates in the cell's nuclei and its substances cannot diffuse freely outside of the cell. However, cells can coordinate their cell cycle progression pace by exchanging information through diffusive molecules with short time scales; for instance, through growth factors that control indirectly the dynamics of the protein-kinases by activating or deactivating key enzymes that subsequently phosphorylate/dephosphorylate the cyclin dependent protein kinases. Mathematically, coupling by an inactive diffusive molecule with a short time scale leads to nonlocal coupling [13]. In the presence of nonlocal coupling, the canonical form, Eq. (1), includes a coupling term, Z,

$$\dot{A} = (1 + i\nu)A - (1 + i\beta)|A|^2 A + \mu(1 + i\epsilon)Z + \gamma A^*. \tag{3}$$

The complex nonlocal field Z is given by [23],

$$Z = \int \exp(-\kappa|\mathbf{r} - \mathbf{r}'|)(A(\mathbf{r}') - A(\mathbf{r}))d\mathbf{r}'. \tag{4}$$

When oscillators are coupled, the phase locked states should be connected by an interface. Indeed, in locally coupled systems, diffusive coupling leads to a spatially continuous front. Therefore, one expects that the coupling by Z leads to a front connecting the phase locked states given by Eq. (2). However, previous studies of a population of oscillators coupled by nonlocal coupling show that spatial discontinuity is characteristic for nonlocal coupling. Hence, a front solution in Eqs. (3)-(4) can

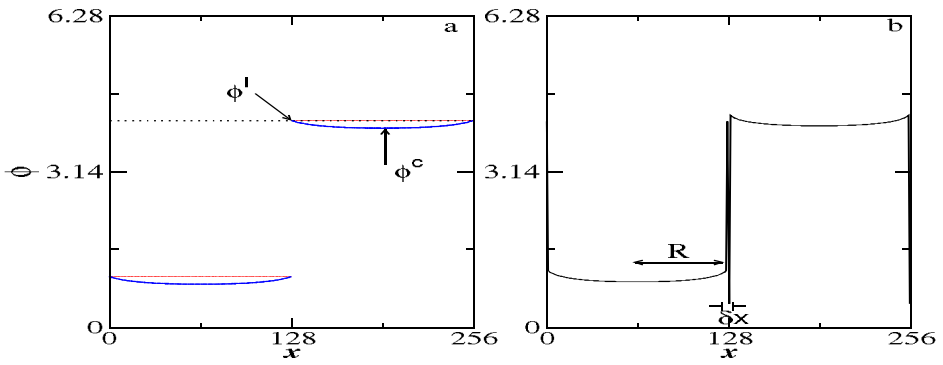

FIG. 2: Solutions of the phase model, Eqs. (5)-(6), in a system with periodic boundary conditions. a) Uniform solution is shown by dotted lines. Red lines show two phase locked states. Blue lines show distorted phase locked states for $\mu = 0.5$. Parameters are $\Omega = 0.835$ and $\gamma = 0.875$. b) Phase domains stabilized by nonlocal coupling. The size of a domain is given by its radius R. δx is the interface width. Parameters are $\Omega = 0.875$, $\gamma = 0.835$, and $\mu = 0.5$. Other parameters are $\delta = 0.394$, $\kappa = \frac{1}{16}$, and $\alpha = 1.6$.

be spatially discontinuous. A question arises as to whether Ising-Bloch bifurcation is possible in forced oscillators with nonlocal coupling?

III. ANALYSIS OF THE PHASE MODEL

In the weak coupling limit, when the perturbations modulating the oscillation amplitude is small, Eqs.(3)-(4) can be reduced to a phase model [24], which can be very helpful for theoretical analysis. The phase equation reads,

$$\frac{d\phi}{dt} = \Omega - \gamma' \sin[2(\phi - \delta)] + Z_\phi, \tag{5}$$

$$Z_\phi = \mu \int \exp(-\kappa|\mathbf{r} - \mathbf{r}|) \sin(\phi(\mathbf{r}) - \phi(\mathbf{r}') + \alpha) d\mathbf{r}'. \tag{6}$$

In Eqs.(5)-(6) $\Omega = \beta(\mu - 1) + \nu - \epsilon\mu$; $\gamma' = \gamma\sqrt{1+\beta^2}$; $\sin(2\delta) = -\frac{\beta}{\sqrt{1+\beta^2}}$; and, $\tan(\alpha) = \frac{\beta - \epsilon}{1+\epsilon\beta}$.

Let find simple solutions of Eqs. (5)-(6) and investigate their stability. If $\mu = 0$ and $\gamma' \geq \Omega$, there are two phase locked states, ϕ^L and $\phi^L + \pi$, which are solutions to

$$\Omega - \gamma' \sin(2(\phi - \delta) = 0. \tag{7}$$

Another simple solution for $\mu \neq 0$ is the uniform solution, $\phi^U = 0.5 \arcsin[\frac{\Omega - \mu\sin(\alpha))}{\gamma'}] + \delta$.

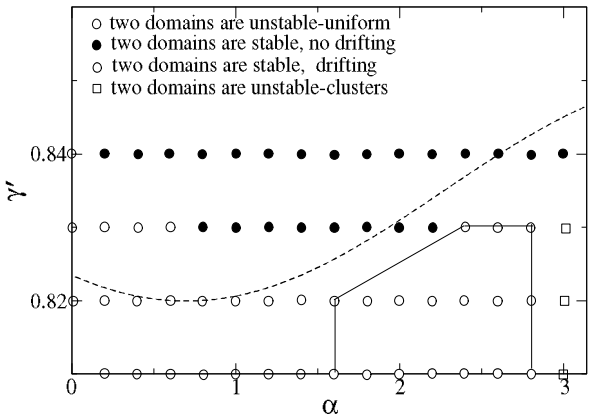

FIG. 3: Bifurcation to drifting oscillators in Eqs. (5)-(6). Dashed line is analytically found curve below which an interface oscillator losses stability. Open circles mark areas where the two domain solution(TDS) is unstable and uniform solution emerges. Open boxes mark areas where TDS is unstable and clusters emerge. Connected by lines partially filled circles mark areas where TDS is stable but drifting oscillators emerge. Filled circles show areas with stable TDS and no oscillator drifting. Parameters are $\Omega = 0.875$, $\gamma' = 0.835$, $\delta = 0.394$, $\mu = 2.32$, $\kappa = \frac{1}{32}$. $N = 256$ and periodic boundary condition.

Based on the analysis of the amplitude model(Fig. 1), at small μ, the phase locked solutions are expected to be stable. An emergent, nonuniform solution is coexistence of two domains with local phases close to $\phi^L = \frac{1}{2}\arcsin[\frac{\Omega}{\gamma'}] + \delta$ and $\phi^L + \pi$, Fig. 2a. Note that if $\mu = 0$ and $\gamma' \leq \Omega$, there are no stable uniform solutions to Eq. (7), because oscillators are drifting. However, for these parameters values, solutions forming stable domain structures similar to in Fig. 2a are possible in Eqs.(5-6) if $\gamma' \approx \Omega$. Though, it is difficult to obtain analytic expressions for such solutions, these solutions forming a stable domain structure can be found numerically, Fig. 2b. For the domains stabilized by nonlocal coupling, oscillator drifting at the interface region is typical, because coupling field can vanish there due to the symmetry of the domains.

Consider small μ and mark the phases at an interface and a center of a domain by ϕ^I and ϕ^C, respectively. Assuming a linear phase distribution from the center of the domain to the interface, $\phi^I = \phi^C + qx$, we evaluate the coupling integrals at these locations,

$$Z^I_\phi = -\frac{\mu'\kappa}{q^2+\kappa^2}[q\cos(\alpha) + \kappa\sin(\alpha) - \exp(-\kappa\delta x)(q\cos(\alpha_1) + \kappa\sin(\alpha_1))], \tag{8}$$

$$Z^C_\phi = -\frac{\mu'\kappa}{q^2+\kappa^2}[\exp(-\kappa R)(2q\cos(\alpha_2) + 2\kappa\sin(\alpha_2)) + -q\cos(\alpha) + \kappa\sin(\alpha)]. \tag{9}$$

In Eqs.(6)-(7) δx is the interface width, and R is the distance from the center of the domain to the interface, and $\alpha_1 = \alpha + q\delta x$ and $\alpha_2 = qR - \alpha$. For $\delta x << 1$ and $q \to 0$ we find that $Z_\phi^I \approx -\mu\kappa \sin(\alpha)\delta x$ and $Z_\phi^C \approx -\mu[1 - 2\exp(-\kappa R)]\sin(\alpha)$. If coupling range is large, κ is small, therefore, for sufficiently long-range coupling, Z_ϕ^I is negligible and ϕ^I is close to ϕ^L. Contrary, the phase at the center, $\phi^C \approx \frac{1}{2}\arcsin[\frac{\Omega - \mu\sin(\alpha)}{\gamma'}] + \delta$ can be larger or smaller ϕ^L, depending on α and κR. In other words, the center of the domain is concave or convex depending on the value of α.

At small μ, we can treat nonlocally coupled oscillators as uncoupled rotors subject to a time dependent forcing field with spatial distribution. In this way, the stability of a domain can be studied by considering only two oscillators, the ones at the center of the domain and at the interface. By perturbing the solutions ϕ^I and ϕ^C with small perturbations $\delta\phi\exp(\lambda t + qx)$, λ can be calculated. For $\delta x << 1$ and $q \to 0$, we find $\lambda_I = -2\gamma'\cos[2(\phi^I - \delta)]$ and $\lambda_C = -2\gamma'\cos[2(\phi^C - \delta)]$, respectively. Hence, the instability conditions reads as, $\kappa\mu\sin(\alpha)\delta x \leq \Omega - \gamma'$ and $\mu\sin(\alpha) \leq \Omega - \gamma'$. Thus, for parameters in Fig. 2a and for $\alpha \in [0, \pi/2]$, both ϕ^I and ϕ^C are stable to small perturbations. Interestingly, for $\alpha \in (\pi, 2\pi]$ and for some ranges of the parameters μ and κR, the solution ϕ^I can be linearly stable when ϕ^C is linearly unstable. Note that such an instability may lead to a cluster formation.

If γ' is sufficiently large and $\gamma' \geq \Omega$, a front connecting mode-locked states are motionless. Such a front is called an Ising front. In locally coupled systems, with the decrease of γ', there is a transition to a moving front called a Bloch front. Our simulations indicate that in nonlocally coupled systems, the decrease of γ' does not always lead to a moving front because drifting oscillators emerge at the interface, enforcing fluctuations of propagation direction. Here we consider the dependence of oscillator's drifting on two parameters, α and γ'. To locate transitions from a phase-locked state to a drifting state on the parameter plane (α,γ'), we numerically compute the phase distribution and the nonlocal field, $Z_\phi(x)$, for oscillators forming phase-locked domains as shown in Fig. 2a. Then, we consider an interface oscillator at the Ising front as an uncoupled oscillator subject to the nonlocal field $Z_\phi^I(x)$. Next, we assume that the phase distribution of other oscillators are stationary and use the parameters α and γ' as bifurcation parameters. Then we numerically locate saddle-node bifurcations which we regard as approximate transition points from phase-locked states to drifting states, dashed-line Fig. 3. We also mark in Fig. 3 results of direct numerical simulation of Eqs. (5)-(6), from an initial condition with two unform phase

locked states with the phase difference π. Filled circles in Fig. 3 show cases when an interface has no drifting oscillators(similar to the phase distribution shown in Fig. 2a), whereas partially filled circles show the case when there are drifting oscillators as shown in Fig. 2b. Thus, according to Fig. 3, when parameter γ' is fixed, the system can display different front profiles depending on parameter α.

Simulations show that when there are no drifting oscillators, front propagation in Eq. (5) resembles front dynamics in locally coupled systems, with distinct Ising-Bloch transitions. However, when drifting oscillators emerge with the change of parameter α, failure of front propagation occurs. In the parameter region depicted by the solid line in Fig. 3 front direction fluctuates; as a result, no steady propagation of a front has been observed in simulations. Note that Eq. (5) is valid when coupling is weak and the nonvariational coefficients, ϵ, ν, and β, are small in the amplitude model. In the next section we examine the amplitude model when the nonvariational coefficents are not small.

IV. DOMAIN PROPAGATION IN THE AMPLITUDE MODEL

Parameter α in Eq. (6) depends on ϵ, therefore, we can use analysis of Eqs. (3)-(4) by controlling ϵ in the amplitude model while fixing other parameters. As an initial condition, we again consider two equal-sized domains with the phase difference π. When $\epsilon < -2$, the front propagation resembles dynamics in the phase model, which do not involve notable amplitude modulations. If $-2 < \epsilon < 3$ a front is immobile or cannot propagate steadily because of drifting oscillators at the interface, which change the propagation direction randomly. A front region displays time by time from two to eight large phase jumps ($|\frac{\partial \phi}{\partial x}| > 2.5$), for which the drifting oscillators are responsible. As we increase ϵ above the value 3, fluctuation of front propagation direction decreases, and the number of large phase jumps in the frontal region is reduced. The frontal pattern of a Bloch front shows some spatial regularity resembling a periodic pattern, Fig. 4. By computing spatial correlation functions, we confirmed that periodic structures in the frontal region are robust.

Note that the unstable, uniform solution of Eqs. (3-4), $A = 0$, has linear spectra $\lambda = 1 - \sigma \pm \sqrt{\gamma^2 - (\nu - \epsilon\sigma)}^2$, where q is the wavenumber and $\sigma = \frac{\mu q^2}{\gamma^2 + q^2}$. The spectra are positive everywhere, with $\lambda = 1$ at $q = 0$ and $\lambda \approx const$ at large q. Therefore, if we assume that the frontal region is given by $A = 0$ solution, it can be subject to

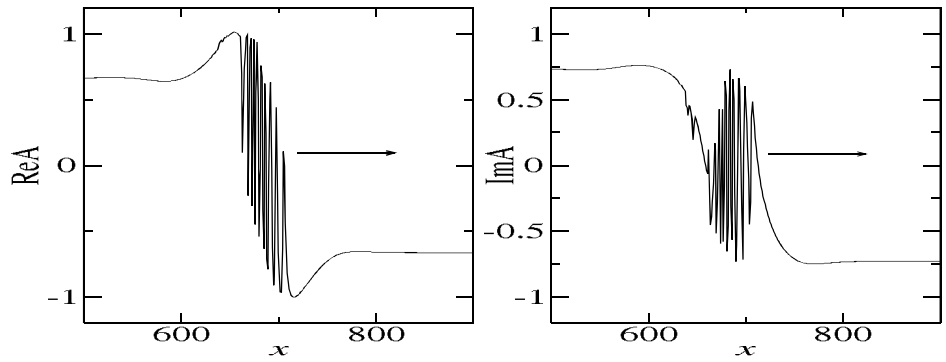

FIG. 4: Frontal pattern of a Bloch front in a one dimensional(1d) system with noflux boundary condition. Arrows mark propagation direction. Parameters are: $\epsilon = 3.5$, $\beta = -1.2$, $\nu = -0.825$, $\mu = 0.4$, $\kappa = \frac{1}{16}$, $N = 1024$, and $\gamma = 0.4$.

wavenumber instability. Previous studies of the 2:1 resonance system with diffusive coupling show that wavenumber selection is particularly clear when the parameter ϵ is large [10, 11]. Also, it is known that the velocity of a front increases with the increase of nonvariational parameters, including ϵ. Therefore, our explanation for Ising-Bloch bifurcation in the amplitude model is that for an appropriate choice of the parameters ϵ and γ, wavenumber selection and front propagation processes mutually stabilize each other: front propagation selects a particular wavenumber, whereas pattern formation prevents oscillator drifting.

The fact that oscillators drifting at the frontal region causes front propagation failure can be confirmed by enforcing Ising-Bloch transition by synchronizing oscillators drifting at frontal regions. Let us assume that Z field couples the forced oscillators with a time delay τ, and it appears in Eq. (3) as $Z(t-\tau)$. Simulations show that when $\epsilon = 2.5$, $\gamma = 0.35$ and other parameters are the same as in Fig. 4, there is no steady front propagation if $\tau = 0$. However, if $\tau \approx 2.75$, oscillators drifting ceases, and a front propagation similar to the case with small amplitude modulations occurs.

We confirmed that in dimension two, when transition to a Bloch front occurs from a regime with drifting oscillators, the system displays periodic frontal structures. As for the Ising-Bloch transition with weak amplitude effects, interesting pattern is a rotating wave with a complex core, Fig. 5. Despite the presence of a few drifting oscillators at the core region, rotation is steady. Similar to the theory presented in Ref. [18, 20], the complexity of the core is due to the vanishing of the coupling field, Z, near the core.

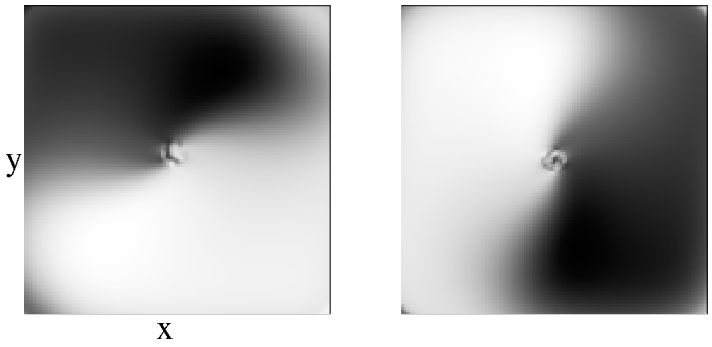

FIG. 5: Rotating waves with complex core in a system(128,128) with no flux boundary. Parameters are the same as in Fig. 4. Two different time moments are shown as gray scale plots of $Im(A)$.

V. DISCUSSION

Recent studies show that external periodic forcing can enforce mode locking of the eukaryotic cell cycle [25, 26]. In a population of yeast cells, growth factors(e.g. TGF-α) with time scales much shorter than the cell cycle period mediate between the cells. Such a system can be studied by the mathematical formalism presented in this paper. Our results suggest that if as a result of forcing, cell population is in the mode locked domains with different phases(corresponding to different physiological states), nonlocal coupling by the growth factors may obscure or induce a wave propagation depending on the value of a control parameter. Front propagation failure is known in a model of a tissue where cell's are under long range coupling [27]. According to our model, front propagation failure can be prevented by nonequilbrium effects and time delayed feedbacks.

Our result that the nonlocal field can lead to emergent stable domains when the uncoupled system has no stable steady states seems very interesting. One may speculate that pathological cells may use such a mechanism to emerge in the tissue. We will study this subject in detail in a separate work [28].

It is also known that front propagation in the 2:1 resonant system is similar to the front dynamics in models of bistable systems. Therefore, our results presented in this paper can be relevant to bistable systems with long range coupling. We hope that periodic frontal structures and spiral waves with complex cores can be observed in

experimental systems.

Acknowledgments

This work has been supported by a grant of the Mongolian Foundation for Science and Technology under the contract SSA-009/14. The author is thankful to Prof. Kh. Namsrai and Prof. B. Chadraa for fruitful discussions.

[1] L. Glass, Nature **410**, 277(2000).

[2] Hemming and R. Kapral, Faraday Discuss. **120**, 371 (2001).

[3] C. J. Hemming and R. Kapral Phys. Rev. E **68**, 026203 (2003).

[4] J. Davidsen, A. S. Mikhailov, and R. Kapral Phys. Rev. E **72**, 046214 (2005).

[5] A. Yochelis, C. Elphick, A. Hagberg, and E. Meron, Europhys. Lett. **69**, 170 (2005).

[6] A. Yochelis, C. Elphick, A. Hagberg, and E. Meron, Physica **199** D, 201 (2004).

[7] A. L. Lin, A. Hagberg, E. Meron, and H. L. Swinney Phys. Rev. E **69**, 066217 (2004).

[8] P. Coullet, J. Lega, B. Houchmanzadeh and J. Lajzerowicz, Phys. Rev. Lett. **65**, 1352 (1990).

[9] P. Coullet and K. Emilsson, Physica D **61**, 119(1992).

[10] D. Battogtokh and D. Browne, Phys. Lett. A **266**, 359 (2000).

[11] D. Battogtokh, Phys. Rev. E **66**, 066202 (2002).

[12] Y. Kuramoto, H. Nakao, and D. Battogtokh, Physica A, **288** ,244(2000).

[13] Y. Kuramoto, *Nonlinear Dynamics and Chaos; Where do we go from here.* (IOP. 2003) Ch. 9.

[14] V. Casagrande and A. S. Mikhailov, Physica **205** D, 154(2005).

[15] D. Battogtokh, Prog. Theor. Phys. **102**, 947(1999); Phys. Lett. A **299**, 558(2002).

[16] D. M. Abrams and S. H. Strogatz, Phys. Rev. Lett. **93**, 174102(2004).

[17] Y. Shiogai and Y. Kuramoto, Prog. Theor. Phys. Suppl. **150**, 435(2003).

[18] S. Shima and Y. Kuramoto, Phys. Rev. E **69**, 036213 (2004).

[19] F. Plenge, H. Varela, and K. Krischer, Phys. Rev. Lett. **94**, 198301 (2005).

[20] Y. Kuramoto and D. Battogtokh, Nonlin. Phenom. Complex Syst. **5**, 380 (2002).

[21] D. Battogtokh, Y. Kuramoto, Phys. Rev. E **61**, 3227(2000).

[22] Y. Kuramoto, D. Battogtokh, H. Nakao, Phys. Rev. Lett. **81**, 3543(1998).

[23] D. Tanaka and Y. Kuramoto, Phys. Rev. E **70**, (2004).

[24] Y. Kuramoto, *Chemical Oscillations, Waves and Turbulence*, Springer-Verlag, Berlin, 1984.

[25] F. R. Cross and E. D. Siggia, Phys. Rev. E **72**, 021910(2005).

[26] D. Battogtokh and J. J. Tyson, Phys. Rev. E **73**, 011910(2006).

[27] C. B. Muratov and S. Y. Shvartsman, Phys. Rev. Lett., **93**, 118101(2004).

[28] D. Battogtokh, unpublished.

STUDYING TOPOLOGY FOR NANO ANTENNA

T. Begzsuren, G. Munkhbayar, M. Otgonbaatar
Department of Physics, School of Arts & Sciences, National University of Mongolia, University Street-1, 210646 Ulaanbaatar, Mongolia

Guy A. E. Vandenbosch
ESAT- TELEMIC, University of Leuven, Kasteelpark Arenberg 10 - box 2444, Leuven, Belgium

The efficiency of a nano-rectenna strongly depends on the interaction between shape and materials of the antenna element. In this paper, upper bounds for this rectenna efficiency are determined for bowtie shaped dipoles fabricated of Au, Ag, and Al. The result is that an optimal total harvesting efficiency of about 57% is obtained, which is 11% higher compared to traditional nano dipole topology.

I. INTRODUCTION

The fundamental question whether optical waves can be efficiently converted into electricity using nanometer scale antennas and rectifiers is a highly important research field. The idea was originally proposed by Robert L. Bailey in 1972 [1]. However, it was not until 2005 that real research had started due to the lack of technical ability to manufacture structures at the nanometer scale [2]. Nowadays, by some researchers it is claimed that so-called nano-rectennas could harvest more energy from a wider spectrum of sunlight, in this way offering the possibility to replace traditional silicon solar cells[3, 4]. Once realized, this concept would revolutionize the energy market. It would partially solve the energy problem of human kind, and this would be done in a completely clean and renewable way.

In recent years, the concept of using nano-rectennas in solar energy harvesting has been intensively investigated. A thorough numerical investigation was published in [5, 6]. It was shown there that at a single frequency in the solar spectrum, up to 90% of the energy can be made available at the output of a silver nano dipole. However, the radiation from the sun is spread out over a wide frequency range, mainly in the visible and near-infrared bands. Therefore, the concept of total harvesting efficiency was defined in[5], taking this issue into account, yielding levels of about 60 70 %. In

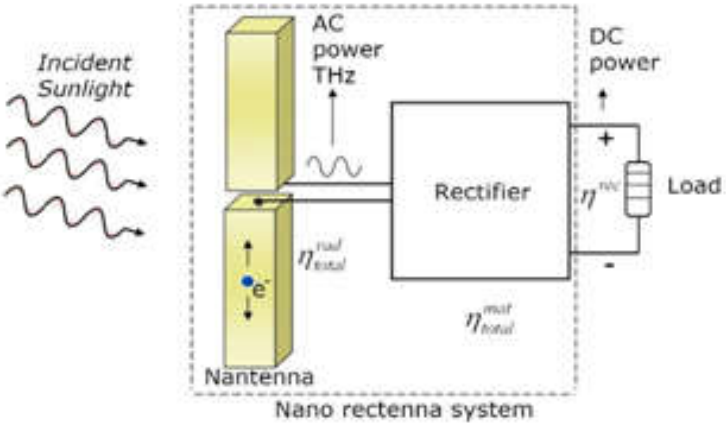

FIG. 1: Schematic representation of a nano rectenna system for solar harvesting. The light is absorbed via a suitable antenna and the generated AC power is fed through a rectifier to produce a DC power. The symbols η_{total}^{rad}, η_{total}^{mat}, η^{rec} represent the total radiation efficiency, the total matching efficiency, and the rectenna efficiency, respectively.

[6], results were presented of upper bounds for the receiving efficiency for 5 different metals in terms of the dimensions of a simple nano dipole antenna. The receiving efficiency also takes into account the matching with the rectifier circuits. For silver dipoles, a maximum receiving efficiency of about 54% was found and for Al dipoles, this value was about 46%.

In this paper, the goal is to increase the maximum receiving efficiency by using the shape of the nano dipole. The main idea is to use the bowtie topology, which is a well-known topology to obtain a broad band in classical antenna design at microwave frequencies.

II. THE RECTENNA TOPOLOGY

A nano-rectenna system consists of two parts, see Fig.1. The first part is the nano antenna or nantenna that converts the incident light into electric current at Terahertz frequencies flowing in the body of the antenna and available at the port. In this conversion, the total radiation efficiency is a key parameter and the first factor in the total efficiency product.

The second part is a rectifier that converts the THz current at the nano antenna output port to DC electrical current, generating a DC power in the load.

At present, there are still two main challenges in the design of nano-rectenna systems. The first one is the realization of rectifiers at optical frequencies. In a

conventional rectification, i.e. at RF and microwave frequencies, a diode is used. Such rectennas have been proven to successfully convert microwave radiation into DC power, achieving conversion efficiencies as high as 91% [7]. MIM (metal-insulator-metal) point contact diodes based on Nb_2O_5 and $Nb-TiO_2$ have been fabricated and successfully tested at somewhat lower frequencies [8]. However, present-day diodes are still unable to efficiently rectify at visible and near-infrared frequencies. Since thermodynamic calculations suggest that rectennas can convert any electromagnetic radiation to DC power with a conversion efficiency of at least 85% [9], the search for the proper diode technology is currently fully in progress.

The aim of this work is to deal with the second great challenge: the optimization of the shape of the nantenna topology in order to maximize the rectenna efficiency for the visible and near-infrared bands. In this work, the bowtie topology is considered, since it is a well-known topology to generate broadband behavior at microwave frequencies. Three materials are considered: Gold, Silver, and Aluminum. Al has the great advantage that its oxide is transparent at the frequencies targeted, indicating much lower losses than for the oxide of Silver [10, 11]. The values of the permittivities are taken from [12]. The efficiency calculation is performed in the wavelength (of frequency) range between $300nm$ and $1300nm$, where about 80 percent of the energy of the sun is present. The optimization procedure follows the same lines as in [13]. It takes into account the nantenna input impedance and rectifier impedance since they determine the matching between these two components.

III. TOPOLOGY AND ANALYSIS TOOLS

The nantenna topology studied in this paper is depicted in Fig.2. The dipole consists of two trapezoidal arms on top of a glass (SiO_2) substrate, which is transparent. The gap between the two dipole arms is $G = 10nm$, which is conform to the resolution obtainable with current fabrication technology. The height H and the short base length W are both $40nm$. These values are suited for the frequency range targeted and can easily be fabricated with existing fabrication technology. G, H, and W are kept constant. The dipole length L is varied between $100nm$ and $400nm$, with a step of $20nm$. The base angle in the bowtie topology is Φ. The base angle is varied between 0^o and 50^o with a step of 5^o. The power captured by the bowtie is fed to the rectifier circuit which is assumed to be present near the middle of the gap. The

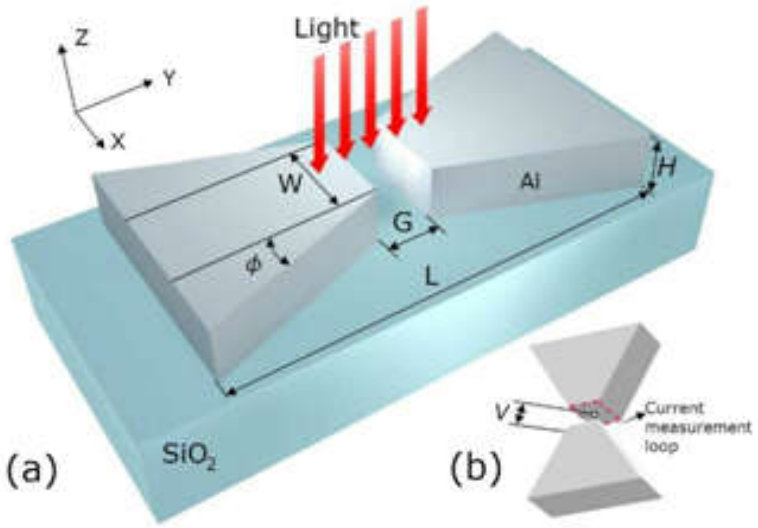

FIG. 2: The trapezoidal dipole or bowtie studied: (a) dimensional parameters, (b) the port with voltage and current at the output where the rectifier circuit is assumed.

incident electric field is polarized along Y-axis.

For mutual validation purposes, numerical calculations were performed using two totally different solvers. The first one is Lumerical, using the FDTD technique [14]. The second one is MAGMAS, an in-house developed solver using integral equations solved with the method of moments(MoM) [15–17].

The voltage and current at the output port of the nantenna are determined as indicated in Fig.2(b). The voltage is the integrated electric field between the two arms. In Lumerical, the current is obtained through Ampres law from the loop integral of the magnetic field around the gap. The 3D setup, PML boundary conditions are selectedand mesh sizes are chosen $\Delta x = 2nm$, $\Delta y = 1nm$, and $\Delta z = 2nm$. In MAGMAS, the delta gap current source concept is used, see [15]. The input impedance of the nantenna is

$$Z_{ant} = \frac{\int_{-G/2}^{G/2} E_y \mathrm{d}y}{\oint_{loop} H \mathrm{d}S} \tag{1}$$

IV. CALCULATION OF EFFICIENCIES

A nano-rectenna systems efficiency is the product of the nantennas total harvesting efficiency η_{total}^{rad} and the matching efficiency η_{total}^{mat} between nantenna and rectifier

$$\eta^{rec} = \eta_{total}^{rad} \cdot \eta_{total}^{mat} \tag{2}$$

The total radiation efficiency is defined by how much energy can be harvested by the nantenna over the complete band targeted. It can be derived from the conventional radiation efficiency as [13]

$$\eta_{total}^{rad} = \frac{\int_{\lambda_{start}}^{\lambda_{stop}} P_{inc}(\lambda)\eta^{rad}(\lambda)\mathrm{d}\lambda}{\int_{\lambda_{start}}^{\lambda_{stop}} P_{inc}(\lambda)\mathrm{d}\lambda} \tag{3}$$

where λ is the wavelength of the incident light, $\eta^{rad}(\lambda)$ is the classical radiation efficiency of the nantenna as a function of the wavelength, and P_{inc} is Plancks law for black body radiation

$$P_{inc} = \frac{2\pi hc^2}{\lambda^5} \times \frac{1}{e^{hc/\lambda kT} - 1} \tag{4}$$

where T is the absolute temperature of the surface of the sun (in K), h is Plancks constant ($6.626 \cdot 10^{-34} J \cdot s$), c is the speed of light in vacuum ($3 \cdot 10^8 m/s$), and k is the Boltzmann constant ($1.38 \cdot 10^{-23} J/K$). The radiation efficiency of an antenna is defined as

$$\eta^{rad} = \frac{P^{rad}}{P^{inject}} = \frac{P^{rad}}{P^{rad} + P^{loss}} \tag{5}$$

where P^{rad} is the radiated power in transmit mode, P^{inject} is the power injected at the terminal, and P^{loss} is the power dissipated in the material of the antenna.

The equivalent circuit of the total rectenna system is depicted in Fig.3. Based on the circuit, the total matching efficiency is derived as [13]

$$\eta_{total}^{mat} = \frac{\int_{\lambda_{start}}^{\lambda_{stop}} P_{inc}(\lambda)\eta^{rad}(\lambda)\eta^{mat}(\lambda)\mathrm{d}\lambda}{\int_{\lambda_{start}}^{\lambda_{stop}} P_{inc}(\lambda)\eta^{rad}(\lambda)\mathrm{d}\lambda} \tag{6}$$

where η^{mat} is the matching efficiency of the nantenna rectifier system as a function

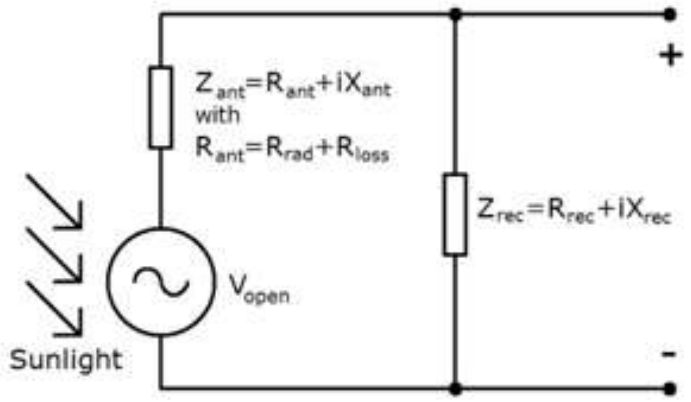

FIG. 3: Equivalent circuit for rectenna system.

of frequency. This parameter is calculated as

$$\eta^{mat} = \frac{4R_{rec}R_{ant}}{|Z_{rec} + Z_{ant}|^2} \tag{7}$$

where Z_{rec} is the impedance of the rectifier, Z_{ant} is the input impedance of the nantenna, R_{rec} is the real part of the rectifier impedance, and R_{ant} is the real part of the nantenna input impedance.

The optimization procedure works as follows. For each concrete topology considered, all the parameters related to the nantenna are calculated by the numerical solvers used. The impedance of the rectifier Zrec is then determined in the form of a second order polynomial with coefficients and with boundaries set for the possible range of the impedance values:

$$\left\{ \begin{array}{c} 2^{nd} : Z_{rec} = C^2_{rec}\lambda^2 + C^1_{rec}\lambda + C^0_{rec} \\ R^{min}_{ant} < Re\left(C^0_{rec}\right) < R^{max}_{ant} \\ -|X_{ant}|^{max} < Im\left(C^0_{rec}\right) < |X_{ant}|^{max} \end{array} \right\} \tag{8}$$

where R^{min}_{ant} and R^{max}_{ant} are the minimum and maximum of the nantenna resistance, and $|X_{ant}|^{max}$ is the maximum amplitude of the dipole reactance, respectively. The coefficients of this polynomial are optimized in such a way that the total matching efficiency θ^{mat}_{total} is maximized. A Particle Swarm Optimization (PSO) algorithm was chosen as the optimization tool.

TABLE I: Comparison between MAGMAS and Lumerical for a normal Al dipole (with $\phi = 0^o$).

Length of dipole, nm	Total efficiencies with MAGMAS			Total efficiencies with Lumerical		
	Radiation %	Matching %	Rectena %	Radiation %	Matching %	Rectena %
100	27.38	81.79	22.39	26.47	81.77	21.64
120	34.17	86.36	29.51	32.79	86.75	28.45
140	39.6	89.14	35.3	37.99	89.72	34.09
160	43.77	90.36	39.55	41.95	91.08	38.21
180	46.9	90.57	42.48	44.91	91.51	41.1
200	49.22	90.21	44.4	47.07	91.59	43.11
220	50.97	89.53	45.64	48.58	91.52	44.46
240	52.28	88.78	46.41	49.63	91.42	45.37
260	53.12	88.17	46.83	50.23	91.29	45.86
280	53.48	87.86	46.99	50.5	91.46	46.19
300	53.43	87.65	46.84	50.39	91.55	46.13
320	53.06	86.85	46.08	50.0	90.38	45.19
340	52.43	85.58	44.87	49.37	88.67	43.77
360	51.65	84.28	43.54	48.69	87.24	42.48
380	50.82	83.07	42.22	47.92	85.99	41.2
400	49.99	81.95	40.97	47.14	84.94	40.04

V. NUMERICAL RESULTS

In this section first the solver used in this work is compared to the solver mainly used in [13]. Then, simulation results are given for a systematic set of bow tie structures.

The result of the solver comparison is given in Table I. The case considered is $\phi = 0^o$. It is clearly seen that the two solvers agree extremely well, yielding a difference for the rectenna efficiency of maximum 1.3%. Since fabrication and measurements of nano antennas is extremely costly and time consuming, it is quasi mandatory to base analysis and design on full wave simulation tools.

Fig. 4 gives all relevant efficiencies for the bow tie topology: the total radiation efficiency, the total matching efficiency, and the rectenna efficiencies, respectively, for silver, gold and aluminum structures, as a function of the length and base angle of the bow tie. It is clearly seen that the total radiation efficiency has higher values for all three metals for base angles higher than 0^o. This is a clear indication that the bow tie is intrinsically better for harvesting applications. For each metal, the highest efficiencies can be found for a base angle between 35^o and 45^o and a dipole length

TABLE II: Maximum total radiation efficiency for normal (straight) dipole and bowtie topology.

Material	Straight Topology			Bowtie topology		
	L, nm	ϕ	θ^{rad}_{total}	L	ϕ	θ^{rad}_{total}
Ag	200	0^o	64%	300	45^o	80%
Au	220	0^o	35%	280	45^o	45%
Al	280	0^o	51%	280	40^o	61%

TABLE III: Maximum rectenna efficiency for normal (straight) dipole and bowtie topology.

Material	Straight Topology			Bowtie topology		
	L, nm	ϕ	θ^{rec}	L	ϕ	θ^{rec}
Ag	220	0^o	58%	300	45^o	72%
Au	240	0^o	32%	280	45^o	41%
Al	280	0^o	46%	240	30^o	57%

between $200nm$ and $350nm$. The total matching efficiency graphs are rather smooth for any metal. Efficiency values higher than 90% can be found for any base angle. Rectifier impedances were assumed optimal as explained in the previous section.

A comparison of the maximum total radiation efficiencies for $\phi = 0^o$ (normal dipole) and the overall maximum for the bow tie topology is shown in Table II for the three metals. It is clearly shown that the bowtie topology is able to increase the radiation efficiency by 16%, 10%, and 10% for silver, gold, and aluminum, respectively. For Silver, a very high resulting value of 80% is found.

A comparison of the maximum rectenna efficiency for $\phi = 0^o$ (normal dipole) and the overall maximum for the bow tie topology is shown in Table III for the three metals. The increase here is 14% for silver, 9% for gold, and 11% for aluminum. Minimal rectenna efficiency falls on gold with 41% and for other two metals, depending on angle and length, it is usually higher than 50%. Rectenna efficiencies of Ag and Al could be obtained in similar way in form tables.

The maximum rectenna efficiency reached is 72% for silver, 57% for aluminum, and 41% for gold. Note that although the efficiency of naked silver is considerably higher than for aluminum, this metal has clear advantages. First, the transparency of the oxide of aluminum is a great advantage. Second, the rectenna efficiency for aluminum is sensitive to varying length between $200nm$ and $340nm$, and base angle between 25^o and 40^o, yielding a considerable result always higher than 50%. This is illustrated in Table II and III.

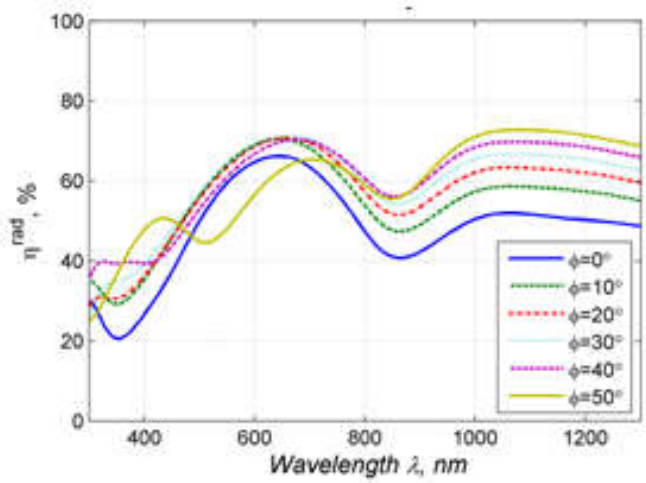

FIG. 4: Radiation efficiency of bowtie Al dipole as a function of wavelength (frequency) and base angle, $L = 240nm$.

The radiation efficiency, real part of input impedance, and imaginary part of input impedance of the optimal bowtie nantenna structures, both for Ag (length of $300nm$ and angle of 45^o) and Al, (length of $240nm$ and angle of 30^o) are plotted in Fig. 4.

VI. CONCLUSION

In this paper, a bowtie topology is considered as the nantenna in a rectenna for solar energy harvesting purposes. Its total rectenna efficiency is calculated for Ag, Au, and Al. It is shown that the bow tie topology is able to increase the total rectenna efficiency compared to the straight dipole nantenna by 10 to 15%. The final efficiencies reach an impressive 72% for silver and 57% for aluminum, which is about three and two times larger than for existing commercial silicon solar cells.

[1] R. L. Bailey, A proposed new concept for a solar energy convertor, J. Eng. Power 94 (1972) 73-77

[2] M. Sarehraz, K. Buckley, T. Weller, E. Stefanakos, S. Nhansali, Y. Goswami, K. Subramanian, Rectenna developments for solar energy collection, Photovoltaic Specialist Conference (2005) 78-81.

[3] Kempa, K., et al., Carbon nanotubes as optical antennae. Advanced Materials, 2007. 19(3): p. 421-+.

[4] M. N. Gadalla., Design, Optimization and Fabrication of a 28.3 THz Nano-Rectenna for Infrared Detection and Rectification, Scientific Reports 4 (March 2014), Article number: 4270.

[5] D.K. Kotter, S.D. Novack, W.D. Slafer, P.J. Pinhero, Theory and Manufacturing Processes of Solar Nanoantenna Electromagnetic Collectors, Journal of Solar Energy Engineering,(2010) Vol. 132 / 011014.

[6] G. A. E. Vandenbosch and Z. Ma, Upper bounds for the solar energy harvesting efficiency of nano-antennas, Nano Energy 1 (2012) 494-502

[7] W.C. Brown, The History of Wireless Power Transmission, Solar Energy, 56, 1996, pp. 3-21.

[8] P. Periasamy et al., Metal-Insulator-Metal Point-Contact Diodes as A Rectifier for Rectenna, Proceedings of 35th IEEE PVSC, 2010, pp. 1858-1861.

[9] R. Corkish, M. A. Green, and T. Puzzer, Solar Energy Collection by Antennas, Solar Energy, 73, 2002, pp. 395-401.

[10] J. Iijima, J.-W. Lim, S.-H. Hong, S. Suzuki, K. Mimura, M. Isshjiki, Native oxidation of ultra high purity Cu bulk and thin film, Applied Surface Science 253 (2006) 2825-2829

[11] Y. A. Akimov and W. S. Koh, Resonant and nonresonant plasmonic nanoparticle enhancement for thin film silicon solar cell, Nanotechnology 21 (2010) 235201

[12] E.Palik (ed.), Handbook of Optical Optical Constants of Solids, Academic Press, San Diego, 1985.

[13] Z. Ma and G. A. E. Vandenbosch, Optimal solar harvesting efficiency of nano rectenna systems, Nano Energy,Volume 88, February 2013, Pages 163174

[14] http://www.lumerical.com

[15] Z. Ma and G. A. E. Vandenbosch, Systematic full-wave characterization of real-metal, Nano Energy 1 (2012) 494-502

[16] M. Vrancken, G.A.E. Vandenbosch, IEEE Transactions on Antennas and Propagation 51 (10) (2003) 27782787.

[17] Y. Schols, G.A.E. Vandenbosch, IEEE Transactions on Antennas and Propagation 55 (4) (2007) 10861094.

GPU-accelerated simulation of SU(2) flux tube profiles

S. Chagdaa, G. Gombojav, E. Galsandorj
Laboratory of Lattice QCD, Department of Theoretical Physics,
Institute of Physics and Technology, Mongolian Academy of Sciences,
Peace Ave. 54b, Ulaanbaatar 13330, Mongolia

E. Laermann
Department of Theoretical High Energy Physics, Faculty of Physics,
University of Bielefeld, D-33615 Bielefeld, Germany

We present longitudinal and transverse profiles of the flux tube between static quarks at temperatures around the deconfinement transition. Exploiting the computational power of a GPU accelerator, we achieve a much higher statistics of our simulation and an improved signal to noise ratio. This has allowed to investigate larger lattices as well as larger separations between the quarks than in our previous work.

I. INTRODUCTION

Looking at behavior of matter when it undergoes the phase transition from confined to deconfined phase is still an appealing topic in high energy physics. In the confined phase quarks are bound together forming hadrons. A single isolated quark has never been observed in nature and any attempts to separate them were unsuccessful so far. Reason of this is that potential energy between two quarks rises linearly with the distance between them, which means isolating them would need infinite amount of energy. But there are numerical evidences that the slope of the linearly rising potential curve decreases as the temperature increases. We mainly are interested in the longitudinal and transverse profiles of the flux tube when it undergoes the phase transition.

Non-perturbative phenomena such as quark confinement can be most successfully studied by using the lattice gauge theories described on a lattice of space-time. Lattice numerical simulation has played an important role in the theoretical description of phenomena in high energy physics and Monte Carlo methods have proven to be very effective in its study.

A common special problem which one encounters in lattice numerical simulation is

that the signal gets drowned in the statistical noise when loop size is increased. For the flux tube simulation, it becomes difficult to get clear signal when $q\bar{q}$ separation is increased. Also the computation of expectation values and correlation functions of large Wilson loops is often extremely time consuming. As a result, the lattice numerical simulation of QCD is a highly demanding task computationally and requires advanced and powerful computers.

Generally, there are two ways of improving results of computer simulation. One can improve it by using advanced computer architectures or improving techniques used in simulation algorithms. In recent years computer power has increased quite dramatically and computer simulation algorithms have also been steadily refined. Here we have used the first method to reach much higher statistics of our simulation and an improved signal to noise ratio.

II. OBSERVABLES

Interactions between quarks are mediated by gluons which form flux tube. Therefore, exploring quark confinement means exploring the flux tube at the two ends of which a quark and an antiquark are located. Details of the interaction can be seen by scanning the nature of the flux tube by calculating the central observables that govern the events that take place in this region. They are the chromoelectric and chromomagnetic field strength components in the flux tube that can be extracted from the following Polyakov loop - plaquette correlations

$$f_{\mu\nu}(R,\mathbf{x}) = \frac{\beta}{a^4}\left[\frac{\langle L(0)L^+(R)\Box_{\mu\nu}(\mathbf{x})\rangle}{\langle L(0)L^+(R)\rangle} - \langle\Box_{\mu\nu}\rangle\right]. \tag{1}$$

Time propagation of the two static quarks sitting at the distance R from each other are represented by Polyakov loop L and its conjugate L^+. The plaquette variable $\Box_{\mu\nu}$ at distance $\mathbf{x}$ from the line connecting the $q\bar{q}$ pair, with the orientation μ,ν, measures the field strength $f_{\mu\nu}$. β is the coupling constant and a is the lattice spacing. Three space-space plaquettes correspond to magnetic components

$$f_{12} \to \frac{1}{2}(-B_\perp^2), \quad f_{13} \to \frac{1}{2}(-B_\perp^2), \quad f_{23} \to \frac{1}{2}(-B_\parallel^2) \tag{2}$$

and three space-time plaquettes correspond to electric components

$$f_{24} \to \frac{1}{2}E_{\perp}^2, \quad f_{34} \to \frac{1}{2}E_{\perp}^2, \quad f_{14} \to \frac{1}{2}E_{\parallel}^2. \tag{3}$$

The subscript $\parallel$ denotes the components that are oriented parallel to axis connecting the two sources, while $\perp$ denotes the components that are oriented perpendicular to the axis. Flux tube profiles thus can be extracted from Eq. 1 by varying the distance $\mathbf{x}$ and the orientation of the plaquette with respect to the Polyakov loops. We want to look at the longitudinal and transverse profiles of the components expressed in Eq. 2 and 3.

III. DETAILS OF THE SIMULATION

Pure gauge theory with gauge group SU(2) and standard Wilson action has been simulated on the lattice of size $32 \times 12^2 \times 6$. As we are interested in having larger $q\bar{q}$ separations we have used an extended number $N_{\parallel}$ of lattice sites in the direction of the $q\bar{q}$ axis. Update algorithms [1–5], the reference point [6] and link integration method [7] which were used in the previous work [8] for error reduction are kept the same.

We accelerate the generation of the gauge field configurations by executing the simulation program on a single NVIDIA GPU accelerator. Mapping of the lattice SU(2) gauge theory to the GPU by means of the CUDA programming model [9] is done by developing the code given in [10] by Cardoso and Bicudo.

Exploiting the computational power of the GPU accelerator, we were able to increase the number of our measurements to 400000. For the thermalization of the gauge configurations 10000 measurements have been used. Temperature and $q\bar{q}$ separation ranges at which the simulations have been performed are $0.75T_c - 1.29T_c$ and 0.4fm - 2.5fm, respectively.

IV. RESULTS

A. Longitudinal and transverse profiles

A Longitudinal profile shows how the field strength value is distributed along the direction parallel to the axis connecting q and $\bar{q}$. Longitudinal profiles at $x_\perp = 0$ of the parallel electric component $1/2E_{||}^2(R,x)$ are displayed on the left column of Fig. 1 at the given values of separation, namely at $R\sqrt{\sigma} = 1.6$, 2.0, 2.5, 2.8, 3.2 and 3.7 and their corresponding transverse profiles at $x_{||} = R/2$ are displayed on the right column of the figure at the same values of separation. The plotted results and the separation values are in units of the string tension.

Same plots for the parallel magnetic component are depicted in Fig. 2. Here we confirm with higher accuracy that $E_\perp \approx B_\perp \approx B_{||} < E_{||}$ also at high temperature. Thus, we have chosen only parallel components to show in the figures.

For the plots in the left column of the figures one quark source is placed at $x_{||}\sqrt{\sigma} = 0$ and another one is at distance $R\sqrt{\sigma}$ from it. Blue star points correspond to the data at lower temperature, while red square points correspond to the data at higher temperature. There are pink circle points only on the plots for the largest two separations of both Fig. 1 and 2, which denote the data at a temperature higher than that of the red one for that plots.

The reason why there are only two to three data differing in temperature for each plot, while we have performed the simulation at five values of the parameter T is the fact that $q\bar{q}$ separations that were equal in lattice units will be no longer equal in physical units. Because it is expressed as Ra and a takes a different value for each β. Thus collecting data with matching physical values of separation but different temperatures in order to compare results at a fixed value of Ra gives the reduced number of data to be compared.

As one reads the plots going down the parameter separation value $R\sqrt{\sigma}$ increases from 1.6 to 3.7. If one looks at the central region between the two sources one can see that the field strength value at the middle point between the two sources decreases with rising temperature and the distribution approaches the one of two isolated quarks as the temperature goes to T_c. Increase in separation accelerates the decreasing process with temperature.

Drop in the middle point value is clearly visible in the transverse profile plots. For

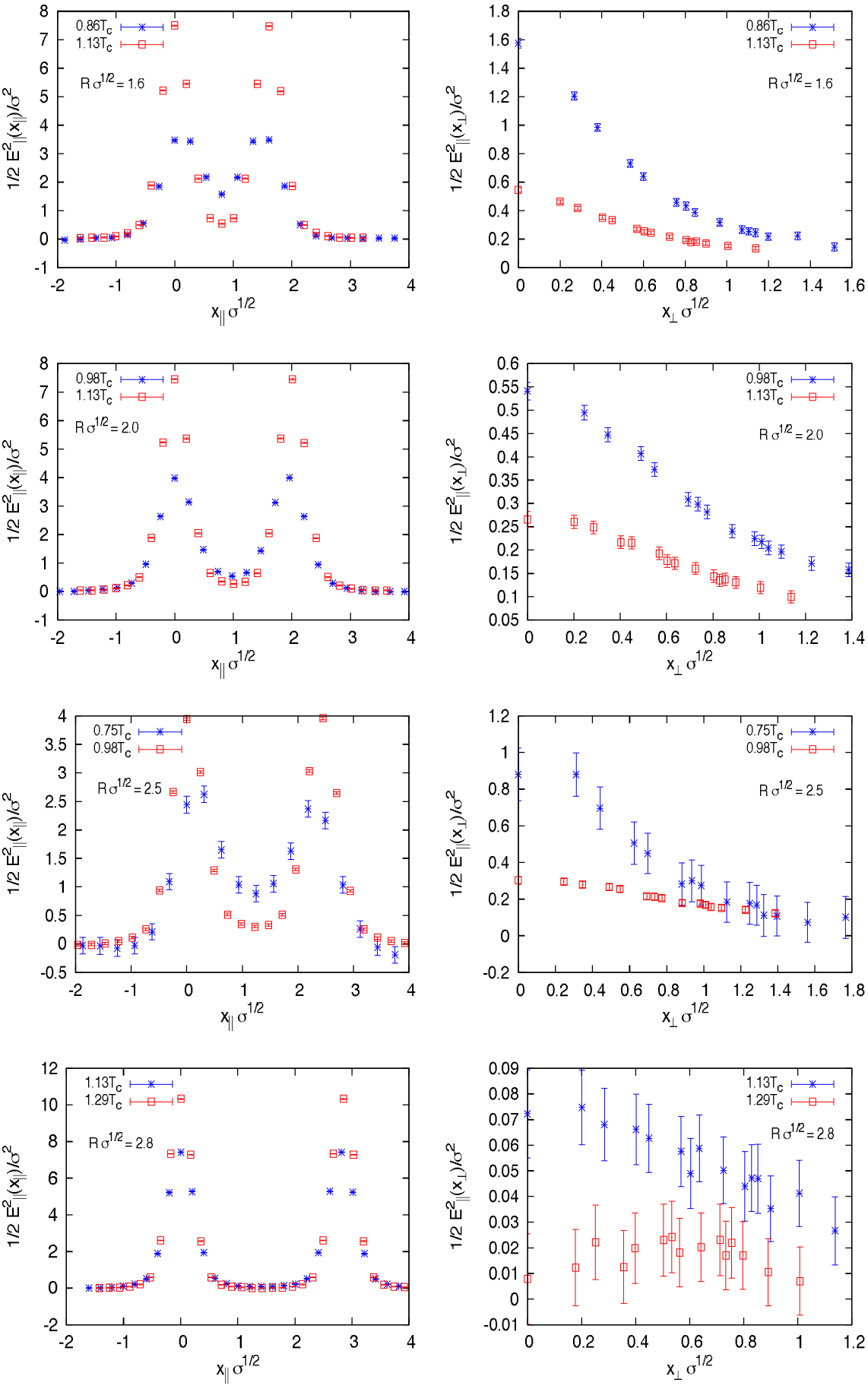
0.86T_c
1.13T_c
Rσ^1/2 = 1.6
1/2 E^2_∥(x_∥)/σ^2
x_∥ σ^1/2
0.86T_c
1.13T_c
Rσ^1/2 = 1.6
1/2 E^2_∥(x_⊥)/σ^2
x_⊥ σ^1/2
0.98T_c
1.13T_c
Rσ^1/2 = 2.0
1/2 E^2_∥(x_∥)/σ^2
x_∥ σ^1/2
0.98T_c
1.13T_c
Rσ^1/2 = 2.0
1/2 E^2_∥(x_⊥)/σ^2
x_⊥ σ^1/2
0.75T_c
0.98T_c
Rσ^1/2 = 2.5
1/2 E^2_∥(x_∥)/σ^2
x_∥ σ^1/2
0.75T_c
0.98T_c
Rσ^1/2 = 2.5
1/2 E^2_∥(x_⊥)/σ^2
x_⊥ σ^1/2
1.13T_c
1.29T_c
Rσ^1/2 = 2.8
1/2 E^2_∥(x_∥)/σ^2
x_∥ σ^1/2
1.13T_c
1.29T_c
Rσ^1/2 = 2.8
1/2 E^2_∥(x_⊥)/σ^2
x_⊥ σ^1/2

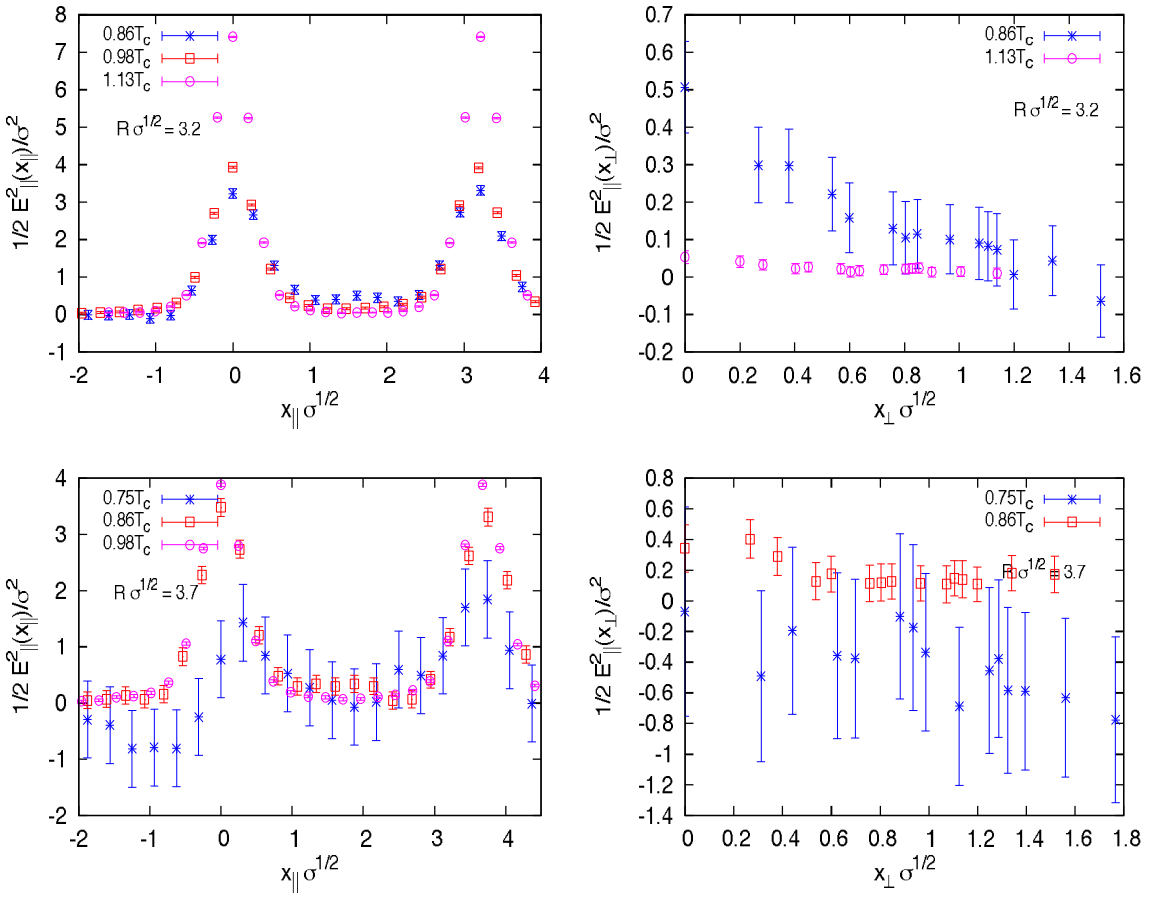

FIG. 1: **(Left:)** Longitudinal profiles $1/2E^2_{\|}(x_{\|}, x_{\perp} = 0)$ and **(Right:)** transverse profiles $1/2E^2_{\|}(x_{\|} = R/2, x_{\perp})$ at the given values of R from the lattice of size $32 \times 12^2 \times 6$.

a transverse profile, the initial point at $x_{\perp}\sqrt{\sigma} = 0$ corresponds to the middle point between the two sources and its value vanishes as a function of $x_{\perp}\sqrt{\sigma}$ for a given T. When T increases the initial point for the transverse profile but the middle point for the longitudinal profile drops from around 1.6 to 0.6 for $1/2E^2_{\|}/\sigma^2$ at $R\sqrt{\sigma} = 1.6$ in Fig. 1 for example. Same feature holds for other values of separation as well as for the magnetic component depicted in Fig. 2.

B. Potential and the string tension

From above plotted data we have computed the color averaged potential between a quark and an antiquark pair by using the equation

$$\langle L(\vec{0})L^{+}(\vec{R})\rangle = e^{-V(|\vec{R}|,T)/T} \tag{4}$$

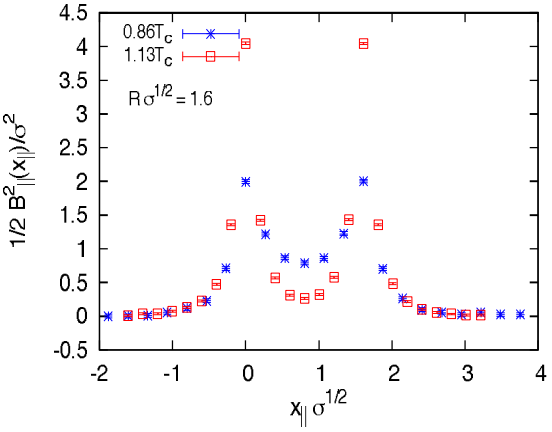
0.86T_c
1.13T_c
Rσ^1/2 = 1.6
1/2 B^2_∥(x_∥)/σ^2
x_∥ σ^1/2

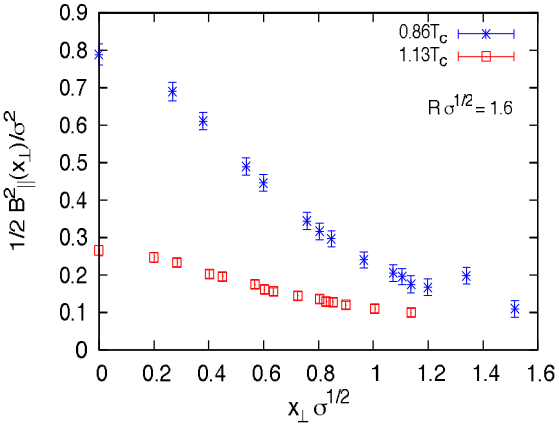
0.86T_c
1.13T_c
Rσ^1/2 = 1.6
1/2 B^2_∥(x_⊥)/σ^2
x_⊥ σ^1/2

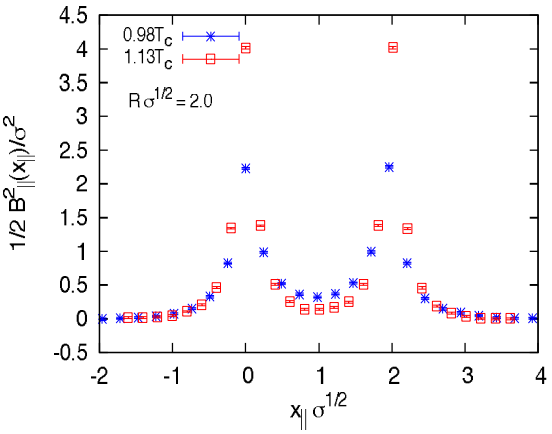
0.98T_c
1.13T_c
Rσ^1/2 = 2.0
1/2 B^2_∥(x_∥)/σ^2
x_∥ σ^1/2

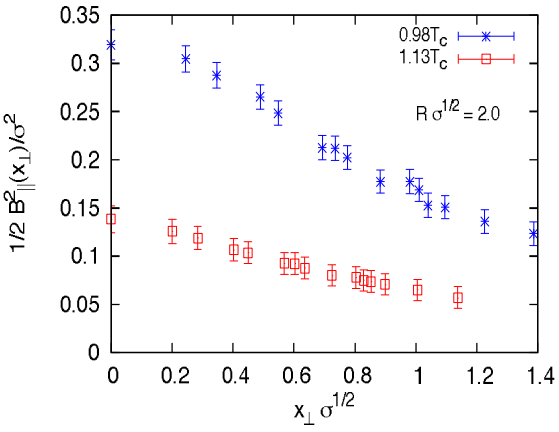
0.98T_c
1.13T_c
Rσ^1/2 = 2.0
1/2 B^2_∥(x_⊥)/σ^2
x_⊥ σ^1/2

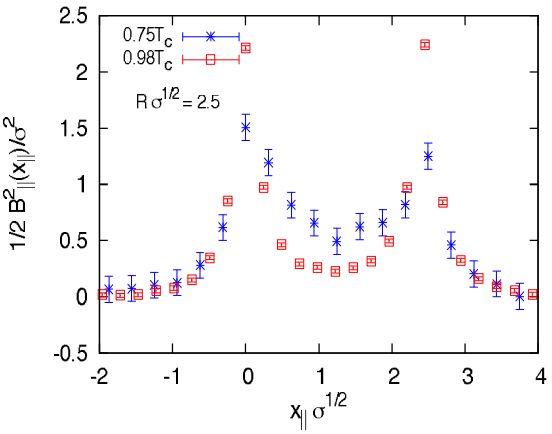
0.75T_c
0.98T_c
Rσ^1/2 = 2.5
1/2 B^2_∥(x_∥)/σ^2
x_∥ σ^1/2

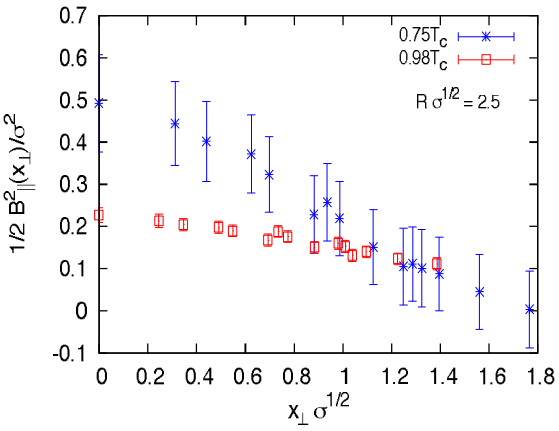
0.75T_c
0.98T_c
Rσ^1/2 = 2.5
1/2 B^2_∥(x_⊥)/σ^2
x_⊥ σ^1/2

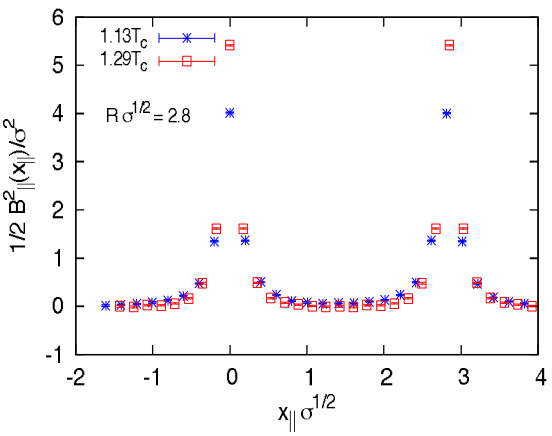
1.13T_c
1.29T_c
Rσ^1/2 = 2.8
1/2 B^2_∥(x_∥)/σ^2
x_∥ σ^1/2

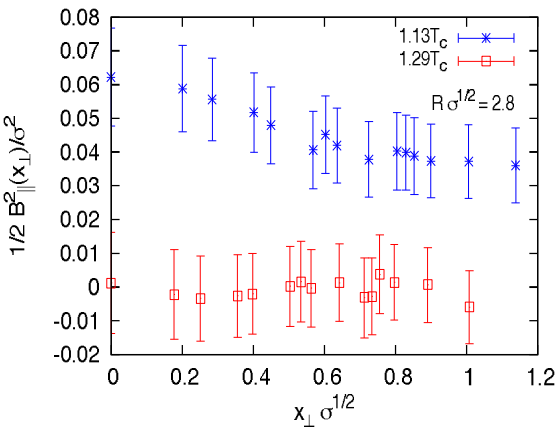
1.13T_c
1.29T_c
Rσ^1/2 = 2.8
1/2 B^2_∥(x_⊥)/σ^2
x_⊥ σ^1/2

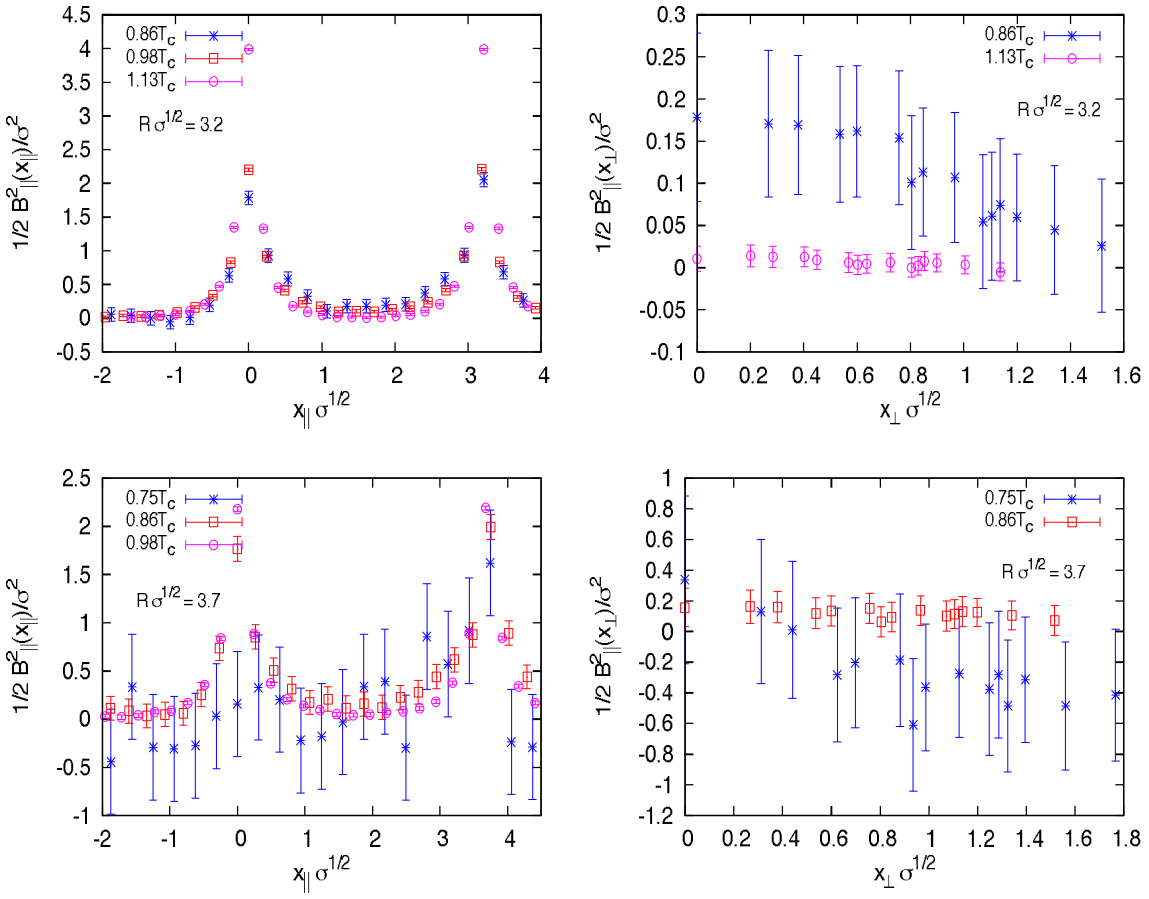

FIG. 2: **(Left:)** Longitudinal profiles $1/2B^2_{\|}(x_{\|}, x_\perp = 0)$ and **(Right:)** transverse profiles $1/2B^2_{\|}(x_{\|} = R/2, x_\perp)$ at the given values of R from the lattice of size $32 \times 12^2 \times 6$.

and the results are shown in Fig. 3 in lattice units. The figure shows the potential as a function of R, the range of which is $4a - 16a$, for various temperatures. Our data confirm what we already know from quark confinement that the potential between q and $\bar{q}$ rises linearly with the distance between them. The slope of the potential curve decreases when temperature increases, meaning that the string tension is no longer constant but is temperature dependent.

These potentials have been fitted to three potential forms

$$V_1(R,T) = V_0 - \left[\frac{\pi}{12} - \frac{1}{6}\arctan(2RT)\right]\frac{1}{R} + \Bigg[\sigma - \frac{\pi}{3}T^2 + \frac{2}{3}T^2 \arctan\left(\frac{1}{2RT}\right)\Bigg]R + \frac{T}{2}\ln[1+(2RT)^2], \tag{5}$$

$$V_2(R,T) = V_0 + \sigma(T)R + \gamma T \ln(2RT) \tag{6}$$

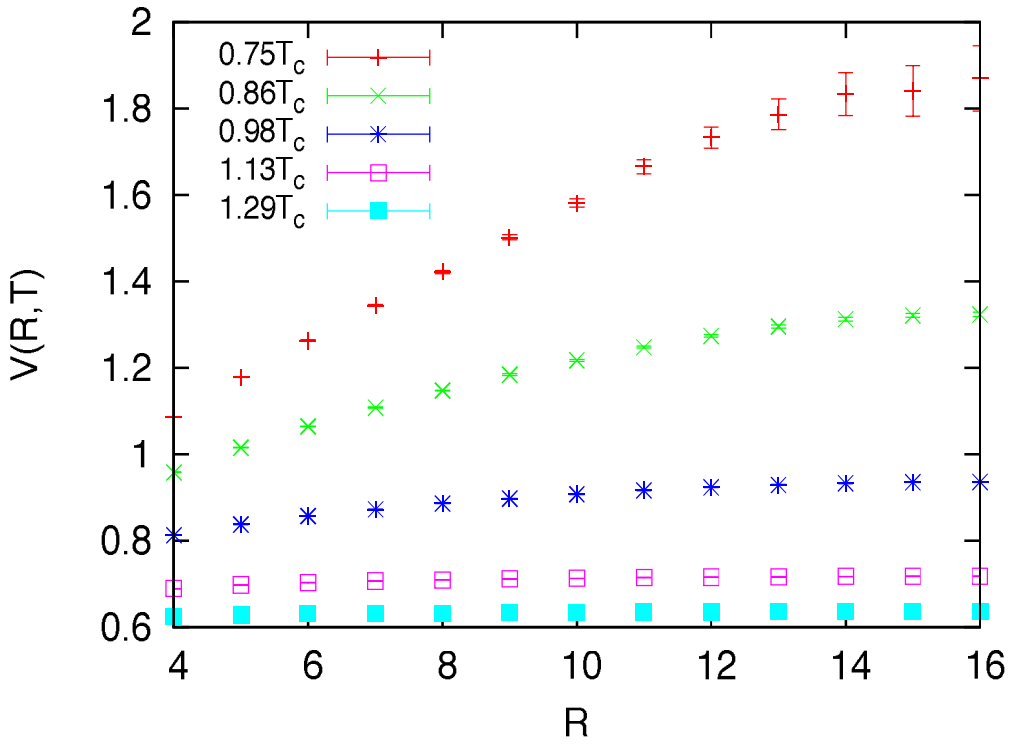

FIG. 3: The linearly rising potential between $q\bar{q}$ pair at various temperatures around T_c from the lattice of size $32 \times 12^2 \times 6$.

TABLE I: Results for the free parameters from fit of the potential to Eq. 5.

N_τ	β	T/T_c	aV_0	$a^2\sigma$	χ^2
	2.35	0.75	0.94(2)	0.091(2)	12.89
	2.39	0.86	0.96(1)	0.055(1)	172.73
6	2.43	0.98	0.876(5)	0.0340(4)	153.46
	2.47	1.13	0.7501(5)	0.02812(5)	10.08

and

$$V_3(R,T) = V_0 - \frac{\alpha}{R} + \sigma(T)R \tag{7}$$

in order to extract T-dependent string tension values, first allowing for a temperature dependent string tension instead of zero temperature string tension in Eq. 5 and then accounting for a logarithmic behavior with Eq. 6 and thirdly accounting for a Coulomb type behavior for small $q\bar{q}$ separations with Eq. 7. The fit results are displayed in the Table. I, II and III, respectively.

The resulting string tension values in the Table. I can be compared with zero temperature string tension values, obtained from renormalization group inspired in-

TABLE II: Results for the free parameters from fit of the potential to Eq. 6.

N_τ	β	T/T_c	aV_0	$a^2\sigma(T)$	γ	χ^2
	2.35	0.75	0.84(1)	0.0099(97)	2.98(52)	3.14
	2.39	0.86	0.841(8)	-0.013(4)	2.51(25)	16.80
6	2.43	0.98	0.785(2)	-0.0085(8)	1.01(5)	6.74
	2.47	1.13	0.6894(2)	-0.00220(6)	0.231(4)	0.23

TABLE III: Results for the free parameters from fit of the potential to Eq. 7.

N_τ	β	T/T_c	aV_0	$a^2\sigma(T)$	α	χ^2
	2.35	0.75	1.40(10)	0.036(6)	2.25(45)	3.95
	2.39	0.86	1.33(5)	0.008(2)	2.01(25)	26.12
6	2.43	0.98	0.99(1)	-0.0005(6)	0.84(6)	15.19
	2.47	1.13	0.737(2)	-0.00039(8)	0.197(9)	1.36

terpolation ansatz to data from [11] and also with our previous fit results in [8]. The string tension values as determined from these fits are decreasing with temperature confirming T-dependent string tension at non-zero temperature.

V. CONCLUSION

We have studied distribution of chromoelectric and chromomagnetic field strength components in the flux tube connecting a quark and an antiquark sources by means of the lattice numerical simulations. Longitudinal and transverse profiles of the distribution have been extracted from Polyakov loop - plaquette correlations at the temperatures around the deconfinement phase transition. The field strength value at the middle point between the two sources clearly decreases with rising temperature. By improving performance of SU(2) flux tube simulation program parallelizing it on a NVIDIA GPU accelerator, we were able to reach much higher statistics of our simulation. This enabled us to obtain clear signal of longer flux tubes with larger separations which were unreachable during our previous simulations performed on CPU. Field strength distribution values and the T-dependent string tension values in the flux tube have been redetermined with higher accuracy. As precision is improved, the string tension values tend to decrease compared to the previous results.

Acknowledgments

We would like to acknowledge the Ministry of Education, Culture and Science of Mongolia for their approval to execute this project. We also thank Mongolian Foundation for Science and Technology for their full financial support throughout the project, the financial contract number of which is SSA 019/14. This paper is dedicated to memory of Dr. Orlokh Dorjkhaidav, who made a noteworthy contribution to bringing along for the first time the high-performance computer to the laboratory as was the administration of the institute.

[1] M. Creutz, *Monte Carlo Study of Quantized SU(2) Gauge Theory*, Phys. Rev. D 21, 2308, 1980.

[2] M. Creutz, *Confinement and the Critical Dimensionality of Space-Time*, Phys. Rev. Lett. Vol. 43, 553, 1979.

[3] A. D. Kennedy and B. J. Pendleton, *Improved Heatbath Method for Monte Carlo Calculations in Lattice Gauge Theories*, Phys. Lett. B 156, 393, 1985.

[4] M. Creutz, *Overrelaxation and Monte Carlo Simulation*, Phys. Rev. D 36, 515, 1987.

[5] P. Forcrand and O. Jahn, *Monte Carlo Overrelaxation for SU(N) Gauge Theories*, [hep-lat/0503041].

[6] R. W. Haymaker and Y. Peng, *SU(2) Flux Distributions on Finite Lattices*, Phys. Rev. D 47, 5104, 1993.

[7] G. Parisi, R. Petronzio and F. Rapuano, *A Measurement of the String Tension Near the Continuum Limit*, Phys. Lett. B 128, 418, 1983.

[8] S. Chagdaa, *Flux Tube Profiles at High Temperature*, Doctoral dissertation, Bielefeld University, 2008.

[9] NVIDIA, NVIDIA CUDA Programming Guide, 3rd Edition, 2010.

[10] N. Cardoso and P. Bicudo, *SU(2) Lattice Gauge Theory Simulations on Fermi GPUs*, Journal of Computational Physics, 230, 3998, 2011.

[11] J. Engels, J. Fingberg and D. Miller, *Phenomenological Renormalization and Scaling Behaviour of SU(2) Lattice Gauge Theory*, Nucl. Phys. B 387, 501, 1992.

Kinetic study of coal under heat treatment

S. Munkhtsetseg

*Department of Physics, School of Arts & Sciences, National University of Mongolia, University Street-1, 210646 Ulaanbaatar, Mongolia**

The high temperature has been set up directly in the resonator. Established thermal reaction allows detecting transient, short lived, highly reactive radicals. Brown (lignite) coals such as Tevsh, Tugrug and Khotgor showed the similar behavior in the heat treatment. However, it is complicated for the high rank coals in the used temperature. The complexity structure of coal is independently of the coal rank, the microwave power and temperature used.

I. INTRODUCTION

Coals come to be distributed in various parts of Mongolia with over 152 billion tons of coal reserves, mainly lignite, brown and bituminous metamorphism [1]. So far, the country coal use has been mainly for the nation's electricity generation, precisely, the electricity and heating supply is directly from coal burning in electro stations and homes over the years and this will stay as the largest single source of overall domestic energy production in the nearest future. This has been called the investigation on Mongolian coal structure and chemical processing [2–16] and it will increase with a growing demand of an interest on coal mining. Furthermore, for the proper use of national wealth such as a coal which can be converted through proven, existing modern technology into clean coal it is highly required to push the structural analysis of Mongolian coals in an advanced level.

For the characterization of coal, the coal rank studies, the type of organic (e.g. macerals) and inorganic (e.g. minerals, trace elements) constituents within coal play significant role. In addition, for energy production applications the essential properties such as calorific value, volatile matter, moisture content, elementals (carbon, hydrogen, oxygen, sulphur, nitrogen) content and behavioral characteristics as a liq-

*Electronic address: munkhtsetseg_s@num.edu.mn

uefaction yields', coking propensity and combustion efficiency are in basic interest.

In the latter case the paramagnetic centers naturally present in coal can serve as probes to study local properties without affecting the original composition of coal. In the present work a high temperature electron paramagnetic resonance (EPR) spectroscopy is applied to study coals and their reaction. The heat treatment on coal samples inside the EPR cavity has the capability of monitoring thermally induced transient free radicals in coals.

II. EXPERIMENTAL

Samples. Six coal samples from the different Mongolian coal deposits were studied by EPR spectroscopy.

Sample mass is measured on the Mettler Toledo AE 260 micro balance and size on SMZ-140 series Stereomicroscope with magnification range 40. Sample preparation for the analysis was performed in accordance with standard procedures of coal chemistry: the samples were mixed, crushed initially in a breaker and then in a mill to a size of 0.05 mm or less for elemental analysis measurement and to a size of up to 5 mm for spectroscopic analysis.

Further the coals in this work were grouped into their provenance by basins or areas in the country which can be the followings: Western Mongolian province (Mongol Altai, Valley of Great Lakes), Southern Khangai, Ikh Bogd, and Ongi river basins (Valley of Lakes), South Gobi basin (Southern Mongolia), Orkhon-Selenge area (Central and Northern Mongolia) and Eastern Mongolian province (Eastern Mongolia) how determined in [5].

Grouped coal places and their deposit names and as well as the element contents are given in the table 1 . The determination of the elements C, H, N, O and S is carried out with instruments of the company LECO at the Micro Laboratory for Organic Chemistry (ETH, Zurich). The samples were digested first and the combustion products – carbon (CO_2), hydrogen (H_2O), sulfur (SO_2) and oxygen (CO_2) are analyzed quantitatively by infrared spectroscopy. Nitrogen (N_2) is determined by a thermal conductivity detector. These variables are measured in weight percent (wt. %) and are calculated in the air–dried (ad) base.

EPR measurement. Measurements were performed with a Bruker Elexsys II E500 spectrometer (ETH, Zurich) equipped with a high–temperature EPR cavity. Exper-

TABLE I: Elemental analysis of coals

Basin/ Area	**Coal deposit/ sample**	C^{ad}, **wt.%**	H^{ad}, **wt.%**	O^{ad}, **wt.%**	N^{ad}, **wt.%**	S^{ad}, **wt.%**
Eastern Mongolian province	Tevsh (Te)	51.13	5.47	35.40	0.77	0.36
	Tugrug (Tu)	59.41	3.28	3.92	1.45	0.34
Southern Khangai, Ikh Bogd, and Ongi river basins	Khotgor (Kho)	68.20	4.56	11.08	2.03	0.40
Western Mongolian province	Maanit (Ma)	74.75	5.56	9.14	1.65	0.47
	Khushuut (Khu)	80.85	4.09	5.79	2.07	0.33
Central and Northern Mongolia	Saikhan-Ovoo (SO)	84.26	2.84	5.94	2.21	0.35

iments are conducted at a frequency 9.20 GHz and modulation of 100 kHz provided by the modulation unit. A microwave power of 30 dB is used throughout the measurements.

The spectrometer was equipped with a super high Q-factor resonator (ER 4122 SHQE) which has a cylindrical shape TE011 cavity. For a standard procedure, 20 mg samples a size of ~ 0.05 mm or less placed in a 0.4 mm quarts EPR sample tube, which was inserted directly into the high–temperature cavity.

Modulation amplitude and time constant of EPR registration were chosen from well-known requirements for undistorted registration of the first derivative resonance absorption signal by magnetic induction.

EPR spectra of the studied coals were registered as the first derivative of the microwave absorption versus applied magnetic field. The parameters of the EPR spectra: g–factor, linewidth (ΔH_{pp}) and integral intensity (I_{pp}) were evaluated. g–factor was determined as $g = h\nu/\beta H_r$, where h is the Planck constant, β the Bohr magneton, ν the microwave frequency, and H_r is the resonance magnetic induction. The linewidth (ΔH_{pp}) was determined as the difference of field positions of maximum and minimum of the first derivative EPR spectrum. The integral intensity (I_{pp}) is the distance between maximum and minimum of the first derivative EPR spectrum. Heating available temperature range was from room temperature ($\sim 26^0C$) to 500^0C. To prevent oxidation by air, the sample tube was degassed at low vacuum (a few

pascals) and flowed by nitrogen gas (kept at a constant flow rate).

In this experiment, the only relevant ESR–parameter is the peak–to–peak amplitude of the first derivative signal in arbitrary units, taken as a measure of the number of radicals in the sample. The EPR spectrum was measured at every 50^0C and during heating and cooling (after heat treatment) room temperatures as well. EPR microwave power saturation was measured at every 100^0C heating temperatures.

EPR spectra of the coals were first measured at room temperature and after the samples were cooled EPR spectra also were measured at room temperature. Simulation of EPR spectra was done using the Matlab package EasySpin [17].

III. EPR MEASUREMENT RESULT AND DISCUSSION

Changes in the EPR parameters, such as peak–to–peak amplitude (I_{pp}), linewidth (ΔH) and g–factor, at room temperature before heating and cooling of the studied coals can be seen in the table 2.

TABLE II: EPR parameters at room temperature (1 – heating and 2 – cooling)

Coal sample	**EPR parameters**						
	I_{pp}/I_{ppmax}		$I_{pp}(1)/I_{pp}(2)$	ΔH_{pp}, Gs		g-factor	
	1	2		1	2	1	2
Tevsh	0.005	0.018	0.277	6.45	6.84	2.0075	2.0073
Tugrug	0.098	0.219	0.447	1.61	1.20	2.0028	2.0028
Khotgor	1	0.012	83.33	2.10	11.24	2.0013	2.0029
Maanit	0.001	0.072	0.014	7.09	3.86	2.0074	2.0073
Khushuut	0.051	1	0.051	4.49	0.93	2.0035	2.0035
Saikhan–Ovoo	0.007	0.693	0.010	1.61	2.08	2.0045	2.0031

The EPR spectra of coals registered at room temperature before heat treatment and cooling are shown in figure 1.

Figure 2 shows the general profile of peak–to–peak amplitude as a function of temperature for the studied coals.

The dependence between the temperature and the peak–to–peak amplitude corresponds to the Curie law for the high carbon contained coals Maanit, Khushsuut and Saikhan–Ovoo (Table 2, cooling from 500^0C to room temperature) but contradictious for the lignite coals such as Tugrug, Tevsh and Khotgor.

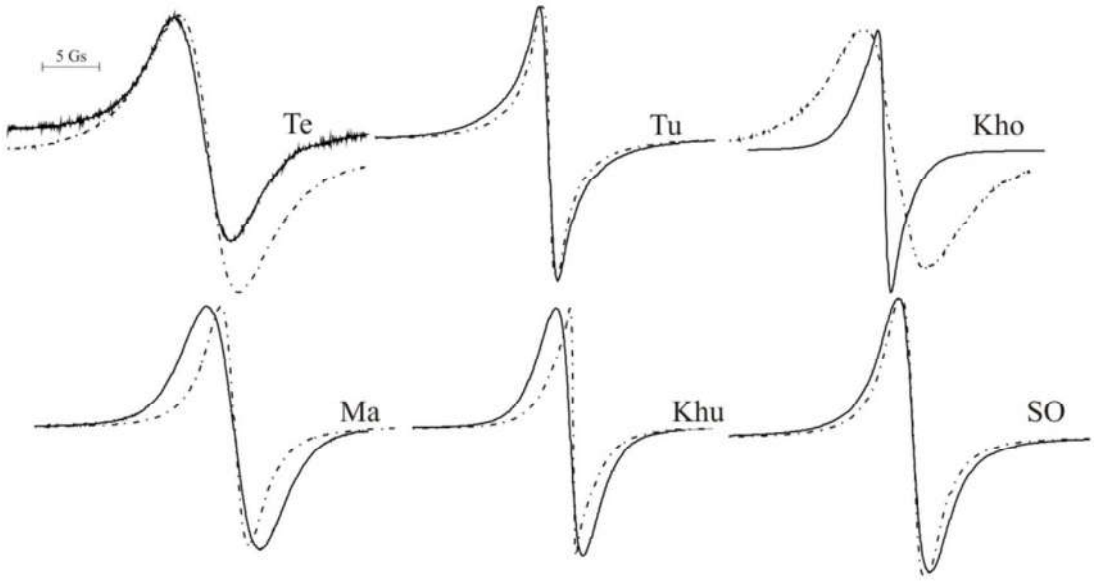

FIG. 1: Normalized EPR spectra of coals (solid line spectrum – before heating and dashed line spectrum – cooling/after heating. Abbreviations of coal sample names are quoted from table 1.

These dependences behave similarly with maximum around $200 - 300^0C$ for the lignites Tevsh and Tugrug and subbituminous Khotgor coal. This increase can be correlated with the weak bonds such as benzyl phenyl ether type C–O linkages or dibenzyl type C–C bonds dissociation in coal structure [18, 19]. Further, a decrease of the amplitude till 500^0C causing the major loss of hydrogen is observed. This bond breakup point could not been reached in the used temperature for the bituminous coals (Saikhan–Ovoo, Khushuut and Maanit).

Temperature dependence for these coals behaves differently. Its peak–to–peak amplitude is high from room temperature up to 300^0C and goes abruptly down at high temperatures for Saikhan–Ovoo coal. Saturation curve presents the disappearance of the narrow line from this temperature. This phenomenon can be observed in Maanit coal at 500^0C where it has maximum point of amplitude and appearance of the narrow EPR line.

The observed changes in linewidth were relatively small in Tevsh, Tugrug, and Saikhan-Ovoo. The linewidth has strongly broadened in Khotgor coal. Generally, linewidth dependence versus temperature plots the jumps from 26 to 100^0C (fig 3). Despite the tendency of line width broadening for Tevsh and Tugrug and decreasing for Khotgor and Khushuut coals in the up going temperature can be considered. g–factor decreases in the increasing temperature for the coals. In Khotgor coal g–factor

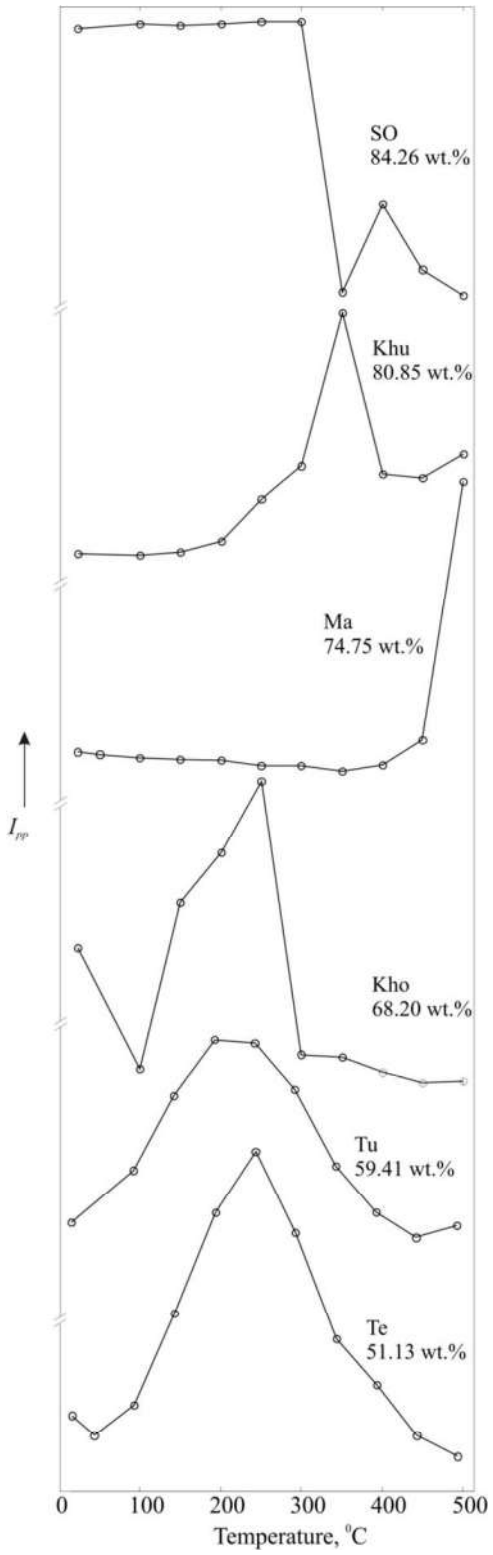

FIG. 2: Temperature dependence on peak–to–peak amplitude of EPR spectra of coals.

increases large from 400 to 500^0C. The saturation measurement of these coals at every 100^0C temperatures behaved differently for each coal. In the figures 4 below show the power saturations for each coal. For Tevsh coal the EPR is singlet and

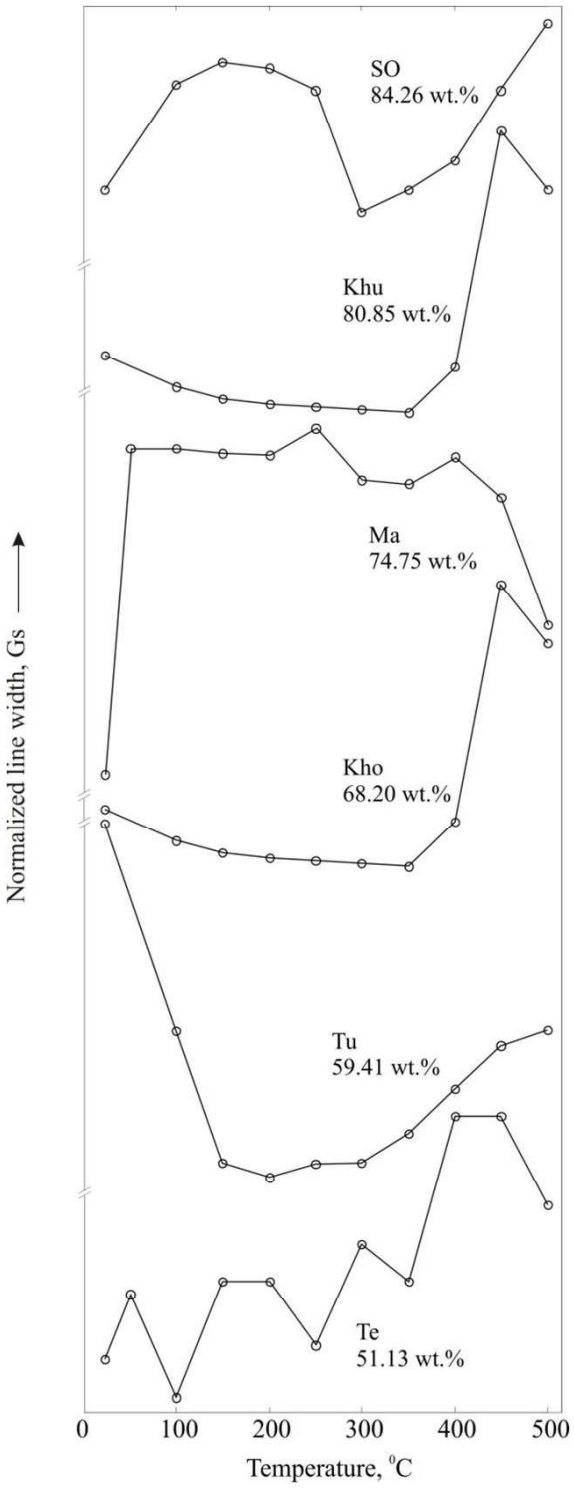

FIG. 3: Temperature dependence of normalized EPR spectra line width of coals

all dependences from room temperature to 500^0C are homogeneous and saturated, presenting the maximum at the lower power level, following a considerable EPR intensity quench (fig 4 Te: dependences 1–6). EPR spectrum of Tugrug coal consists of two components (broad and narrow) at high power level. The saturation at all

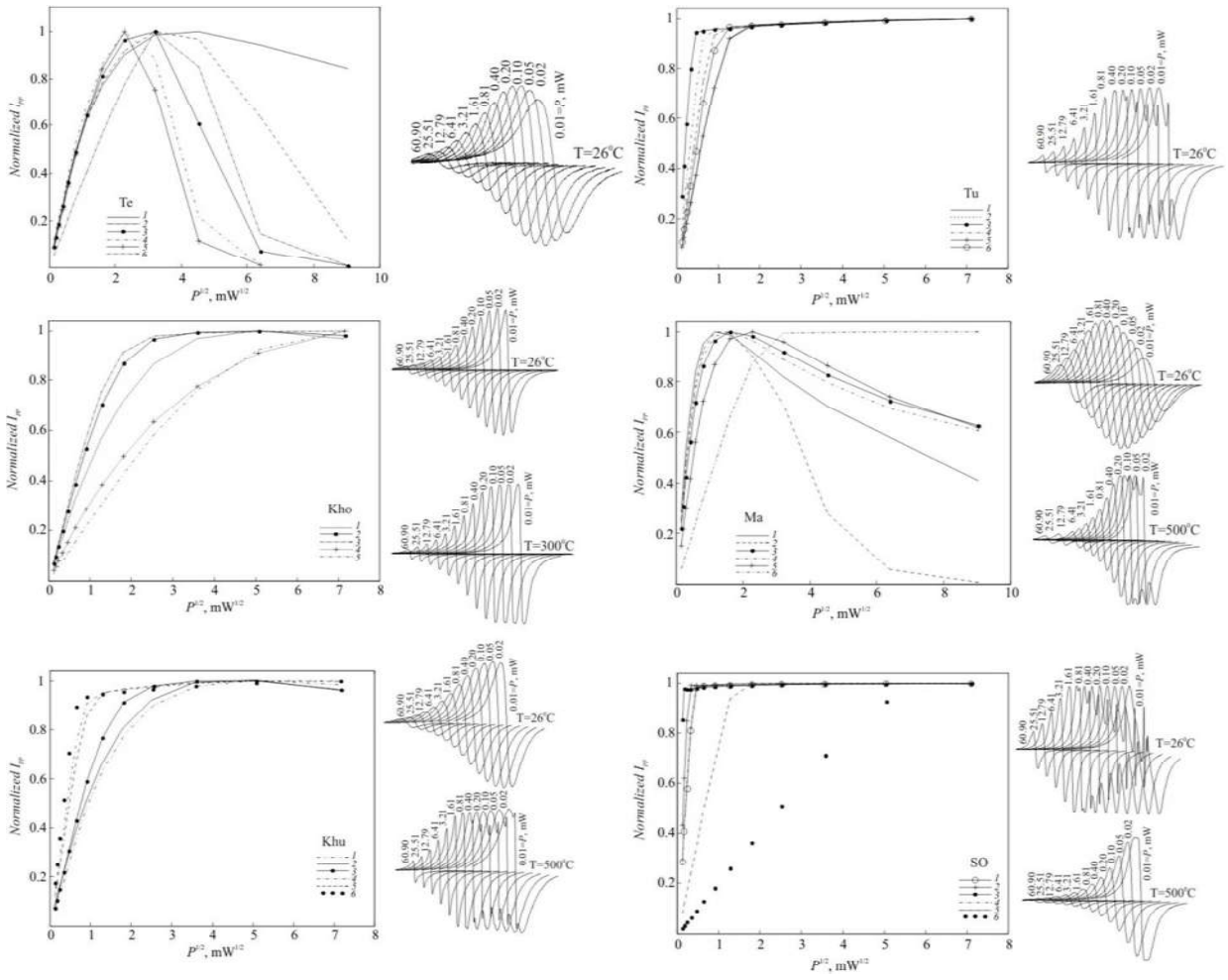

FIG. 4: Power saturation curves for studied coals at different temperatures (1 – room temperature ($\sim 26^0C$), 2 – 100^0C; 3 – 200^0C; 4 – 300^0C; 5 – 400^0C; 6 – 500^0C)

temperatures is exhibiting leveling that no having subsequent decrease in EPR signal amplitude (fig 4 Tu: dependences 1–6).

At lower temperatures (from 26 to 200^0C) EPR spectrum homogeneously saturated with maximum at high power ($\sim$ 25 mW) on Khotgor coal (fig 4 Kho: dependences 1–3). At 300^0C this singlet spectrum slightly broadens at high power. From 400^0C the homogeneous saturation degree is getting smaller that can be caused the appearance of the spins with short relaxation time (fig 4 Kho: dependences 4–6).

From room temperature up to 400^0C the homogeneous saturation with exhibition of maximum at low power level were observed for Maanit coal (fig 4 Ma: dependence 1–5), but at 500^0C the EPR spectrum was split to two components and the saturation curve leveled at high level of powers (fig 4 Ma: dependence 6). Homogeneous, single spectrum at room temperature of the Khushuut coal starts to split to two parts from temperature 100^0C. EPR spectra consist of two components show the similar behavior

of saturation that it saturated at lower power and keeps the EPR signal intensity (fig 4 Khu: dependence 1–6). At higher microwave power levels at temperature interval of $26 - 400^0C$ EPR spectrum of the Saikhan–Ovoo coal is a two–component and the spectrum saturated at low power levels (fig 4 SO: dependence 1–5). At 500^0C the spectrum saturated at highest power level showing splitting on it.

IV. CONCLUSION

In the conclusion, one can consider that the established thermal reaction allow to detect transient, short lived, highly reactive radicals. Brown (lignite) coals show the similar behavior in the heat treatment. However, it is complicated for the high rank coals in the used temperature. The paramagnetic centers related to the singlet EPR spectrum of brown (lignite) Tevsh coal is the most homogeneous type among the studied coals. The complexity structure of coal is independently of the coal rank, the microwave power and the temperatures used. The "natural" asymmetry of the EPR line of Khotgor coal can be not due to the complex structure of the organic matter. Therefore, the paramagnetic centers with low concentration and short relaxation time appeared at high temperatures (400 and 500^0C) might be the effect of ash content.

Acknowledgments

Author is very thankful to Prof. Gunnar Jeschke and EPR spectroscopy laboratory at ETH Zurich.

[1] Purevsuren B. Coal is the main source of energy in Mongolia, Second Korean and Mongolian Energy Conference. Seoul, Korea: Yonsei University. 2007, P. 13

[2] T. Tsedevsuren, T.A. Titova, E.A. Dembavskaya. Hydrogenation of Bayanteeg coal of Mongolia, Chemistry of Solid Fuels (Russian Academy of Science). 1981, 6, P. 17–9

[3] P. Ochirbat Coal industry development strategy and ecology, Ecology and Stability Development Center, Mountain and Mining Engineering School of University of Mongolian Science and Technology, "INTERPRESS" printing. Ulaanbaatar. 2002, P. 378

[4] B. Avid, B. Purevsuren, N. Paterson, Y. Zhuo, D. Peralta, A. Herod, D. R. Dugwell, R. Kandiyoti An exploratory investigation of the performance of Shivee-Ovoo coal and Khoot oil shale from Mongolia, Fuel. 2004, 83(7–8), P. 1105–1111

[5] Bat–Orshikh Erdenetsogt, Insung Lee, Sung Keun Lee, Yoon–Joo Ko, Delegiin Bat–Erdene Solid–state C–13 CP/MAS NMR study of Baganuur coal, Mongolia: Oxygen–loss during coalification from lignite to subbituminous rank, International Journal of Coal Geology. 2010, 82(1–2), P. 34–44

[6] B. Avid, Y. Sato, K. Maruyama, Y. Yamada, B. Purevsuren Effective utilization of Mongolian coal by upgrading in a solvent, Fuel Processing Technology. 2004, 85, P. 933945

[7] S. Munkhtsetseg, N.A. Poklonski, N.M. Lapchuk, A.V. Khomich, G. Shilagardi, S. Erdenebat Paramagnetism of Mongolian coals, The 2^{nd} international symposium on physics and high–tech industry (ISPHTI'08); 4^{th} international symposium on magnetic industry (ISMI'08). Shenyang. Liaoning. China. 2008, P. 17

[8] Munkhtsetseg S, Tsogbadrakh N, Shilagardi G, Poklonski N.A, Lapchuk N.L. Mongolian Nuurstkhotgor coal and its characteristic at low temperature baking: EPR and FTIR study, The 3^{rd} Korea–Mongolia "Energy Technology Symposium", July 1^{st} – July 2^{nd}, Ulaanbaatar, Mongolia. 2008, P. 81

[9] R. Erdenechimeg, L.N. Novikova, B. Purevsuren, T.I. Vakul'skaya, Zh. G. Bazarova Quality Assessment of brown coals from the Ulaan–Ovoo deposit in Mongolia using spectroscopic technique, Solid Fuel Chemistry. 2009, 43, P. 67–70

[10] Dugarjav J. Review on coal research work of Mongolian coals, Chem.Sci. 2006, 81, P. 179

[11] S. Munkhtsetseg, A.V. Khomich, N.A. Poklonski, J. Davaasambuu. Infra-red absorption spectra of the bituminous coals. Journal of Applied Spectroscopy. 2007, 74(3), P. 304–309.

[12] S. Munkhtsetseg, N.A. Poklonski, A.V. Khomich, N.I. Gorbachuk, N.M. Lapchuk. Analysis of electron paramagnetic resonance line shape of bituminous coals. Vestnik. Journal of Belarusian State University. 2007, 1(3), P. 49–55.

[13] S. Munkhtsetseg, B. Munkh–Orchlon. Coal structure in the oxidation. NUM, Scientific Writing, Journal of Physics. National University of Mongolia, 2011, 355(16), P. 60–63.

[14] N. A. Poklonski, S. A. Vyrko, O. N. Poklonskaya, N.M. Lapchuk, S. Munkhtsetseg. Inversion of electron spin resonance signal in coals. Journal of Applied Spectroscopy. 2013, 80(3), P. 380–384.

[15] S. Munkhtsetseg, N. M. Lapchuk, N. A. Poklonski, N. I. Gorbachuk, Kh. Tsookhuu, G. Shilagardi, N. Tsogbadrakh, T. M. Lapchuk. Advanced pulse EPR study of natural Mongolian coals. 6^{th} International Conference "Materials and Structures of Modern

Electronics", October 8 – 9, Minsk (Belarus). 2014, P. 11–15.

[16] S. Munkhtsetseg, N. M. Lapchuk, N. A. Poklonski, N. I. Gorbachuk, Kh. Tsookhuu, G. Shilagardi, N. Tsogbadrakh, A. N. Oleshkevich. CW EPR study of natural Mongolian coals. 6^{th} International Conference "Materials and Structures of Modern Electronics" October 8 – 9, Minsk (Belarus). 2014, P. 15–19.

[17] Stefan Stoll, Arthur Schweiger. EasySpin: Simulating cw ESR spectra Biol. Magn. Reson. 2007, 27, P. 299–321

[18] Hiroyuki Seki, Osamu Ito, Masashi Iino. Energy&Fuels. 1988, 2, P. 321–325

[19] Mohindar S. Seera, Bikas Ghosh. Journal of Analytical and Applied Pyrolysis. 1988, 13, P. 209–220

Finite Quantum Electrodynamics

Kh.Namsrai, B.Munkhzaya, M.Purevkhuu

Department of Theoretical Physics, Institute of Physics and Technology, Mongolian Academy of Sciences, Peace Ave. 54b, Ulaanbaatar 13330, Mongolia

It is known that the origin of the divergence problem in quantum electrodynamics is related to the singularity of classical electrostatic potential. A modification of its Coulomb potential at small distances leads to the change of the photon propagator which allows us to construct finite and gauge-invariant quantum electrodynamics. We establish restriction on the value of the so-called fundamental length $\ell \leq 10^{-16}$cm from the experimental data on the measuring anomalous magnetic moment of leptons. It is well known that any modification of the spinor propagator (in particular, electron one) gives ride to many problems connected with verification of basic principles of the theory like gauge invariance, unitarity, causality condition and so on. However, it turns out that square-root modification of the spinor propagator is free from these difficult problems. Here we also construct a finite square-root quantum electrodynamics.

I. INTRODUCTION

A beautiful quantum electrodynamics developed by many physicists of the 20^{th} Century (for example, see [1-5]) has played a vital role in the construction of the finite and gauge invariant so - called standard model [6,7] of the particle physics. What was an initial origin of this theory. It is natural that it was classical electrostatic field theory. Generally speaking, as usual, classical and quantum theories are the models of **point - like particles**. For example, the Newtonian and Coulomb potentials

$$U_N(r) = \frac{G}{4\pi r}, \qquad U_C(r) = \frac{e}{4\pi r} \tag{1}$$

are the potentials of the point - like sources of mass and charge, respectively:

$$\rho_N(\mathbf{r}) = m\delta(\mathbf{r}), \qquad \rho_C(\mathbf{r}) = e\delta(\mathbf{r})$$

where $\delta(\mathbf{r}) = \delta(x)\delta(y)\delta(z)$ is the Dirac δ - function with properties:

$$\int_{-\infty}^{\infty} dx\delta(x) = 1, \qquad \int_{-\infty}^{\infty} dx\delta(x)f(x) = f(0)$$

and etc.

It is well known that the inverse Fourier transform of the Coulomb potential for point - like charge is

$$D(\mathbf{p}) = \frac{1}{e}\int d^3 r e^{i\mathbf{pr}} U_C(r) = \frac{1}{\mathbf{p}^2} \tag{2}$$

and its relativistic generalization in four - momentum space

$$D(p) = \frac{1}{-p_0^2 + \mathbf{p}^2 - i\varepsilon} \tag{3}$$

gives the local photon propagator which leads to the divergent theory. Fundamental importance is that the Coulomb potential (1) satisfies the Laplace equation

$$\Delta U_C(r) = 0 \tag{4}$$

where

$$\Delta = \frac{\partial^2}{\partial x^2} + \frac{\partial^2}{\partial y^2} + \frac{\partial^2}{\partial z^2}.$$

In principle, any modification of the Coulomb potential at small distances leads to a violation of the Laplace equation (4). Here we find out more simpler and natural changing of the Coulomb potential

$$U_C(r) \Rightarrow U_C^l(r) = \frac{e}{4\pi}\frac{1}{\sqrt{r^2 + l^2}} \tag{5}$$

which does not satisfy the Laplace equation (4) and gives modification of the photon propagator (3):

$$D(p) \Rightarrow D^l(p) = \frac{1}{-p^2 - i\varepsilon} V_l(-p^2 l^2) \tag{6}$$

where

$$V_l(-p^2l^2) = \frac{1}{2i}\int_{-\beta+i\infty}^{-\beta-i\infty} d\eta \frac{v(\eta)}{\sin\pi\eta}\left[l^2\left(-p^2-i\varepsilon\right)\right]^{1+\eta} \tag{7}$$

$(1 < \beta < 2)$

$$v(\eta) = \frac{\pi}{4^{1+\eta}}\frac{1}{\sin\pi\eta\cdot\Gamma(1+\eta)\Gamma(2+\eta)}. \tag{8}$$

Some time ago Markov [8] considered possibility of changing metric form

$$S_0 = x^2+y^2+z^2 \to x^2+y^2+z^2 \pm l^2$$

in his indefinite metric modification of the field theory.

The Poisson equation for the potential (5) takes the form

$$\Delta U = -\frac{3l^2}{(r^2+l^2)^{5/2}}.$$

On the other hand the basic equation for electric stress $\mathbf{E} = -\text{grad}\phi$ with extended charges is

$$\text{div}\mathbf{E} = 4\pi\rho = -\text{div grad}\phi = -\Delta\phi,$$

$$\Delta\phi = -4\pi\rho.$$

It means that in our case electric charge is not located at the single point and is distributed continuously over the whole space with the density

$$\rho = \frac{1}{4\pi}\frac{3l^2}{(r^2+l^2)^{5/2}}$$

with the normalization

$$\int d^3r\rho(r) = 1$$

as it should.

Therefore, in our scheme, an idealized concept of the point - like charge is absent.

Moreover, already in the early developments of quantum mechanics occur square - root operators. In particular, it was the relativistic relation between energy and momentum in a coordinate space representation that hindered its use [9]. A review of the early and later works are contained in [10]. In bound - state problems of two - and three - quark systems the Salpeter equation is often used [11-13]. Problems associated with binding in very strong fields [14,15] string theory [16,17] and astrophysical black holes [18-20] are applicable areas. Green's function for differential equations of infinite order like

$$\sqrt{m^2 - \Box}\Omega(x) = -\delta^{(4)}(x) \tag{9}$$

are treated in [21]. Green function (9) in momenum p - and x - spaces take the forms

$$\Omega(p) = -\frac{1}{\sqrt{m^2 - p^2 - i\varepsilon}} = \int_{-m}^{m} d\lambda \rho_m(\lambda) \widetilde{S}(\lambda, \widehat{p}) \tag{10}$$

and

$$\Omega(x - y) = \int_{-m}^{m} d\lambda \rho_m(\lambda) S(x - y, \lambda) \tag{11}$$

where the distribution

$$\rho_m(\lambda) = \frac{1}{\pi} \left(m^2 - \lambda^2\right)^{-1/2}$$

has the following properties,

$$\int_{-m}^{m} d\lambda \rho_m(\lambda) = 1, \qquad \int_{-m}^{m} d\lambda \cdot \lambda \cdot \rho_m(\lambda) = 0$$

$$\int_{-m}^{m} d\lambda \lambda^2 \rho_m(\lambda) = \frac{1}{2} m^2 \tag{12}$$

and

$$\widetilde{S}(\lambda, \widehat{p}) = \frac{1}{i} \frac{\lambda + \widehat{p}}{\lambda^2 - p^2 - i\varepsilon} \tag{13}$$

$$S(x-y,\lambda)=\frac{1}{(2\pi)^4}\frac{1}{i}\int d^4p e^{-ip(x-y)}\frac{\lambda+\widehat{p}}{\lambda^2-p^2-i\varepsilon} \tag{14}$$

are the Dirac spinor propagator in corresponding spaces with random mass λ. Here the relations

$$m^2-p^2=(m-\hat{p})(m+\widehat{p}),\qquad \widehat{p}=\gamma^\nu p_\nu$$

and the Feynman parametric formula

$$\frac{1}{a^{n_1}b^{n_2}}=\frac{\Gamma(n_1+n_2)}{\Gamma(n_1)\Gamma(n_2)}\int_0^1 dx x^{n_1-1}(1-x)^{n_2-1}\frac{1}{[ax+b(1-x)]^{n_1+n_2}} \tag{15}$$

are used. In this paper by using formulas (6), (10), (11), (13) and (14) we will construct finite nonlocal and square - root quantum electrodynamics free from ultraviolet divergences.

II. MODIFICATION OF THE COULOMB POTENTIAL AND DERIVATION OF THE NONLOCAL PHOTON PROPAGATOR

We propose the following finite Coulomb potential at small distances:

$$U_C^l(r)=\frac{e}{4\pi}\frac{1}{\sqrt{x^2+y^2+z^2+l^2}} \tag{16}$$

where l - is some parameter dimension of length. Its value may be interpreted as a size of an extended electric charge or as an universal constant like fundamental length in physics. As mentioned above this modified potential satisfies the Poisson equation. Let us calculate the Fourier transform of the finite potential (16):

$$D_l(\mathbf{p})=\frac{1}{e}\int d^3r e^{i\mathbf{pr}}\left(\frac{e}{4\pi\sqrt{r^2+l^2}}\right)=\frac{1}{p}\int_0^\infty dr\frac{r}{\sqrt{r^2+l^2}}\sin pr,$$

($p=|\mathbf{p}|$). By using the Mellin representation this expression takes the form

$$D_l(\mathbf{p})=\frac{l^2}{2\sqrt{\pi}}\cdot\frac{l}{2i}\int_{-\beta+i\infty}^{-\beta-i\infty}d\eta\frac{(p^2l^2)^\eta}{\sin\pi\eta\Gamma(2+2\eta)}\times\Gamma\left(\frac{3}{2}+\eta\right)\Gamma(-1-\eta) \tag{17}$$

where $(1<\beta<2)$.

Further, taking into account Gamma - function relations:

$$\Gamma(2+2\eta)=\frac{2^{2(1+\eta)-1}}{\sqrt{\pi}}\Gamma(1+\eta)\Gamma\left(\frac{3}{2}+\eta\right)$$

$$\Gamma(\eta)\Gamma(1-\eta)=\frac{\pi}{\sin\pi\eta}$$

and after some elementary calculations, one gets

$$D_l(\mathbf{p})=\frac{V_l\left(\mathbf{p}^2l^2\right)}{\mathbf{p}^2} \tag{18}$$

where

$$V_l(\mathbf{p}^2l^2)=\frac{1}{2i}\int_{-\beta+i\infty}^{-\beta-i\infty}d\eta\frac{v(\eta)}{\sin\pi\eta}\left[l^2\mathbf{p}^2\right]^{1+\eta} \tag{19}$$

$$v(\eta)=\frac{\pi}{4^{1+\eta}}\frac{1}{\sin\pi\eta}\frac{1}{\Gamma(1+\eta)\Gamma(2+\eta)}. \tag{20}$$

From these formulas one can calculate residues at the points $\eta=-1,0,1,\ldots$. The result reads

$$D_l(\mathbf{p})=\frac{l}{|\mathbf{p}|}K_1(l|p|) \tag{21}$$

where $K_1(x)$ is the modified Bessel function of second kind or the Mac'Donald function

$$K_1(x)=\frac{\pi}{2}\frac{x}{2}\frac{1}{2i}\int_{-\beta+i\infty}^{-\beta-i\infty}d\zeta\frac{\left(\frac{x}{2}\right)^{2\zeta}}{\sin^2\pi\zeta\Gamma(1+\zeta)\Gamma(2+\zeta)}$$

$(0<\beta<1)$, $x=|p|l$.

Finally, the modification of the Coulomb potential (16) gives rise to the following nonlocal photon propagator [22]

$$D^l_{\mu\nu}(x)=\frac{i}{(2\pi)^4}g_{\mu\nu}\int d^4pe^{ipx}\frac{V_l\left(-p^2l^2\right)}{-p^2-i\varepsilon} \tag{22}$$

where the form - factor $V_l\left(-p^2l^2\right)$ of the theory is defined by the formulas (19) and

(20).

Here our theory with the propagator (22) is very similar to the nonlocal theory due to [22] and [23]. Notice that the simple modification of the Coulomb potential (16) leading to the nonlocal photon propagator (22) is cornerstone of the finiteness of classical and quantum electromagnetic fields. For example, now electrostatic self - energy of the extended charge is finite at small distances:

$$W = \frac{e}{2}\int d^3r\rho(r)U_l(r) = \frac{1}{2}\int d^3rE^2, \quad E = -\frac{e}{4\pi}\mathrm{grad}\frac{1}{\sqrt{r^2+l^2}}.$$

Here simple calculation reads

$$W = \frac{e^2}{8\pi}\int_0^\infty dr\frac{r^4}{[r^2+l^2]^3} = \frac{e^2}{2\Gamma(3)}\frac{1}{l}\Gamma\left(\frac{5}{2}\right)\Gamma\left(\frac{1}{2}\right)\cdot\frac{1}{8\pi} = \frac{3}{32}\frac{\pi}{l}\alpha.$$

Moreover, the nonlocal photon propagator (22) is finite at the origin

$$\begin{aligned} D^l_{\mu\nu}(0) &= g_{\mu\nu}\frac{2\pi^2}{2^4\pi^4}\int_0^\infty dpp^3D_l(p^2) = \\ &= -g_{\mu\nu}\frac{1}{8\pi}\lim_{\epsilon\to 0}\int_{-\beta+i\infty}^{-\beta-i\infty}d\zeta\frac{\left(\frac{l^2}{4}\right)^{1+\zeta}}{\sin^2\pi\zeta}\frac{\varepsilon^{2\zeta+4}}{\Gamma(1+\zeta)\Gamma(2+\zeta)\Gamma(2\zeta+4)} \end{aligned}$$

where $2<\beta<3$.

Calculation of residue at the point $\zeta=-2$ and taking the limit $\varepsilon\to 0$ leads

$$D^l_{\mu\nu}(0) = \frac{1}{4\pi^2l^2}g_{\mu\nu} = const.$$

It turns out that, in principle, due to finiteness of $D^l_{\mu\nu}(0)$ one can calculate vacuum fluctuation diagrams, shown in Figure 1.

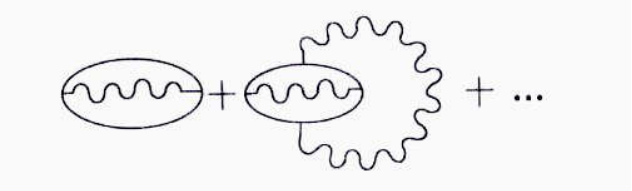

FIG. 1: Primative Feynman diagrams for vacuum fluctuation

Finally, we indicate one important consequence of the photon propagator (22) with the form - factor (19). If we want to calculate high order divergence integrals over

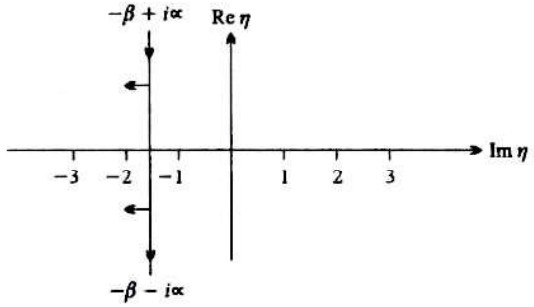

FIG. 2: Integration contour in the formula (19)

the internal momentum variable p, like

$$\frac{1}{2i}\int_{-\beta+i\infty}^{-\beta-i\infty} d\eta \frac{v(\eta)}{\sin\pi\eta}\int d^4p \frac{[p^{2\nu}]^\eta}{[p^2+A]^\lambda}$$

for any order of ν, then we can move integration contour in Figure 2 to the left through points $\eta = -2, -3, \ldots$, in desired order, since in such type of integrals there are no poles at these points. After integration result we can again move integration contour to the right to calculate residues at the points $\eta = -3, -2, -1, \ldots$ so on. This procedure of analytic continuation over complex variable η plays a vital role in regularization scheme.

III. NONLOCAL QUANTUM ELECTRODYNAMICS

A. Introduction

Lagrangian functions of the nonlocal quantum electrodynamics arisen from the modification of the Coulomb potential at small distances have similar structures as the local theory [24].

$$\begin{aligned} L(x) &= e : \overline{\psi}(x)\widehat{A}(l,x)\psi(x) : \\ &+ e(Z_1-1) : \overline{\psi}(x)\widehat{A}(l,x)\psi(x) : \\ &- \delta m : \overline{\psi}(x)\psi(x) : + (Z_2-1) : \overline{\psi}(x)(i\widehat{\partial} - m)\psi(x) : \\ &- (Z_3-1)\frac{1}{4} : F_{\mu\nu}(x)F^{\mu\nu}(x) : \end{aligned} \tag{23}$$

where

$$\widehat{A}(l,x) = A_\mu(l,x)\gamma^\mu, \quad \widehat{\partial} = \gamma^\mu \frac{\partial}{\partial x_\mu}.$$

Only in our case of the nonlocal theory, renormalization constants $Z_1, Z_2, Z_3, \delta m$ are finite and moreover $Z_1 = Z_2$ due to the Ward - Takahashi identity. Here "chronological" pairing (or T - product) of the fermonic field operators of electrons has the usual local form:

$$S(x-y) = \langle 0|T[\psi(x)\overline{\psi}(y)]|0\rangle = \frac{1}{(2\pi)^4}\frac{1}{i}\int d^4p \frac{e^{-ip(x-y)}}{m-\widehat{p}-i\varepsilon} \tag{24}$$

while "causal" function of the nonlocal electromagnetic field $A_\mu(l,x)$ in (23) takes the form due to the formula (22)

$$D^l_{\mu\nu}(x-y) = g_{\mu\nu}D^l(x-y) = -\frac{g_{\mu\nu}}{(2\pi)^4 i}\int d^4p e^{-ip(x-y)}\frac{V_l(-p^2l^2)}{-p^2-i\varepsilon} \tag{25}$$

where $V_l(-p^2l^2)$ is given by formulas (19) and (20).

B. The Electron Self - Energy in NQED

The complete electron propagator in NQED is given by the sum

$$\begin{aligned}\left[-i(2\pi)^{-4}S'_l(p)\right] &= \left[-i(2\pi)^{-4}S(p)\right] + \left[i(2\pi)^{-4}S(p)\right]\left[i(2\pi)^4\Sigma_l(p)\right] \\ &\times \left[-i(2\pi)^{-4}S(p)\right] + \cdots\end{aligned}$$

where

$$S(p) = \frac{m+\widehat{p}}{m^2-p^2-i\varepsilon}.$$

The sum is trivial and gives

$$S'_l(p) = \left[m-\widehat{p}-\Sigma_l - i\varepsilon\right]^{-1}.$$

In the lowest order there is a one - loop contribution to Σ_l, given by in Figure 3:

$$-i : \overline{\psi}(x)\Sigma_l(x-y)\psi(y) :$$

where

$$\Sigma_l(x-y) = -ie^2\gamma_\mu S(x-y)\gamma_\mu D^l(x-y). \tag{26}$$

Passing to the momentum representation and going to the Euclidean metric by using $k_0 \to \exp(i\pi/2)k_4$, one gets

$$\widetilde{\Sigma}_l(p) = \frac{e^2}{(2\pi)^4}\int d^4k_E \frac{V_l(k_E^2 l^2)}{k_E^2}\gamma_\mu^{(E)}\frac{m - \widehat{p}_E + \widehat{k}_E}{m^2 + (p_E - k_E)^2}\gamma\mu^{(E)}.$$

Here $p_E = (-ip_0, \mathbf{p})$, $\gamma^{(E)} = (-i\gamma_0, \overrightarrow{\gamma})$ and $k_E = (k_4, \mathbf{k})$. Taking into account the Mellin representation (19) for the form - factor $V_l(k_E^2 l^2)$ and after some calculations, we have

$$\widetilde{\Sigma}_l(p) = -\frac{e^2}{8\pi}\frac{1}{2i}\int_{-\beta+i\infty}^{-\beta-i\infty} d\eta \frac{1}{\sin^2\pi\eta}\frac{v(\eta)(m^2e^2)^{1+\eta}}{\Gamma(2+\eta)}F(\eta,p) \tag{27}$$

where

$$F(\eta,p) = \frac{1}{\Gamma(-\eta)}\int_0^1 du\left(\frac{1-u}{u}\right)^{1+\eta}\left(1 - \frac{p^2}{m^2}u\right)^{1+\eta}(2m - \widehat{p}u) \tag{28}$$

is a regular function in the half - plane $\mathrm{Re}\eta > -2$.

Assuming the value m^2l^2 to be small, one can obtain (after calculation of residues at the points $\eta = -1, 0$):

$$\begin{aligned}
\widetilde{\Sigma}_l(p) &= \frac{e^2}{8\pi^2}\int_0^1 du(2m - \widehat{p}u)\ln\left(1 - \frac{p^2}{m^2}u\right) + \\
&+ \frac{e^2}{8\pi^2}\left\{\ln\left(\frac{m^2l^2}{4}\right)\left(2m - \frac{1}{2}\widehat{p}\right) + \widehat{p}\left(\frac{1}{2} + \psi(1)\right) - 4m\psi(1)\right\} + \\
&+ \frac{me^2}{32\pi^2}(m^2l^2)\left[\ln^2\left(\frac{m^2l^2}{4}\right) - \ln\left(\frac{m^2l^2}{4}\right)(3 + 4\psi(1)) + \right. \\
&+ \left. 4\psi(1)(1+\psi(1)) + 2 - \frac{1}{3}\pi^2\right],
\end{aligned} \tag{29}$$

where $\psi(1) = -C, C = 0.57721566490\ldots$ is the Euler number.

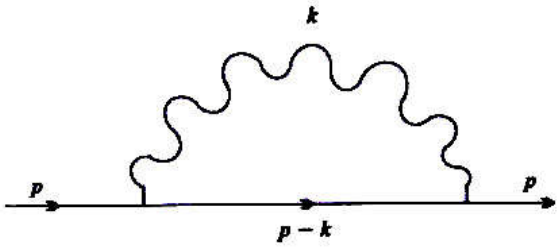

FIG. 3: Diagram of Self - energy of a electron in NQED

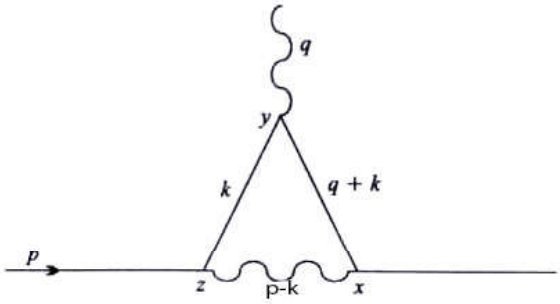

FIG. 4: Vertex function in NQED

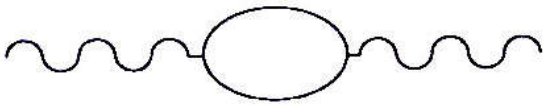

FIG. 5: The vacuum polarization in NQED

C. Vertex Function and Anomalous Magnetic Moment of Leptons in NQED

Let us consider Feynman diagram shown in Figure 4. The following matrix element corresponds to this diagram:

$$\mathrm{ie} : \overline{\psi}(x)\Gamma^{l}_{\mu}(x, z/y)\psi(z)A_{\mu}(y) : \tag{30}$$

Analogously, in the momentum space and in the Euclidean metric, the vertex function takes the form

$$\begin{aligned}\widetilde{\Gamma}^{l}_{\mu}(p_1, p) &= -\frac{e^2}{(2\pi)^4}\int d^4k_E \frac{V_l\left((p_E - k_E)^2 l^2\right)}{(p_E - k_E)^2}\gamma_\nu \times \\ &\times \frac{m - \widehat{k}_E - \widehat{q}_E}{m^2 + (k_E + p_E)^2}\gamma_\mu \frac{m - \widehat{k}_E}{m^2 + k_E^2}\gamma_\nu \end{aligned} \tag{31}$$

Again passing to the Minkowski metric and using the generalized Feynman parameterization formula (15), one gets

$$\widetilde{\Gamma}^{l}_{\mu}(p_1;p) = \frac{e^2}{8\pi}\frac{1}{2i}\int_{-\beta+i\infty}^{-\beta-i\infty} d\eta \frac{v(n)}{\sin^2\pi\eta}\frac{(m^2l^2)^{1+\eta}}{\Gamma(2+\eta)}F\mu(\eta;p_1,p) \tag{32}$$

where

$$F_{\mu}(\eta;p_1,p) = \gamma_{\mu}F_1(\eta;p_1,p) + F_2(\eta;p_1,p)$$

Here

$$F_1(\eta;p_1,p) = \frac{1}{\Gamma(-\eta)}\int_0^1\int_0^1\int_0^1 d\alpha d\beta d\gamma\delta(1-\alpha-\beta-\gamma)\alpha^{-1-\eta}Q^{1+\eta}$$

$$\begin{aligned} F_2(\eta;p_1,p) &= \frac{1}{\Gamma(-1-\eta)}\int_0^1\int_0^1\int_0^1 d\alpha d\beta d\gamma\delta(1-\alpha-\beta-\gamma)\alpha^{-1-\eta}Q^{\eta}\times \\ &\times \frac{1}{m^2}\left[m^2\gamma_{\mu} - 2mq_{\mu} + 4m(\beta q_{\mu} - \alpha p_{\mu}) + \right. \\ &+ \left. (\alpha\widehat{p} - \beta\widehat{q})\gamma_{\mu}\widehat{q} + (\alpha\widehat{p} - \beta\widehat{q})\gamma\mu(\alpha\widehat{p} - \beta\widehat{q})\right] \end{aligned} \tag{33}$$

$$Q = \beta + \gamma - \alpha\gamma\frac{p^2}{m^2} - \beta\gamma\frac{q^2}{m^2} - \alpha\beta\frac{(p+q)^2}{m^2}. \tag{34}$$

Let us calculate the vertex function (32) for two cases: first, when $q = 0$ and p has an arbitrary value; second, when q is an arbitrary quantity and p, p_1 are situated on the m - mass shell. In the first case, assuming $q = 0$ in the formula (33) and after some standard calculations, one gets

$$\begin{aligned} F_{\mu}(\eta;p_1,p) &= \frac{1}{\Gamma(-\eta)}\int_0^1 du\left(\frac{1-u}{u}\right)^{1+\eta}\left(1-u\frac{p^2}{m^2}\right)^{1+\eta}\times \\ &\times \left[u\gamma_{\mu} + \frac{2(1+\eta)up_{\mu}(2m-u\widehat{p})}{m^2-up^2}\right]. \end{aligned} \tag{35}$$

Comparing this formula with the expression (28) for the self - energy of the electron, it is easily seen that

$$F_{\mu}(\eta;p_1,p) = -\frac{\partial}{\partial p_{\mu}}F(\eta;p). \tag{36}$$

From this identity, we can obtain a very important conclusion. In nonlocal QED constructed using the modification of the Coulomb potential, the Ward - Takahashi identity is valid:

$$\widetilde{\Gamma}^{l}_{\mu}(p,p) = -\frac{\partial}{\partial p_{\mu}}\widetilde{\Sigma}_{l}(p). \tag{37}$$

In the second case, one can put

$$\overline{u}(\mathbf{p}_1)\widetilde{\Gamma}^{l}_{\mu}(p_1,p)u(\mathbf{p}) = \overline{u}(\mathbf{p}_1)\Lambda_{\mu}(q)u(\mathbf{p}) \tag{38}$$

where $u(\mathbf{p}_1)$ and $u(\mathbf{p})$ are solutions of the Dirac equation

$$(\widehat{p}-m)u(\mathbf{p}) = 0, \quad \overline{u}(\mathbf{p}_1)(\widehat{p}_1+m) = 0.$$

Substituting the vertex function (32) into (38) and after some transformations, we have

$$\overline{u}(\mathbf{p}_1)F_{\mu}(\eta;p_1,p)u(\mathbf{p}) = u(\mathbf{p}_1)\Lambda_{\mu}(\eta;q)u(\mathbf{p}). \tag{39}$$

Here

$$\Lambda_{\mu}(\eta;q) = \gamma_{\mu}f_1(\eta;q^2) + \frac{i}{2m}\sigma_{\mu\nu}q_{\nu}f_2(\eta;q^2)$$

$$\sigma_{\mu\nu} = \frac{1}{2i}(\gamma_{\mu}\gamma_{\nu} - \gamma_{\nu}\gamma_{\mu})$$

$$f_j(\eta;q^2) = \frac{1}{\Gamma(-\eta)}\int_0^1\int_0^1\int_0^1 d\alpha d\beta d\gamma\delta(1-\alpha-\beta-\gamma)\alpha^{-1-\eta}L^{\eta}\times g_j(\alpha,\beta,\gamma,q^2), \quad (j=1,2)$$

$$L = \varepsilon\alpha + (1-\alpha)^2 - \beta\gamma\frac{q^2}{m^2} \tag{40}$$

$$\begin{aligned} g_1(\alpha,\beta,\gamma,q^2) &= (1-\alpha)^2(-\eta)+2\alpha(1+\eta)- \\ &- \frac{q^2}{m^2}\left[\beta\gamma+(1+\eta)(\alpha+\beta)(\alpha+\gamma)\right]\cdot \\ &\cdot\ g_2(\alpha,\beta,\gamma,q^2)=2\alpha(1-\alpha)(1+\eta). \end{aligned}$$

To avoid infrared divergences in the vertex function we have introduced here the parameter $\varepsilon = m_{ph}^2/m^2$, taking into account the "mass" of the photon. Finally, one gets

$$\Lambda_\mu(q) = \gamma_\mu F_1(q^2) + \frac{i}{2m}\sigma_{\mu\nu}q_\nu F_2(q^2) \tag{41}$$

where

$$F_j(q^2) = \frac{e^2}{8\pi}\frac{1}{2i}\int_{-\beta+i\infty}^{-\beta-i\infty} d\eta \frac{v(\eta)}{\sin^2\pi\eta}\frac{(m^2l^2)^{1+\eta}}{\Gamma(2+\eta)} f_j(\eta;q^2). \tag{42}$$

It is easy to verify that the vertex function $\Lambda_\mu(q)$ satisfies the gauge invariant condition:

$$q_\mu \overline{u}(\mathbf{p}_1)\Lambda_\mu(q)u(\mathbf{p}) = 0. \tag{43}$$

Let us write the first terms of the decomposition for the functions $F_1(q^2)$ and $F_2(q^2)$ over small parameters m^2l^2 and q^2/m^2:

$$F_2(q^2) = -\frac{\alpha}{2\pi}\left[1+\frac{m^2l^2}{6}\left(\ln\frac{m^2l^2}{4}-2\psi(1)+\frac{1}{6}\right)\right]+O\left(\frac{q^2}{m^2}\right) \tag{44}$$

$$\begin{aligned} F_1(q^2) &= -\frac{\alpha}{4\pi}\left\{3\left[\ln\frac{m^2l^2}{4}-2\psi(1)-\frac{3}{2}\right]+\right. \\ &+ \left. m^2l^2\left[\ln\frac{m^2l^2}{4}-2\psi(1)-\frac{1}{3}\right]\right\}+O\left(\frac{q^2}{m^2}\right). \end{aligned} \tag{45}$$

We know that corrections to the anomalous magnetic moment (AMM) for leptons are given by

$$(\Delta\mu)_i = (\Delta\mu)_i^{QED} + (\Delta\mu)_i^{EW} + (\Delta\mu)_i^{Hadron} + (\Delta\mu)_i^{nonlocal},$$

$$(i = e, \mu),$$

where for example,

$$(\Delta\mu)_e^{QED} = \frac{\alpha}{2\pi} - 0.328478455\left(\frac{\alpha}{\pi}\right)^2 + C_3\left(\frac{\alpha}{\pi}\right)^3 + C_4\left(\frac{\alpha}{\pi}\right)^4 \tag{46}$$

$$\begin{pmatrix} C_3 = 1,1765 \pm 0,0013 \\ C_4 = -0,8 \pm 2,5 \end{pmatrix}$$

and

$$\Delta\mu_i^{nonlocal} = \frac{\alpha}{2\pi}\left[\frac{m_i^2 l^2}{6}\left(\ln\frac{m_i^2 l^2}{4} + \frac{1}{6} - 2\psi(1)\right)\right]$$

$$(i = e, \mu).$$

We seen that the first term in (46) is exactly famous Schwinger correction obtained in local QED. From the experimental values of the AMM of the electron and muon ([25], [26],[27]) and [28]

$$\Delta\mu_{exp}^{(e)} = \frac{\mu_e}{\mu_B} - 1 = \frac{1}{2}(q-2) = (1159652180.73(0.28)) \times 10^{-12} \tag{47}$$

and

$$\Delta\mu_{exp}^{(\mu)} = \frac{\mu_\mu}{(e\hbar/2m_\mu)} - 1 = \frac{1}{2}(g_\mu - 2) = (116592089(63)) \times 10^{-11} \tag{48}$$

one gets the following restriction on the value of the universal parameter (or the fundamental length) l:

$$l \lesssim 7.0 \times 10^{-17}\text{cm for} \quad \Delta\mu_{\text{exp}}^{(e)} \tag{49}$$

$$l \lesssim 2.6 \times 10^{-17}\text{cm for} \quad \Delta\mu_{exp}^{(\mu)}. \tag{50}$$

Recent theoretical calculations of the AMM of the electron and muon have been

carried by [29].

D. Vacuum Polarization

Since, in our scheme the propagator $S(x-y)$ of the charged lepton spinor is not changed, the diagrams of the vacuum polarization i.e., closed spinor propagators (see Figure 5) of the leptons in our nonlocal QED are studied by the same way as in the local theory. For completeness we calculate it in e^2-order by using d - dimensional regularization procedure [30]. The result reads in the momentum space:

$$\widetilde{\prod}^{\rho\sigma}(q) = (q^2 g^{\rho\sigma} - q^\rho q^\sigma)\widetilde{\prod}(q^2) \tag{51}$$

where

$$\widetilde{\prod}(q^2) = \frac{e^2}{2\pi^2}\int_0^1 dx(1-x)\ln\left(1+\frac{q^2x(1-x)}{m^2}\right). \tag{52}$$

The physical importance of the vacuum polarization in NQED can be explored by considering its effects on the scattering of two charged particles of spin 1/2.

IV. THE SQUARE - ROOT NONLOCAL QUANTUM ELECTRODYNAMICS

The purpose of this section is to study nonlocal interactions of the charged square - root spinors with nonlocal photons within our scheme. Thus, the Lagrangian corresponding to the equation

$$\sqrt{m^2-\Box}\phi(x) = 0 \tag{53}$$

is given by

$$L^0_\phi = \phi^*(x)\sqrt{m^2-\Box}\phi(x). \tag{54}$$

Instead of (54) we consider the Lagrangian density

$$L^0_\psi = -N\left\{\overline{\psi}(x,\lambda_1)(-\widehat{\partial})\psi(x,\lambda_2) + L^0_{1\psi}\right\} \tag{55}$$

for the $\psi(x,\lambda)$ field. Here notation is used

$$L^0_{1\psi} = \Psi(x,\lambda_1)U(\lambda_1,\lambda_2)\Psi(x,\lambda_2)$$

$$N = \int_{-m}^{m}\int_{-m}^{m} d\lambda_1 d\lambda_2 \rho(\lambda_1)\rho(\lambda_2), \quad \widehat{\partial} = i\gamma^\mu \frac{\partial}{\partial x_\mu} \tag{56}$$

$$\overline{\Psi}_(x,\lambda_1) = (0,\overline{\psi}(x,\lambda_1))$$

$$\Psi(x,\lambda_2) = \begin{pmatrix} \psi(x,\lambda_2) \\ 0 \end{pmatrix}$$

$$U(\lambda_1,\lambda_2) = \begin{pmatrix} 0 & \lambda_1 \\ \lambda_2 & 0 \end{pmatrix}.$$

Equations of motion

$$\int_{-m}^{m} d\lambda \rho(\lambda)(\widehat{\partial} - \lambda)\psi(x,\lambda) = 0$$

$$\int_{-m}^{m} d\lambda \rho(\lambda) \left(i\frac{\partial\overline{\psi}(x,\lambda)}{\partial x_\mu}\gamma^\mu + \lambda\overline{\psi}(x,\lambda) \right) = 0 \tag{57}$$

for $\psi(x,\lambda)$ fields can be obtained from the action

$$A = \int d^4x L^0_\psi(x)$$

by using independent variations over the fields $\psi(y,\lambda)$ and $\overline{\psi}(y,\lambda)$ and by taking the differentiation $\delta L^0_{1\psi}/\delta\overline{\psi}(y,\lambda)$ and $\delta(L^0_{1\psi})^T/\delta\psi(y,\lambda)$. Here we have used the following obvious relations

$$\frac{\delta\overline{\psi}(x,\lambda_i)}{\delta\overline{\psi}(y,\lambda)} = \frac{\delta\psi(x,\lambda_i)}{\delta\psi(y,\lambda)} = \delta^{(4)}(x-y)\delta(\lambda_i - \lambda)$$

and definition

$$(L^0_{1\psi})^T = \overline{\Psi}(x,\lambda_1)U^T(\lambda_1,\lambda_2)\Psi(x,\lambda_2).$$

It is easily seen that the propagator of the field $\phi(x)$ in (53) is given by equation (9) or

$$\Omega(x) = -\frac{1}{\sqrt{m^2-\Box}}\delta^{(4)}(x) = \frac{1}{i}\int_{-m}^{m} d\lambda\rho(\lambda)\frac{1}{\lambda+\widehat{\partial}}\delta^{(4)}(x) = \int_{-m}^{m} d\lambda\rho(\lambda)S(x,\lambda). \quad (58)$$

In the momentum representation, expression (58) takes the form

$$\widetilde{\Omega}(p) = \int_{-m}^{m} d\lambda\rho(\lambda)\widetilde{S}(\lambda,\widehat{p}) \quad (59)$$

where

$$\widetilde{S}(\lambda,\widehat{p}) = \frac{1}{i}\frac{\lambda+\widehat{p}}{\lambda^2-p^2-i\varepsilon} \quad (60)$$

is the spinor propagator with random "mass" λ in momentum space.

Our next goal is to study Feynman diagrams in nonlocal square - root quantum electrodynamics with Green functions (22), (58), (59), (60).

In the "square - root" NQED the S - matrix can be constructed by the usual rule:

$$S = ExpecT\exp\left[\int d^4x L_{in}(x)\right] \quad (61)$$

where

$$L_{in}(x) = eN\left\{\overline{\psi}(x,\lambda_1)\widehat{A}_l(x)\psi(x,\lambda_2)\right\} \quad (62)$$

$$\widehat{A}_l = \gamma^\mu A^l_\mu(x)$$

and N is given by (56). The symbol T is defined by

$$\langle 0|T\left[\psi(x,\lambda_1)\overline{\psi}(y,\lambda_2)\right]|0\rangle = \delta(\lambda_1-\lambda_2)S(x-y,\lambda_1)/\rho(\lambda_1) \quad (63)$$

for the spinor fields. For example, at least for connected diagrams in the momentum

space one assumes

$$Expec\left\{\widetilde{\Omega}(p)\right\} = \int_{-m}^{m} d\lambda\rho(\lambda)\widetilde{S}(\widehat{p},\lambda)$$

$$\begin{aligned} & Expec\left\{\gamma^{\nu_1}\widetilde{\Omega}(p_1)\gamma^{\nu_2}\widetilde{\Omega}(p_2)\gamma^{\nu_3}\right\} = \\ = & \int_{-m}^{m} d\lambda\rho(\lambda)\left\{\gamma^{\nu_1}\widetilde{S}(\widehat{p}_1,\lambda)\gamma^{\nu_2}\widetilde{S}(\widehat{p}_2,\lambda)\gamma^{\nu_3}\right\} \end{aligned} \tag{64}$$

and so on.

The gauge invariance of the "square - root" NQED means that every matrix elements of the S - matrix (61) defining the concrete electromagnetic processes have a definite structure, and algebraical relations exist between them. In particular, in the momentum representation, the so - called vacuum polarization diagram like (in Figure 4) in the second order of the perturbation theory has the form

$$\widetilde{\prod}_{\mu\nu}^{l,s}(k) = (k_\mu k_\nu - g_{\mu\nu}k^2)\widetilde{\prod}^{l,s}(k^2) \tag{65}$$

and the relation

$$\frac{\partial\widetilde{\sum}_l^s(p)}{\partial p_\mu} = -\widetilde{\Gamma}_\mu^{l,s}(p,q)|_{q=0} \tag{66}$$

is valid between the vertex function $\widetilde{\Gamma}_\mu^{l,s}(p,q)$ and the self - energy of the "square - root" electron $\widetilde{\Sigma}_l^s(p)$. The relation (66) generalizes the Ward - Takahashi identity in QED. Here in accordance with (64), we have

$$\widetilde{\Sigma}_l^s(p) = \frac{-ie^2}{(2\pi)^4}\int_{-m}^{m} d\lambda\rho(\lambda)\int d^4kD_l(k^2)\gamma^\mu S(\widehat{p}-\widehat{k},\lambda)\gamma^\mu \tag{67}$$

and

$$\begin{aligned} \widetilde{\Gamma}_\mu^{l,s}(p,q) &= \frac{ie^2}{(2\pi)^4}\int d^4kD_l((p-k)^2l^2)\times \\ &\times E_{xpec}\left\{\gamma^\nu\widetilde{\Omega}(q+k)\gamma^\mu\widetilde{\Omega}(k)\gamma^\nu\right\} = \\ &= \frac{ie^2}{(2\pi)^4}\int_{-m}^{m} d\lambda\rho(\lambda)\int d^4kD_l((p-k)^2l^2)\gamma^\nu S(\widehat{q}+\widehat{k},\lambda)\gamma^\mu\times \\ &\times \widetilde{S}(\widehat{k},\lambda)\gamma^\nu \end{aligned} \tag{68}$$

where

$$\widetilde{S}(\widehat{p},\lambda)=\frac{1}{(\lambda-\widehat{p})}$$

and

$$D_l(k^2,l^2)=\frac{V_l(k^2l^2)}{-k^2-i\varepsilon}.$$

Fort the proof of the relation (66) consider the identity

$$\frac{\partial\widetilde{S}(\widehat{p},\lambda)}{\partial p_\mu}=\widetilde{S}(\widehat{p},\lambda)\gamma^\mu\widetilde{S}(\widehat{p},\lambda). \tag{69}$$

Further, it is easy to verify the identity (66) by differentiating (67)over p_μ and making use of the equality (69) as well as choosing other momentum variables in (68) and assuming $q=0, p^{'}=p+q=p$. The relations of the type

$$q_\mu\widetilde{\Gamma}^{l;s}_{\mu}(p,q)|_{p'^2=p^2=\lambda^2}=0$$

follows from the definition

$$\begin{aligned}
&q_\mu E_{xpec.}\left\{\widetilde{\Omega}(p_1)\gamma^\mu\widetilde{\Omega}(p_2)\right\}=q_\mu\int_{-m}^{m}\int_{-m}^{m}d\lambda_1 d\lambda_2\rho(\lambda_1)\rho(\lambda_2)\times\\
&\times\ \widetilde{S}(\widehat{p}_1,\lambda_1)\gamma^\mu\widetilde{S}(\widehat{p}_2,\lambda_2)\frac{\delta(\lambda_1-\lambda_2)}{\rho(\lambda_1)}=\widetilde{\Omega}(p_1)-\widetilde{\Omega}(p_2)=\\
&=\ \int_{-m}^{m}d\lambda\rho(\lambda)\left[\widetilde{S}(\widehat{p}_1,\lambda)-\widetilde{S}(\widehat{p}_2,\lambda)\right]
\end{aligned} \tag{70}$$

if $q=p_1-p_2$.

Now let us demonstrate that the gauge invariance of the vacuum polarization diagram in the "square - root" NQED and its matrix element is given by

$$\begin{aligned}
\widetilde{\prod}^{s}_{\mu\nu}(k)\ &=\ e^2E_{xpec.}\left\{\int d^dpTr\left\{\gamma^\mu\widetilde{\Omega}(p+k)\gamma^\nu\widetilde{\Omega}(p)\right\}=\right.\\
&=\ e^2\int_{-m}^{m}d\lambda\rho(\lambda)\int d^dpTr\left\{\gamma^\mu\widetilde{S}(\widehat{p}+\widehat{k},\lambda)\gamma^\nu\widetilde{S}(\widehat{p},\lambda)\right\}.
\end{aligned} \tag{71}$$

Here we have used the d-dimensional gauge invariant regularization procedure due to [31] and the definition (64). After some calculations we obtain the same structure as

in (65):

$$\prod\nolimits^{s}_{\mu\nu}(k) = \frac{8i\pi^{d/2}}{\Gamma(2)}\Gamma\left(2-\frac{1}{2}d\right)(k_\mu k_\nu - k^2 g_{\mu\nu}) \times \\ \times \int_{-m}^{m} d\lambda\rho(\lambda)\int_0^1 dx x(1-x)\left[\lambda^2 - k^2 x(1-x)\right]^{\frac{d}{2}-2} \quad (72)$$

which is manifestly gauge invariant. Calculation of the matrix elements for $\widetilde{\Sigma}^s_l(p)$ and $\widetilde{\Gamma}^{l,s}_\mu(p,q)$ can be carried out by the same method as in (27) and (32) where we have to change $m \to \lambda$.

In conclusion, we notice that similar modification of the Newtonian potential (1) and (5) gives rise to a finite quantum gravitational theory with the causal Green function for the graviton:

$$G^c_{\mu\nu,\rho\sigma}(x) = \frac{-1}{(2\pi)^4 i}\int d^4 p e^{-ipx}\widetilde{\prod}_{\mu\nu,\rho\sigma}(p) \times \frac{V_l(-p^2 l^2)}{-p^2 - i\varepsilon}$$

where the projecting tensor $\widetilde{\prod}_{\mu\nu,\rho\sigma}(p)$ is given by the expression:

$$\widetilde{\prod}_{\mu\nu,\rho\sigma}(p) = d_{\mu\rho}(p)d_{\nu\sigma}(p) + d_{\mu\sigma}(p)d_{\nu\rho}(p) - \frac{2}{3}d_{\mu\nu}(p)d_{\rho\sigma}(p),$$

$$d_{\mu\nu}(p) = g_{\mu\nu} - p_\mu p_\nu / p^2$$

and $V_l(-p^2 l^2)$ is defined by the same formula (7). Here l should be changed by the Planck length:

$$l \to l_{Pl} = \sqrt{\frac{\hbar G_N}{c^3}} = 1.62 \times 10^{-33}\text{cm}$$

where G_N is the Newtonian constant.

V. ACKNOWLEDGEMENT

We thank the Mongolian Science and Technology foundation for its financial support within the theme "Study of the elementary length and Quantum field theory within interaction of the four forces with agreement SSA-009/14".

VI. REFERENCE

[1] Feynman, R. (1949). Phys.Rev. **79**,749,769.

[2] Tomonaga, S. (1946). Progr.Theor.Phys. **1**, 27.

[3] Schwinger, J. (1959). Phys.Rev.Lett. **3**, 296.

[4] Schwinger, J. (1948). Phys.Rev. **74**, 1439.

[5] Dyson, F.(1949). Phys. Rev. **75**, 486

[6] Weinberg, S. (1967). Phys.Rev.Lett. **19**, 1264.

[7] Salam, A. (1969). in Elementary Particle Theory ed. N.Svartholm, Almquist and Wiksell, Stockholm, p.367.

[8] Markov, M.A. (1959). Nuclear Phys. **10**, 140.

[9] Weyl,H. (1927). Zeitschrift fur Physik, **46**, 38.

[10] Smith, J.R. (1993). Second quantization of the square - root Klein - Gordon Operator, Microscopic causality, Propagators and Interaction, Univ. California, Davis, CA, Preprint UCD/11, RPA-93-13.

[11] Castorina, P. et.al. (1984). Phys. Rev., **D29**, 2660.

[12] Friar, J.L., and Tomusiak, E.L.(1984). Phys.Rev.**C29**, 1537.

[13] Nickisch, L.J. et.al., (1984). Phys.Rev., **D30**, 660.

[14] Hardekopf, G. and Sucher, J.(1985). Phys.Rev.,**A31**, 2020.

[15] Papp, E.(1985). Quasiclassical upper bounds on the nuclear charge, Munich - Print, Munich.

[16] Kaku, M. (1988). Introduction to superstrings, Springer, New York, pp. 48-58.

[17] Fiziev, P.P.(1985). Theoret. and Math. Phys. (Russian), **62**,123.

[18] Berezin, V.(1997a). Nucl.Phys.B(Proceed.Suppl.)**57**,181.

[19] Berezin,V. (1997b). Phys.Rev.**D55**,2139.

[20] Berezin, V.et.al.(1998). Phys.Rev.**D57**,1108.

[21] Namsrai, Kh. (1998). Inter.J.Theoret. Phys., **37**, 1531.

[22] Efimov, G.V. (1977). Nonlocal interactions of quantized fields, Nauka, Moskow.

[23] Namsrai, Kh. (1986). Nonlocal quantum field theory and stochastic quantum mechanics, D.Reidel, Dordrecht, Holland.

[24] Bogolubov,N.N., and Shirkov, D.V.(1980). Introduction to the theory of quantized fields, 3rd ed. Wiley - Intersience, New York.

[25] Hanneke,D. et.al. (2008). Phys.Rev.Lett.**100**, 120801.

[26] Hanneke, D.et.al.(2011). Phys. Rev.**A83**, 052122

[27] Bennett, G.W. et.al. (2004). Phys.Rev.Lett.**92**,161802.

[28] Roberts, B.L. (2010). Chinese Phys. **C34**, 741.

[29] Aoyama,T. et.al. (2012). Phys.Rev.Lett., **109**, 111808; Phys. Rev. **D85**, 033007.

[30] Weinberg, S. (1995). The quantum theory of fields, vol.1: Foundations, Cambridge Univ. Press, Cambridge.

[31] ′t Hooft, G. and Veltman, M.(1972). Nucl.Phys. **B44**, 189.

Cosmic Microwave Background Anisotropy Analysis

M. Otgonbaatar, J. Davaasambuu, and G. Munkhbayar
Department of Physics, School of Arts & Sciences, National University of Mongolia, University Street-1, 210646 Ulaanbaatar, Mongolia

P. Schupp
Department of Physics and Earth Sciences, Jacobs University Campus Ring 1, 28759 Bremen, Germany

In this paper, we study the statistical anisotropy of the cosmic microwave (CMB) radiation in an approach that uses pseudo entropies of quantum-l states and respects rotational symmetry. We simulate large numbers of randomly generated Gaussian CMB data sets and build probability distribution functions (PDFs). We then compare the predicted artificial data with the real measured data. We use WMAP 9 years coadded data as well as newly released high resolution Planck satellite data. Furthermore, we introduced a new efficient method of eliminating the foreground contamination of the CMB by means of a decomposition procedure of products of spherical harmonics, which is equivalent to applying a mask on the sky map up to a given accuracy.

OUTLINE

First of all, brief comprehension of what CMB is, what it corresponds, how we measured it, is provided. Furthermore characteristics and data products of satellite missions dedicated to measure the CMB are introduced.

Followed with this introduction, software packages which is main tool for cosmological data are discussed, and their applications in our work are explained in details.

In the third section, we introduced two methods which are qualitatively new ways to evaluate randomness of collected data by means of comparing real data with artificially generated one which follows specific statistical distribution.

In next section, computational results are graphically expressed and some anomalies are observed and discussed. Then the summary of the work continues in the last section.

I. INTRODUCTION

Main motivation of this work arises after findings of Schupp and others' work [17] which observes extreme anisotropy of CMB maps with galactic foreground at lower multipoles calculated by methods which will be introduced latter. These anomalies concluded to be result of galactic foreground contamination. This leads to further interests of calculation of higher multipoles of foreground reduced maps.

The Cosmic Microwave Background radiation (CMB) is the electromagnetic radiation coming from every direction of the universe, which was discovered in 1964 experimentally and led two American radio astronomers, Arno Penzias and Robert Wilson, to win the Nobel prize in 1978. The term - "microwave" derives from its wavelength range that is few centimetres.

Its intensity is almost uniform all over the sky, except for tiny wrinkles. Regardless of the exceptional wrinkles in the intensity, CMB has the spectrum of black body radiation[28] at temperature of $T_{CMB} = 2.72548 \pm 0.00057K$[10] which was experimentally well confirmed by the FIRAS instrument[11, 20, 30] on the COBE satellite.

The tiny wrinkles, i.e. small variations of the temperature from the theoretical value of the black-body radiation, are of great interest to scientists. Many questions arises from its anisotropy. The current data has been used to test the inflationary model[15] of the universe which is suggested to have happened after the big bang. According to the Big Bang theory, the tiny variation is the remnant of a statistical density variation of the matter after the Big Bang, which evolves in time and now seen as it's in the CMB temperature variation.

$$\Delta T(\theta, \phi) = T(\theta, \phi) - T_{CMB}$$

This small variation is order of a few μK (indeed $\sim 10^{-5}K$).

One of the difficulty, which is the inseparable part of the CMB data, is the foreground contamination of the radio wave, since there are many other natural sources of the electromagnetic rays, that are of the same wavelength range of the CMB as well as have strong enough intensity to ruin the pure cosmological rays. Therefore one mainstream among the reseachers of the CMB is to remove or to avoid these contamination[7, 24].

The CMB Data Products

The PLA (Planck Legacy Archive) is the highest resolution map, as yet, provided during the full operation of the ESA's (European Space Agency) mission - Planck satellite [2] which released its latest data (Planck2015) products in 2015. But we used the first publicly available Planck data (PLA) which was released in March, 2013, since the resolution of the maps are essentially same, i.e. expansion parameters of spherical harmonics are same at higher as well as lower multipoles. Before this release, the maps with less resolution were provided in series of two years gap from the Wilkinson Microwave Anisotropy Probe (WMAP)[4] - the mission of National Aeronautics and Space Administration (NASA). Both missions provide their own galactic foreground reduced maps, i.e. the Internal Linear Combination (ILC) map of the WMAP [5, 18] and the SMICA [3] map of the Planck mission [19, 31].

1. NASA: LAMBDA Archive and WMAP Mission

The Legacy Archive for Microwave Background Data Analysis (short for LAMBDA) provides the archive data, which are related to the analysis of the Cosmic Microwave Background (CMB) radiation, and the software tools which are useful in their calculations[1, 22, 29].

For some of these bands, i.e. Q, V, and W, foreground reduced versions are available, i.e. the galactic background emission as well as the thermal dust emission[5, 18] were removed from them. The removal procedures are done with help of the calculations and the models which are derived from the other bands, i.e. K and Ka. But we could not accept them as completely free of external foreground contamination.

The ILC map[14] (Figure 1) is produced from a weighted linear combination of smoothed version of the five temperature maps which are formed by coadding full 9 years data. The weights are chosen to maintain the anisotropy of the CMB map while minimizing other contamination sources such as galactic foreground, and thermal dust emission, etc..

The ILC maps is believed to be a good and reliable estimate of the CMB signal on angular scales greater than 10 degrees with negligible instrument noise, over the full sky. But on smaller scales there is a significant structure in the bias correction map that is still uncertain[29].

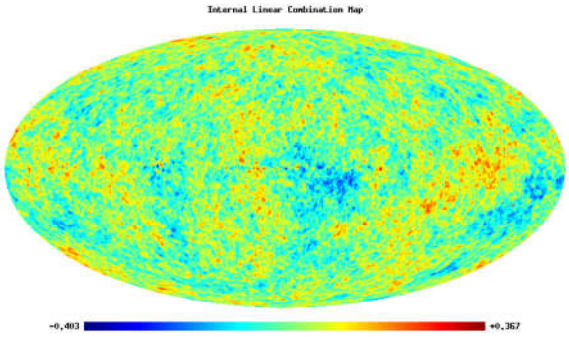

FIG. 1: The Internal Linear Combination map of the WMAP: without any scaling factor and the physical unit of the color bar is in mK

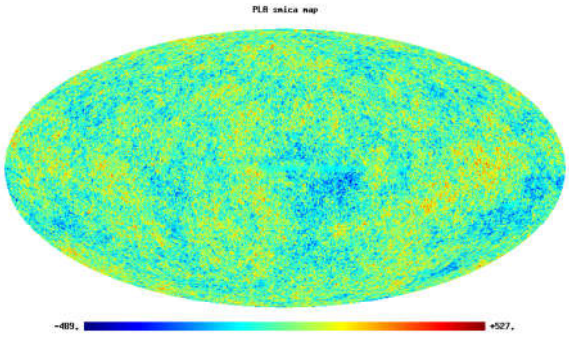

FIG. 2: The foreground reduced product of the Planck Legacy Archive: SMICA. The color bar units is in μK. It has four times finer resolution than ILC.

FIG. 3: *
Reproduce by MAP2GIF facility of Healpix [22] software package.

2. *ESA: Planck Mission*

To emphasize, the Planck (European Space Agency mission) [26] has nine spectrum lines ranging from 35 MHz to 1 THz while the WMAP [4] has five bands of frequencies ranging from 23 GHz to 94 GHz. The foreground reduced maps are made out of combinations of all those different frequency maps and they are the most reliable maps for the analysis of CMB anisotropy in the sense that all the possible external contamination are removed in several methods and procedures [3, 5, 18].

In March 2013, the Planck mission released its public data products (PLA - Planck Legacy Archive), which gives the CMB sky maps of four times higher resolution (compare the Figures 1 and 2) than the WMAP mission maps[9]. Also it produces the temperature intensity and the polarization maps at each different frequency bands. Their comparison with the WMAP frequencies as well as the black-body radiation power density is shown in the Figure 4. PLA frequencies cover both ascending and descending parts of the graph, as well as the frequencies close to the peak of the graph.

The PLA also has its foreground reduced maps, i.e.the SMICA map[3] (Figure 2) similar to the ILC map of the WMAP. We will heavily concentrate on calculations of the data derived from this foreground reduced maps, the SMICA, as well as the ILC maps.

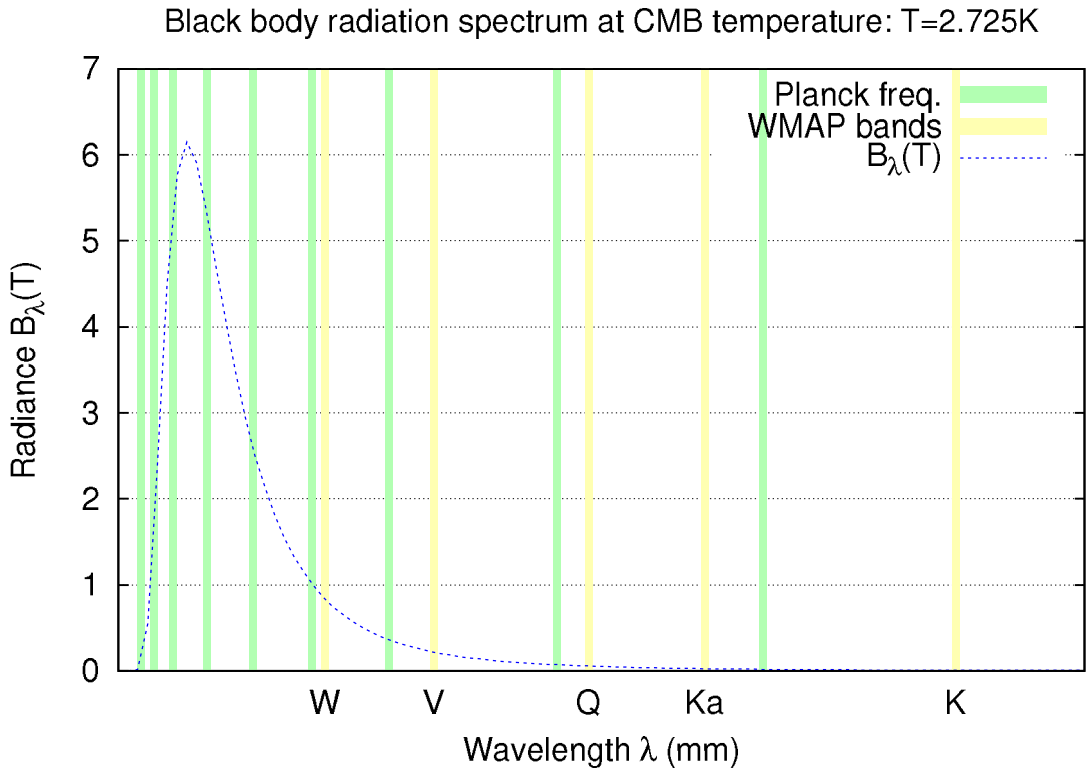

FIG. 4: The Planck frequency bands on the background of the black-body radiation graph at the CMB temperature, $T_{CMB} = 2.725K$.
The dashed blue line draws radiation of the black-body while each green vertical line corresponds to one of the Planck's nine frequency bands, and pink colored lines are of the WMAP's frequencies.

II. MANIPULATING FITS FILE

The name **FITS**[23] is an abbreviation of: Flexible Image Transport System. Its first main usage was interchanging astronomical image data and further developments took place in the late 1970's. Following this, by 1981, a journal[27] describing exact specifications of the format, FITS became the de facto standard of data transfer between astronomers[23]. Since the file format is famous among astronomers, there are several software packages which are developed and provided from NASA[1, 16, 22].

A. HEALPix

The HEALPix is an abbreviation for Hierarchical Equal Area isoLatitude Pixelization of a sphere. This pixelization produces subdivisions of a spherical surface which divided into equal area pixels. The Figure 5 shows the partitioning of a sphere at

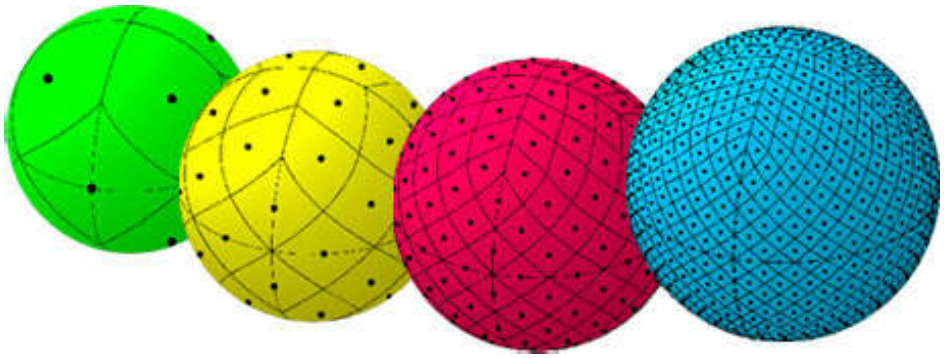

FIG. 5: A simple illustration of how the pixelization of grid lines carried on a sphere in the HEALPix Scheme.
The green sphere is divided into twelve equally sized surfaces which correspond to the lowest possible resolution of the HEALPix, i.e. $\mathrm{N_{res}} = 1$ *and with* $N_{pix} = 12 \cdot 2^{N_{res}}$ *pixels; the other colored (yellow, red, and blue) spheres correspond to HEALPix resolutions of 2, 3, and 4 respectively. On the blue sphere, each pixel covers solid angle of* $7.3°$.[12]

progressively higher resolutions, from left to right.

Another property of the HEALPix grid is that the pixel centers, represented by the black dots in Figure 5, are distributed on discrete number of rings of constant latitude, the number of constant-latitude rings is dependent on the resolution of the HEALPix grid. The formulation is $N_{Lat} = 2^{N_{res}+1} - 1$ which derives from the following recursion relation[12]:

$$N_{Lat(N_{res})} = N_{Lat(N_{res}-1)} + \frac{N_{lat(N_{res}-1)} + 1}{2} 2 = 2N_{lat(N_{res}-1)} + 1$$

Jet Propulsion Laboratory, California Institute of Technology[22], develops a software package which is intended for manipulation, visualization, simulation, and analysis of data stored in HEALPix grid scheme. The most current version of the software is HEALPix 3.00 updated in December 2012. The package has several facilities-subprograms (ALTERALM, ANAFAST, HOTSPOT, MAP2GIF, MEDIAN_FILTER, PLMGEN, SMOOTHING, SYNFAST, and UD_GRADE) for specific tasks and functions. Among them, ANAFAST, MAP2GIF, and SYNFAST are of our interest and use. Since we use them in our analysis of the CMB data; let's have closer look at their details[8, 13]:

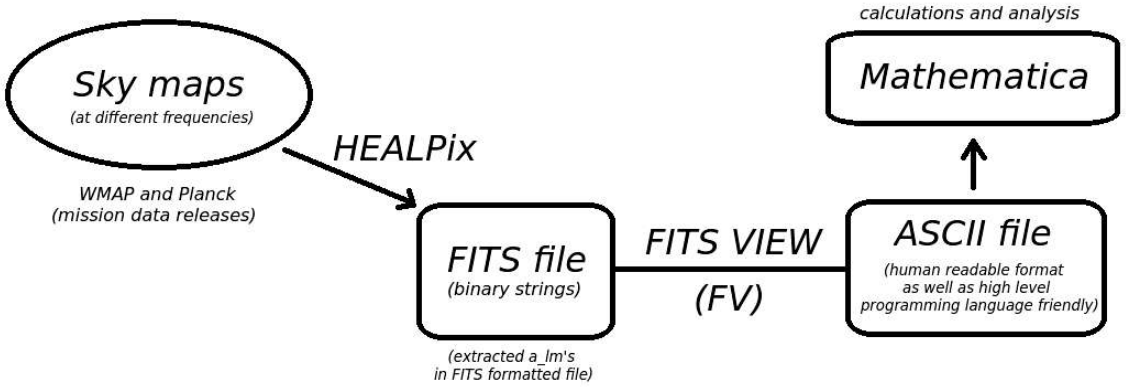

FIG. 6: Block diagram: A brief explanation of how we extract a_{lm}'s in *ASCII* format which are further analyzed in MATHEMATICA codes conveniently.
*First, we compute integrals over the sky map to extract spherical harmonic expansion coefficients, a_{lm}'s, by means of HEALPix facility - ANAFAST[22] which reads and produces FITS formatted files. Then we convert binary data in the newly formed FITS file into ASCII formatted file with help of FV - FITSVIEW[1] software package. New ASCII file is saved as some *.txt file and ready to be read by* MATHEMATICA *codes easily. At last, everything else is carried out in the programming and gives results of the computations.*

B. FITS VIEW

The FV is an acronym for FITS VIEW which is the interactive editor for files formatted in FITS. FV is an easy to use, graphical interface program and capable of viewing, editing, and handling the both images and tables written in the FITS file.

For example, with help of **FITSVIEW**[1], we can extract decimal expressions of the data from any FITS file containing the binary formatted data and save them in a separate file. In this way, we get a new files which are convenient to use in high level programming languages, i.e. MATHEMATICA. A brief explanation of the procedure can be illustrated in a simple block diagram (Figure 6).

III. MATHEMATICAL EXPRESSIONS

Any scalar field on a sphere can be expressed as a series of spherical harmonic multipoles. Since the spherical harmonics form a complete orthonormal basis set of the Hilbert space of square-integrable functions over the 2-sphere. In mathematical

language:

$$f : \mathbb{S}_2 \to \mathbb{C} \quad \Rightarrow \quad f(\theta,\phi) = \sum_{l=0}^{\infty} \sum_{m=-l}^{l} f_{lm} Y_{lm}(\theta,\phi)$$
$$\int_0^{2\pi} \int_0^{\pi} Y_{l_1,m_1}(\theta,\phi)\, Y^*_{l_2,m_2}(\theta,\phi) \sin\theta\, (\mathrm{d}\theta)\, \mathrm{d}\phi = \delta_{m_1,m_2}\delta_{l_1,l_2} \tag{1}$$

Again, indeed the temperature difference on the whole sky is a real function from a two-sphere to a set of real numbers, $\Delta T : \mathbb{S}_2 \to \mathbb{R}$, therefore it can be expanded in the spherical harmonics[6, 17, 21, 25]:

$$\Delta T(\theta,\phi) = \sum_{l=0}^{\infty} \sum_{m=-l}^{l} a_{lm} Y_{lm}(\theta,\phi) \tag{2}$$

Where

$$Y_{lm}(\theta,\phi) = n_{lm} P_l^m(\cos\theta)\, e^{im\phi} \tag{3}$$

with n_{lm} and $P_l^m(\cos\theta)$ are the normalization coefficients and the associated Legendre polynomials respectively. The normalization coefficients are defined in several different way depending on an area of use, i.e. a research field:

$$n_{lm} = \sqrt{\frac{2l+1}{4\pi} \frac{(l-m)!}{(l+m)!}}$$

The coefficients a_{lm} can be calculated by the following formula, which immediately derives from the orthonormality condition (Equation 1).

$$a_{lm} = \int_0^{2\pi} \int_0^{\pi} T(\theta,\phi)\, Y^*_{lm}(\theta,\phi) \sin\theta\, (\mathrm{d}\theta)\, \mathrm{d}\phi$$

This is the equation calculated within the CMB data analysis software packages, i.e. the HEALPix-ANAFAST[13, 22].

Deriving from properties of associated Legendre polynomial, spherical harmonics have the following property:

$$Y_{l,-m} = (-1)^m Y^*_{l,+m} \tag{4}$$

For real functions : $\mathbb{S}_2 \to \mathbb{R}$, there is an especial condition on the expansion coefficients a_{lm} by the Equation 4, so to say "reality condition":

$$a_{l,-m} = (-1)^m a^*_{l,+m} \tag{5}$$

Since the CMB temperature function over the sky is a real function, our randomly generated a_{lm}'s should be constrained by the Equation 5.

The temperature power spectrum or the variance of the CMB is defined by:

$$C_l^T = \langle a_{lm}^{T*} a_{lm}^T \rangle \tag{6}$$

Indeed, the expression $(\Delta T)^2 = \frac{l(l+1)}{2\pi} C_l^T$ is analyzed to estimate the amplitude of the multipole moments.

A. Pseudo Entropies

We are identifying the spherical harmonic multipoles with the quantum mechanical state vectors in the Hilbert space, in which we have a property of the normalization, i.e. $\langle\psi|\psi\rangle = 1$, therefore we need to normalize the spherical harmonic multipoles.

$$\begin{aligned} T_l(\theta,\phi) &\to |\psi\rangle \\ \sum_{m=-l}^{l} a_{lm} Y_{lm}(\theta,\phi) &\to \sum_{m=-l}^{l} a_{lm} |lm\rangle \end{aligned}$$

with the following condition[6]: of the normalization

$$\sum_{m=-l}^{l} |a_{lm}|^2 = 1 \text{ or } \langle\psi|\psi\rangle = 1 \tag{7}$$

This condition won't affect the comparison of the pseudo entropy between the real CMB data and the randomly generated samples since the both of them are normalized. From now on, we use a_{lm}'s for the already normalized coefficients in our notations.

Von Neumann entropy:

$$S(\rho) = -\mathrm{Tr}(\rho \ln \rho) = -\sum_{\lambda \in \mathbb{EV}(\rho)} \lambda \ln \lambda \tag{8}$$

When we encounter values of $\lambda = 0$, we take the zero value $0 = 0 \ln 0$, since in the limiting case we have: $\lim_{x \to 0} x \ln x = 0$. If we have the eigenvalues of $\lambda \in \{1, 0, \ldots, 0\}$, i.e. ρ is the pure density matrix, then this case is of no interest to us. Therefore we need to get a mixed density matrix ρ_{mixed}. There are two methods mixing the pure density matrix with itself, in some sense. We will use both of them in our analysis and calculations.

B. Angular Pseudo Entropy

One way of mixing the density matrix is by means of the angular momentum operators, L_x, L_y, and L_z or L_1, L_2, and L_3[6, 21, 25]:

$$|\psi\rangle\langle\psi| = \rho \to \rho_{mixed} = \frac{1}{l\,(l+1)} \sum_{i=1}^{3} L_i \rho L_i \tag{9}$$

Since the angular momentum operators preserve rotational symmetry, the new mixed density matrix, as well as the entropy are invariant under rotational transformations[6, 25].

If we introduce and use the ladder operators into the Equation 9:

$$L_+ = L_x + iL_y$$
$$L_- = L_x - iL_y$$

which have the following commutation relations:

$$[L_+, L_-] = 2L_z$$
$$[L_z, L_+] = L_+$$
$$[L_z, L_-] = -L_-$$
$$\mathbf{L}^2 = \sum_{i=x,y,z} L_i^2 = L_z^2 + \frac{1}{2} L_+ L_- + \frac{1}{2} L_- L_+$$

then, our mixed entropy is written as the following:

$$\rho_{mixed} = \frac{1}{l\,(l+1)} \left(|\psi_+\rangle\langle\psi_+| + |\psi_-\rangle\langle\psi_-| + |\psi_z\rangle\langle\psi_z| \right) \tag{10}$$

where

$$|\psi_+\rangle = \frac{1}{\sqrt{2}} L_+ |\psi\rangle, \quad |\psi_-\rangle = \frac{1}{\sqrt{2}} L_- |\psi\rangle, \quad \text{and} \quad |\psi_z\rangle = L_z |\psi\rangle$$

The ladder operators have the following relations with their operations on the state vectors:

$$\begin{aligned} L_z|l,m\rangle &= m|l,m\rangle \\ L_+|l,m\rangle &= \sqrt{l\,(l+1) - m\,(m+1)}|l,m+1\rangle \\ L_-|l,m\rangle &= \sqrt{l\,(l+1) - m\,(m-1)}|l,m-1\rangle \end{aligned} \tag{11}$$

By using above expression we can calculate the new mixed density matrix and therefore its entropy (our MATHEMATICA code for the angular pseudo entropy uses these expressions).

C. Projection Pseudo Entropy

The another method of the mixing density matrix is to expand the dimension of the density matrix by tensor multiplying it with a unit matrix and thereafter to project the tensored space into a lower dimensional space. A brief scheme of the procedure is[6, 25]

$$|\psi\rangle\langle\psi| = \rho \to \rho_{mixed} = \frac{2l+1}{2\,(l+j)+1} \underset{l+j}{\mathrm{Pr}} \left(\rho \otimes ((I_j)\right) \underset{l+j}{\mathrm{Pr}}$$

The tensor product on the right hand side can be projected in the higher dimensional space by means of the Clebsch-Gordan decomposition coefficients[6, 21]

$$|l_1, m_1\rangle \otimes |l_2, m_2\rangle = \sum_{l=|m_1+m_2|}^{l_1+l_2} \mathrm{CG}\,(l_1, m_1, l_2, m_2, l, m_1+m_2)\,|l, m\rangle$$

The summation is over the multipole momentum number with the condition to hold the triangle inequality with l_1,and l_2, i.e.:

$$|l_1 - l_2| \le l \le l_1 + l_2$$

$|m_1 + m_2| \le l$ magnetic number should exceed the momentum number

The entropy calculated from the mixed density matrix described above is the "Projection Pseudo Entropy" and it can be written as the following when we insert the Clebsch-Gordan coefficients into the formula:

$$\Pr_{l+j} |l,m\rangle \otimes |j,k\rangle = \sqrt{\frac{\binom{2l}{l+m}\binom{2j}{j+k}}{\binom{2(l+j)}{l+j+m+k}}} |l+j, m+k\rangle \tag{12}$$

The Clebsch-Gordan coefficients vanish except when $m = m_1 + m_2$ and the l_is satisfy the triangle inequality.

D. Gaussianly Distributed Random a_{lm}'s

This is the expression used for generating gaussianly distributed random samples of the spherical harmonic spectral coefficients[21]:

$$c_{lm} = \sqrt{-v \ln x} \exp(2\pi i y) \tag{13}$$

where both x and y are uniformly distributed variables between 0 and 1, i.e. $x, y \in (0, 1]$. If we calculate a variation of these random data:

$$\mathrm{Var}(c_{lm}) = \langle |c_{lm}|^2 \rangle - |\langle c_{lm} \rangle|^2 = \langle |c_{lm}|^2 \rangle = \int_0^1 -v \ln x \mathrm{d}x = v$$

since

$$\langle c_{lm} \rangle = \int c_{lm} \mathrm{d}P(c_{lm}) = \int c_{lm}(x,y)\, \mathrm{d}P(x,y) = \\ = \int_0^1 \int_0^1 \sqrt{-v \ln x} \exp(2\pi i y)\, \mathrm{d}x \mathrm{d}y = 0$$

and the integral of $\exp(2\pi i y)$ from 0 to 1 is zero. Also

$$|c_{lm}| = |\sqrt{-v \ln x} \exp(2\pi i y)| = |\sqrt{-v \ln x}||\exp(2\pi i y)| = \sqrt{-v \ln x}$$

since $|e^{i\alpha}| = 1$ for $\forall \alpha \in \mathbb{R}$. This implies that the variance of the random variable is only dependent of one parameter: v. Therefore, we can choose an arbitrary v for our

need or convenience later when writing the MATHEMATICA codes.

IV. COMPUTATIONAL RESULTS

In this section we illustrate the graphs and the figures which are results of the computation of the above mentioned mathematical setups. To emphasize in advance, the WMAP and the PLA are the two independent data source for the CMB radiation analysis. Therefore we try to compare the two data sets whenever we encounter an issue or an analysis related to the their consistency.

We particularly investigates the entropy value difference between the foreground reduced maps of the WMAP and the PLA (Figures 1 and 2). The resolution comparison of the two maps could be seen easily: the latter (bottom) map contains four times more information than the former (above) one. The both ILC and SMICA show relatively similar plots, see the Figure 7:

Since the two maps are independent of each other and, their foreground reduction methods and algorithms are different, thus the numerical values of the pseudo angular entropy are not exactly same.

On the graphs (Figure 7) confidence interval of 68% and 95% of percentage as well as mean and median of randomly generated data sets which follows Gaussian distribution are drawn. The above graph is for comparison of WMAP with random data sets while the bottom graph is for comparison of PLA map.

Key observation of these graphical representation is that at multipoles $l = 5,\ 16,\ 28,\ 30$; entropy values of both WMAP (ILC) and PLA (SMICA) map lie outside of envelope curve of 95% confidence interval which is produced with the Gaussianly distributed random data set. Our main motivation was to find such anomalies of entropy values at higher multipoles.

V. SUMMARY OF RESULTS

Our calculation of the pseudo entropy of the WMAP 9 year maps showed anomalies at low multipoles, i.e. large angular scales. Particularly $l = 5,\ 16,\ 28$ and 30 are of our interest having extremely unlikely pseudo entropy relative to the Gaussian random and statistically isotropic data. We checked numerically the rotational invariance of the formulation of the pseudo entropy and confirmed it. With the capability of

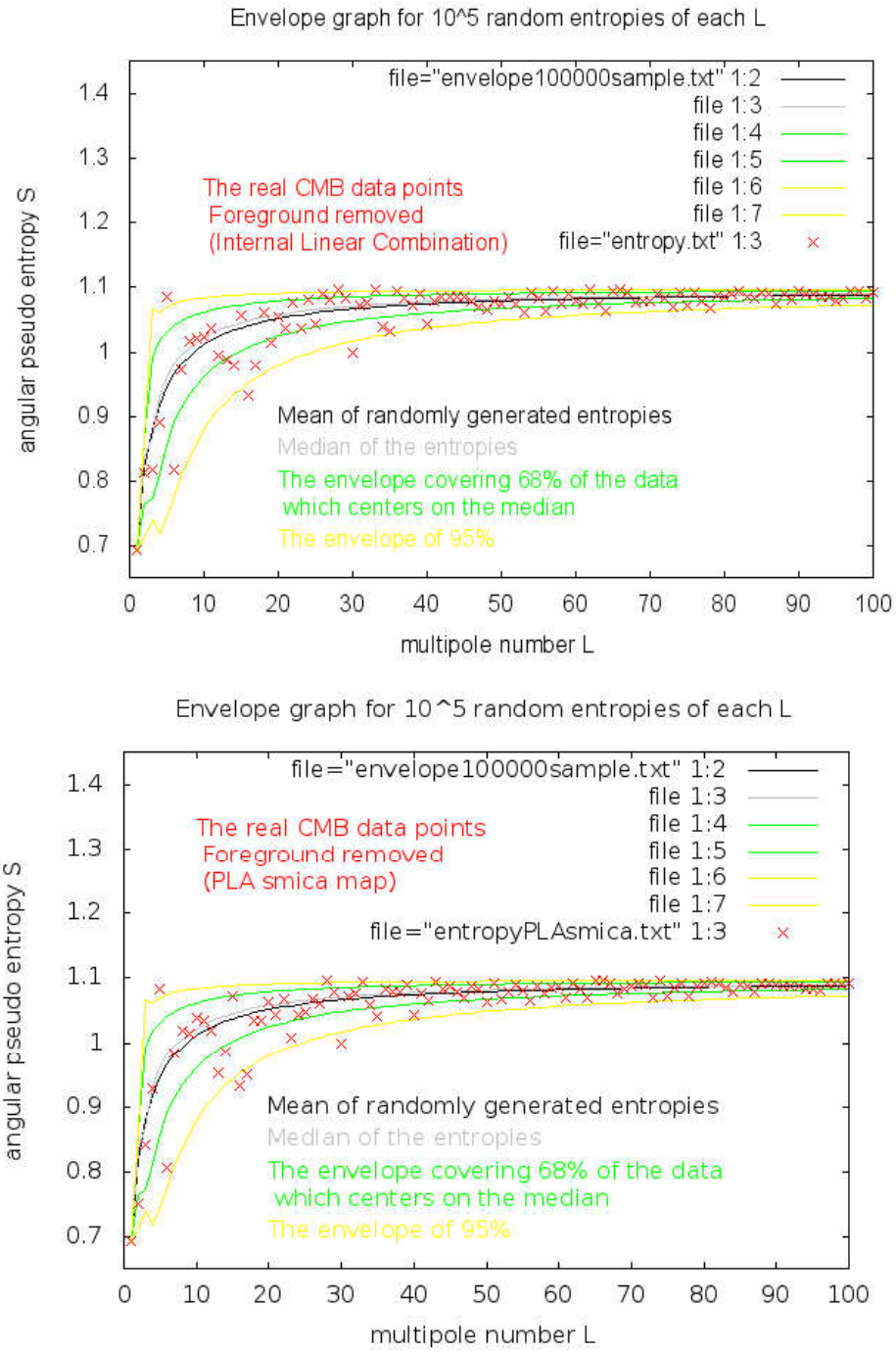

FIG. 7: The first plot: foreground reduced WMAP product - ILC map, with its angular pseudo entropy contrasted on the envelope borders of confidence interval. The second plot: is of PLA foreground reduced map - SMICA.

generating large number of sample data in short time, we combined the PDFs (Probability Distribution Functions) into a single graph - the Confidence Interval Envelope Graph which makes our further analysis more valuable.

We expanded our data source with the Planck satellite data after it released its

first 18 months' observational data. We found that our interested multipoles still show the same qualitative characteristic in the Planck data. But we observed that the pseudo entropy comparison between the WMAP and Planck data were fairly different at higher multipoles. Besides that we used the spherical cut method for removing the galactic background. Also we introduced a new method to eliminate foreground contamination. This gives the result that the foreground reduction process may have affected the entropy values to be shifted upward, i.e. by increasing the values. By reproducing the interpolated graphs of the pseudo entropy, the visual comparison between two or more sets of data becomes very effective, e.g. when comparing the ILC and the SMICA maps[14].

The new method, which actually removes the foreground by means of masking with the given mask files, takes relatively long time on the calculation, therefore we've managed to create PDFs at only few multipole numbers, $l = 5, 6, \ldots, 10$. Even if it requires long computational time, such a procedure that of masking the sky map in real space by means of one of the HEALPix facilities, then analyzing its power spectra is almost impossible when dealing with large number of data sets. Therefore, the new methods is a new fast gateway to do both the masking and the analysis of the sky map at once.

---

[1] FITS VIEW graphical software. `http://heasarc.gsfc.nasa.gov/docs/software/ftools/fv/`. for handling FITS formatted data.

[2] *PLANCK The Scientific Programme*, ESA-SCI(2005)1 edition.

[3] P.A.R. Ade et al. Planck 2013 results. I. Overview of products and scientific results. 2013.

[4] C.L. Bennett et al. The Microwave Anisotropy Probe (MAP) mission. *Astrophys.J.*, 583:1–23, 2003.

[5] C.L. Bennett, D. Larson, J.L. Weiland, N. Jarosik, G. Hinshaw, et al. Nine-Year Wilkinson Microwave Anisotropy Probe (WMAP) Observations: Final Maps and Results. 2012.

[6] Valentin Buciumas. Quantum measures of randomness on the 2-sphere. Bachelor's thesis, Jacobs University Bremen, May 2010.

[7] Craig J. Copi, Dragan Huterer, Dominik J. Schwarz, and Glenn D. Starkman. Bias in low-multipole CMB reconstructions. 2011.

[8] Benjamin D. Wandelt Krzysztof M. Górski Anthony J. Banday Martin Reinecke

Eric Hivon, Frode K. Hansen. Healpix stand-alone facilities. http://healpix.sourceforge.net/documentation.php, Nov 2012.

[9] ESA. Planck legacy archive (PLA). http://www.sciops.esa.int/index.php?project=PLANCK, March 2013.

[10] D. J. Fixsen. The Temperature of the Cosmic Microwave Background. 707:916–920, December 2009.

[11] D. J. Fixsen, E. S. Cheng, J. M. Gales, J. C. Mather, R. A. Shafer, and E. L. Wright. The Cosmic Microwave Background Spectrum from the Full COBE FIRAS Data Set. 473:576, December 1996.

[12] K. M. Górski, E. Hivon, A. J. Banday, B. D. Wandelt, F. K. Hansen, M. Reinecke, and M. Bartelmann. HEALPix: A Framework for High-Resolution Discretization and Fast Analysis of Data Distributed on the Sphere. 622:759–771, April 2005.

[13] K.M. Gorski et al. Healpix - comprehensive documentation. http://healpix.sourceforge.net/.

[14] M. R. Greason et al. Wilkinson microwave anisotropy probe (wmap): Nineyear explanatory supplement, December 2012.

[15] Zong-Kuan Guo, Dominik J. Schwarz, and Yuan-Zhong Zhang. Reconstruction of the primordial power spectrum from CMB data. *JCAP*, 1108:031, 2011.

[16] NASA's HEASARC. Software packages for FITS file. http://heasarc.gsfc.nasa.gov/docs/software.html.

[17] Robert C. Helling, Peter Schupp, and Tiberiu Tesileanu. CMB statistical anisotropy, multipole vectors and the influence of the dipole. *Phys.Rev.*, D74:063004, 2006.

[18] G. Hinshaw, D. Larson, E. Komatsu, D.N. Spergel, C.L. Bennett, et al. Nine-Year Wilkinson Microwave Anisotropy Probe (WMAP) Observations: Cosmological Parameter Results. 2012.

[19] S. M. Leach, J.-F. Cardoso, C. Baccigalupi, R. B. Barreiro, M. Betoule, J. Bobin, A. Bonaldi, J. Delabrouille, G. de Zotti, C. Dickinson, H. K. Eriksen, J. Gonzlez-Nuevo, F. K. Hansen, D. Herranz, M. Le Jeune, M. Lpez-Caniego, E. Martnez-Gonzlez, M. Massardi, J.-B. Melin, M.-A. Miville-Deschnes, G. Patanchon, S. Prunet, S. Ricciardi, E. Salerno, J. L. Sanz, J.-L. Starck, F. Stivoli, V. Stolyarov, R. Stompor, and P. Vielva. Component separation methods for the planck mission. *A&A*, 491:597–615, nov 2008.

[20] J. C. Mather, E. S. Cheng, D. A. Cottingham, R. E. Eplee, Jr., D. J. Fixsen, T. Hewagama, R. B. Isaacman, K. A. Jensen, S. S. Meyer, P. D. Noerdlinger, S. M. Read, L. P. Rosen, R. A. Shafer, E. L. Wright, C. L. Bennett, N. W. Boggess, M. G. Hauser, T. Kelsall, S. H. Moseley, Jr., R. F. Silverberg, G. F. Smoot, R. Weiss, and D. T. Wilkinson. Measurement of the cosmic microwave background spectrum by the

COBE FIRAS instrument. 420:439–444, January 1994.

[21] Momchil Minkov. Probing the statistical isotropy of the CMB. Bachelor's thesis, Jacobs University Bremen, May 2010.

[22] NASA. Healpix software package. `http://healpix.jpl.nasa.gov/`. for Analysis of CMB data in FITS format.

[23] NASA. IAU FITS working group. `http://fits.gsfc.nasa.gov/iaufwg/iaufwg.html`.

[24] Devdeep Sarkar, Dragan Huterer, Craig J. Copi, Glenn D. Starkman, and Dominik J. Schwarz. Missing Power vs low-l Alignments in the Cosmic Microwave Background: No Correlation in the Standard Cosmological Model. *Astropart.Phys.*, 34:591–594, 2011.

[25] Peter Schupp. Unpublished work. Private communications.

[26] Tauber, J. A. et al. Planck pre-launch status: The planck mission. *A&A*, 520:A1, 2010.

[27] E. W.; Harten R. H. Wells, D. C.; Greisen. FITS - a flexible image transport system. *Astronomy and Astrophysics Supplement*, 44:363, 6 1981.

[28] M. White, editor. *Anisotropies in the CMB*, 1999.

[29] LAMBDA WMAP. Nine years mission data. `http://lambda.gsfc.nasa.gov/product/map/dr5/m_products.cfm`, June 2012.

[30] E. L. Wright, J. C. Mather, D. J. Fixsen, A. Kogut, R. A. Shafer, C. L. Bennett, N. W. Boggess, E. S. Cheng, R. F. Silverberg, G. F. Smoot, and R. Weiss. Interpretation of the COBE FIRAS CMBR spectrum. 420:450–456, January 1994.

[31] Planck Collaboration XII. Planck 2013 results: Component separation. *arxiv.org*, 2013.

Theoretical investigation of the piezoelectric effect in Berlinite

N. Tuvjargal* and J. Davaasambuu
Department of Physics, School of Arts & Sciences,
National University of Mongolia, University Street-1, 210646 Ulaanbaatar, Mongolia

U. Pietsch
Department of Physics, University of Siegen,
Emmy-Noether-Campus, Walter-Flex-Str.3, 57072 Siegen, Germany

We report on the atomistic origin of the piezoelectric effect in $AlPO_4$ by means of theoretical investigations in framework of density functional theory using the CRYSTAL14 code. The elastic and piezoelectric properties of Berlinite are related to their AlO_4 and PO_4 tetrahedral units, especially the Al-O-P bridging angle and the strength of the Al-O and P-O bonding. The calculation show that the Al-O bond clearly is of ionic nature but displays a small bond change density between next neighbors only. Under influence of an external field the changes of the P-O bond lengths and the tetrahedral O-Al-O angles are one order of magnitude smaller than those of the Al-O bond lengths and Al-O-P angles between neighboring tetrahedra. Since all changes of bond lengths are small, the atomic origin of the piezoelectric effect mainly can be described by a rotation of slightly deformed AlO_4 tetrahedra against the PO_4 ones.

I. INTRODUCTION

α-quartz is a well-known piezoelectric crystal. MPO_4 (M=Al, Ga, Fe) quartz type compounds have been widely studied due to their large amount of some physical coefficients[1, 2]. The interaction between a crystal lattice and an external electric field is the basis of many fundamental physical phenomena, such as piezoelectricity inducing a change of unit cell parameters and polarization. Although most of these phenomena are well described and understood on a macroscopic level, relatively little is known about the underlying atomic processes. Low quartz $\alpha - SiO_4$, trigonal, space

*Electronic address: tuvjargal@num.edu.mn

group $P3_121$ or $P3_221$ is a well-investigated crystal and widely used for technical applications. $AlPO_4$ has the same crystal symmetry as low quartz. Compared to SiO_4 the unit cell of $AlPO_4$ is twice as large in c direction. Its unit cell can be derived from SiO_4 by an alternating replacement of the Si sites by Al and P atoms. In literature, the explanation of the piezoelectricity in quartz often follows the model introduced by Meissner [3]. He proposed a displacement of the Si_{4+} and O_{2-} ionic sublattices against the external field originating a change in the lattice parameter. This ionic model is not realistic because the Si-O bonds in SiO_4 are partially covalent in nature. Meanwhile one knows that the Si-O bond in quartz is not purely ionic, it also contains covalent contributions[4, 5]. D'Amour et al. [6] have investigated the high pressure dependence of the structure and found that the individual Si-O bond lengths and the O-Si-O bond angles changed very little at high external pressure. The main effect is the change in Si-O-Si angles and O-O distances between the different tetrahedra. Generally, one can suppose that the bond angles between the tetrahedra change more than the Si-O bond lengths under influence of any external perturbation.

It is well known, that the coordinates of atoms within the unit cell can be reconstructed from X-ray diffraction data. By measuring the electric field induced changes of integrated intensities of Bragg reflections one can investigate the origin of the inverse piezoelectric effect in a crystal. The influence of a high electric field on the Bragg reflections has been studied in a number of works [7]. In some cases they might be caused by extinction effects and not by the electrostriction because the field may create structural defects and subsequently causes a change from the dynamical into the kinematic regime of X-ray diffraction. As shown in previous experiments [8] the electric field of about $E < 3\text{kV/mm}$ alters the integrated intensity of Bragg reflections in the order of 1% only. Therefore the combination of an X-ray diffraction experiment with the electric field modulation technique is suitable for these studies because of the eliminations of experimental fluctuations. Generally, the modulation technique is useful for the evaluation of very small physical effects with high accuracy. We have applied this method for studying the inverse piezoelectric effect in $AlPO_4$. For the first time this experiment also was performed at low temperatures[9].

The purpose of the present work is to investigate the atomistic origin of the piezoelectric effect in $AlPO_4$ together with structural, elastic and piezoelectric properties of the crystal by means of density functional theory (DFT) using the CRYSTAL14 code and experimental data[10].

II. THEORETICAL BACKGROUND

Calculations were performed with a standard version of the ab-initio code CRYSTAL14 [11]. Atomic orbitals used for this study are Gaussian type functions (GTO), where each GTO is the product of Gaussian functions multiplied by a real solid spherical harmonic. Further we used the B3LYP (Becke's three-parameter exchange function[12] and the nonlocal Lee-Yang-Parr correlation function[13])to form the Hamiltonian. Several properties of crystalline materials can be computed by considering strained configurations of the structure: elastic and piezoelectric tensors, for instance. The elastic constants C_{ij} are related to the second derivatives of the ground state energy calculated with respect to a certain strain component as follows:

$$C_{ij} = \frac{1}{V_0}\left[\frac{\partial^2 E}{\partial\eta_i \partial\eta_j}\right]_0. \tag{1}$$

where V_0 is the unit cell volume, η is the rank-2 symmetric tensor of pure strain and elastic tensor has been written as a rank-2 66 tensor. This tensor is symmetric so that it has a maximum of 21 independent elements. A Taylor expansion of the unit-cell energy to second order in the strain components yields:

$$E(\eta) = E(0) + \sum_{i=1}^{6}\left[\frac{\partial E}{\partial\eta_i}\right]_0 \eta_i + \frac{1}{2}\sum_{i=1}^{6}\left[\frac{\partial^2 E}{\partial\eta_i \partial\eta_j}\right]_0 \eta_i\eta_j \tag{2}$$

has been considered for the calculation of the elastic constants. The strain η is described by the relative difference of the actual lattice parameter and its value and minimum energy. $E(0)$ stands for the energy of the equilibrium configuration and η_i refers to the strain components expressed according to Voigt's notation ($i = 1, 6$). The second derivatives of ground state energies are evaluated numerically.

In Crystal14 code the polarization can be computed either via localized Wannier functions or via the Berry phase (BP) approach. For our computation we used the BP approach where the piezoelectric constants can be written in terms of numerical first derivatives of the BP φ_l with respect to the strain:

$$e_{iv} = \frac{|e|}{2\pi V} \sum_{l} a_{li} \frac{\partial \varphi_l}{\partial \eta_v}, \tag{3}$$

where a_{li} is the i-th Cartesian component of the l-th direct lattice basis vector a_l. A simple direct connection exists between direct **e** and converse **d** piezoelectric tensors:

$$e = d \times C, \qquad d = e \times S. \tag{4}$$

where C is the fourth rank elastic tensor of second derivatives of energy with respect to pairs of deformations and $S = C^{-1}$ is the fourth rank compliance tensor[17].

As for the computation of the piezoelectric tensor, Eleven η_i strain values in the interval between [0.020 and+0.020] were considered for the fitting. For each value of η_i the three Berry's phase components φ_1, φ_2 and φ_3 are computed, corresponding to the phase differences of the state with and without strain in the three directions of the space (x, y, and z, respectively). Because of the uniaxial strain the symmetry of the unit cell becomes reduced and additional degrees of freedom have to be considered for numerical analysis[15].

III. RESULTS AND DISCUSSION

The charge density distribution of the unstrained (cubic) ground state was examined first in order to characterize the character of the different bonds within the unit cell. The ground-state electron charge density is an observable of primary importance. The total electron density maps provide a pictorial representation of the total electronic distribution. However, more useful information is obtained by considering difference maps, given as a difference between the calculated total electron density and any "reference" electron density. In present case the "reference" density is a superposition of charge distributions of isolated atoms. Difference electronic charge density can be expressed as follows:

$$\Delta\rho(\overrightarrow{r}) = \rho_t(\overrightarrow{r}) - \rho_s(\overrightarrow{r}), \tag{5}$$

where $\rho_t(\overrightarrow{r})$ is crystal electron density and $\rho_s(\overrightarrow{r})$ is "reference" electron density. FIG.1 displays the difference densities in the vicinity of the Al and P atoms in a) plane of O-Al-O bond, b) plane of O-P-O bond. Contours are given in steps of $\Delta\rho(r) = 0.002$

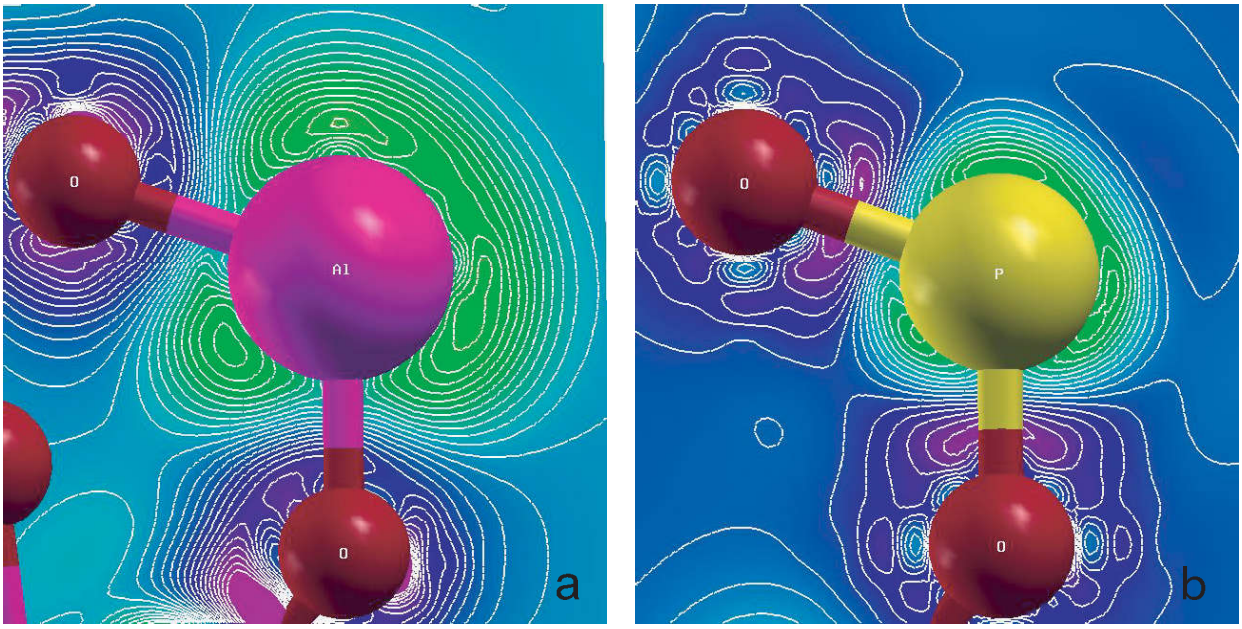

FIG. 1: *Difference electronic charge density distribution in a) plane of O-Al-O bond, b) plane of O-P-O bond*

$e/\mathring{A}^3$. Following these contours the origin of chemical bonds between the atoms can be classified based on charge density distribution between two neighbored atoms. The O-Al bond has little bond charge density between the atoms with maximum close to Al which explains the partially ionic character of the bond. On the other hand the O-P bond is more covalent in nature than the Al-O bond visible by a much larger bond charge between the phosphorous and oxygen atoms.

It is possible to have interatomic bonds that are partially ionic and partially covalent, and, in fact, only a very few compounds exhibit pure ionic or covalent bonding. For a given compound, the degree of either bond type depends on the difference in their electronegativities. The percent ionic character (%IC) of bond between element A and B may be approximated by the expression

$$\%IC = \{1 - \exp\left[-(0.25)(X_A - X_B)^2\right]\} \times 100 \tag{6}$$

where X_A and X_B are electronegativities for respective elements. Using Pauling electronegativity scale [14], we can obtain the percent ionic character (%IC) of the

bonding between the atoms in $AlPO_4$. The crystal contains P (electronegativity value = 2.19), Al (1.61) and O (3.44). Accordingly, the ionic character of the P-O bond is 32.33% and Al-O bond are 56.7% due to the bonds between P-O are more covalent whereas the bonds between Al-O are more ionic in character.

The berlinite ($AlPO_4$) crystal structure belongs to the trigonal space group $P3_121$ (or $P3_221$), there are six nonvanishing independent components of the elastic tensor, namely, C_{11}, C_{12}, C_{13}, C_{14}, C_{33}, and C_{44}.

This leads to an elastic tensor, written using the Voigt's contracted notation, containing the six independent elastic constants,

$$C_{ij} = \begin{bmatrix} C_{11} & C_{12} & C_{13} & 0 & C_{15} & 0 \\ 0 & C_{11} & C_{13} & 0 & -C_{15} & 0 \\ 0 & 0 & C_{33} & 0 & 0 & 0 \\ 0 & 0 & 0 & C_{44} & 0 & C_{15} \\ 0 & 0 & 0 & 0 & C_{44} & 0 \\ 0 & 0 & 0 & 0 & 0 & C_{66} \end{bmatrix}.$$

For trigonal and hexagonal systems, C_{66} elastic constant can be computed from the C_{11} and C_{12} values using by $C_{66} = (C_{11} - C_{12})/2$. To compute the complete elastic tensor of $AlPO_4$, the three different strain values η_1, η_3 and η_4 have to be applied, where $\eta_1 = \epsilon_{11}$, $\eta_3 = \epsilon_{33}$ and $\eta_4 = 1/2(\epsilon_{23} + \epsilon_{32})$. Here ϵ_{ij} are the components of strain tensor. Each deformation allows for the evaluation of all tensor components of the corresponding elastic constants, due to the calculation of the analytical energy gradients. For each of the considered strains the elastic constants have been calculated. In order to compute the independent constants the necessary strains are automatically selected by the program after a symmetry analysis of the crystal. Considering eq.1 the computed values (in GPa) of the six independent elastic constants for the Berlinite are shown in Table.I together with some experimental values.

Our computed values of elastic constants are in good agreement with other theoretical values. Also few of our elastic constants are in good agreement with experimental data. Because of the well know difficulties in the experimental determination of elastic constants, different values of experimental parameters have been reported [18, 20] which , in few cases, are smaller than the theoretical data. In quartz type compounds,

TABLE I: Theoretical and experimental values (in GPa) of elastic constants of Berlinite.

C_{ij}	Our	Theory[15]	Experimental[18]
C_{11}	84.13	87.9	64.0
C_{33}	113.41	122.4	85.8
C_{44}	46.70	43.3	43.2
C_{12}	22.67	27.1	7.2
C_{13}	25.52	30.4	9.6
C_{14}	-10.28	-11.2	-12.4
C_{66}	30.72	30.4	28.4

only two independent constants of the piezoelectric tensor are non-zero. Therefore the piezoelectric tensor can be written as

$$e_{ij} = \begin{bmatrix} e_{11} & -e_{11} & 0 & e_{14} & 0 & 0 \\ 0 & 0 & 0 & 0 & -e_{14} & -2e_{11} \\ 0 & 0 & 0 & 0 & 0 & 0 \end{bmatrix}.$$

Using the Barry phase method the computed values of direct and inverse piezoelectric coefficients in $AlPO_4$ are shown in table.II.

TABLE II: Theoretical end experimental values of direct (in C/m^2) and inverse (in pm/V) piezoelectric coefficients in $AlPO_4$

	Our	Theory [16]	Experimental [19]
e_{11}	0.182	0.208	0.22
e_{14}	-0.05	-0.16	-0.15
d_{11}	0.301	0.30	0.365[9]
d_{14}	0.248	1.62	

These results in good agreement with theoretical and experimental data.

Considering the three strain components η_1, η_3 and η_4 we evaluated changes of bond lengths and bond angels. The results are displayed in fig.2, fig.3 and fig.4. It turns out that the changes of the P-O bond lengths are always close to zero and changes of the Al-O bond lengths are of the order of 0.57%. This is related to the different strength of Al-O and P-O bonds, because, the O-Al bond is mainly of ionic character but the O-P bond is of more covalent nature. On the other hand the

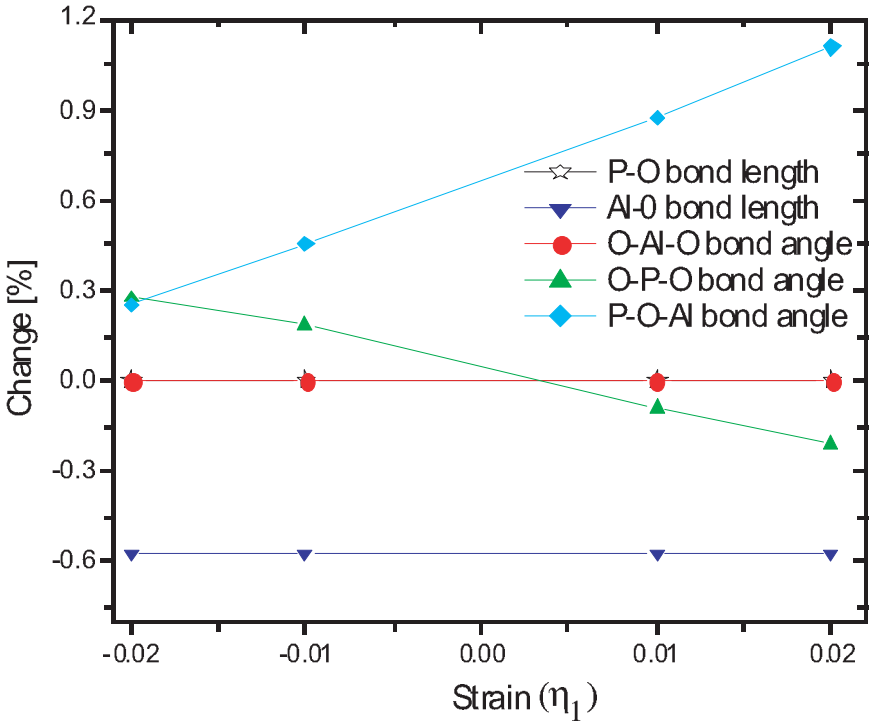

FIG. 2: *Evolution of bond length and bonds angle in $AlPO_4$ under application of η_1 strain.*

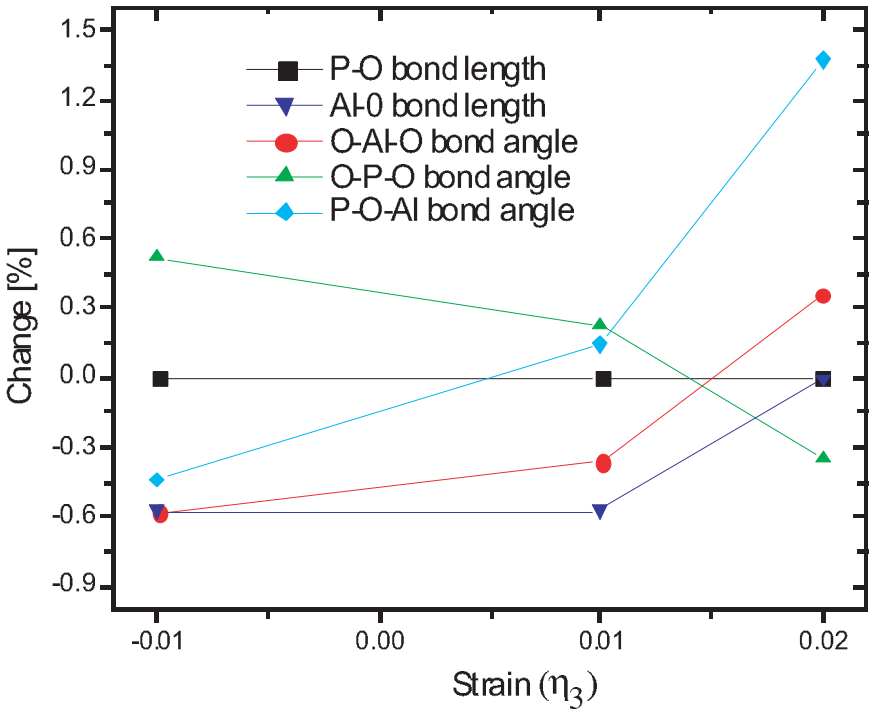

FIG. 3: *Evolution of bond length and bonds angle in $AlPO_4$ under application of η_3 strain.*

change of O-P-O bonding angles are larger compared to the changes of O-Al-O one.

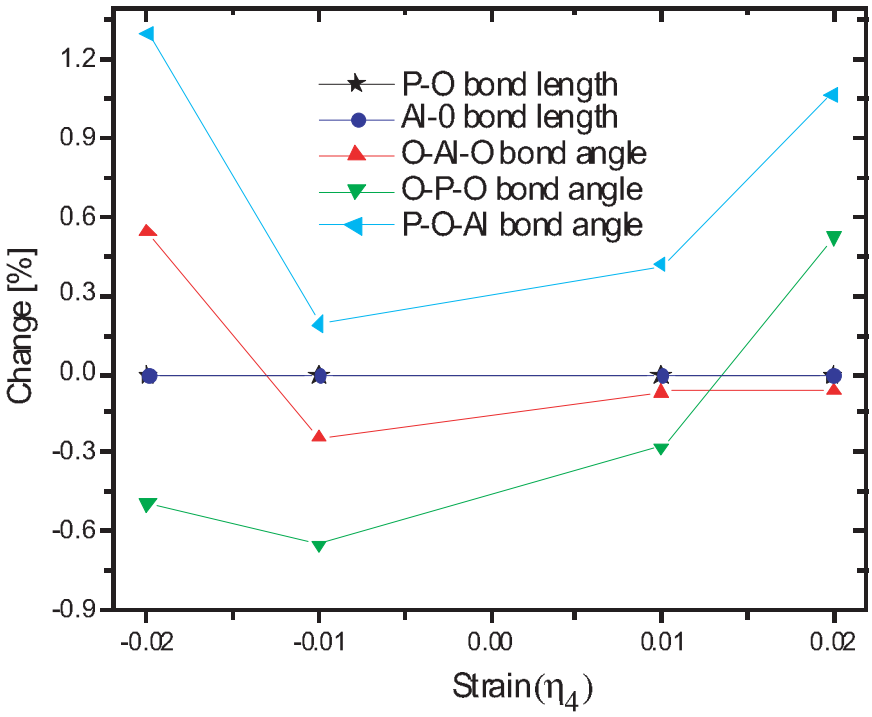

FIG. 4: *Evolution of bond length and bonds angle in $AlPO_4$ under application of η_4 strain.*

The change of Al-O-P bonding angles of individual PO_4 and AlO_4 tetrahedral are between 0.2% and 1.9%. PO_4 and AlO_4 tetrahedral distortions can be closely related to the Al-O-P angle and Al-O and P-O bonding type. Therefore the atomic origin of the piezoelectric effect in $AlPO_4$ can be described by geometrical characteristics of PO_4 and AlO_4 tetrahedral units.

IV. CONCLUSION

We have summarized the elastic and piezoelectric properties of Berlinite. The elastic and piezoelectric properties of $AlPO_4$ are related to their AlO_4 and PO_4 tetrahedral units, especially the Al-O-P bridging angle and Al-O and P-O bonding type. From charge density difference maps and considering the percentage of ionic character (%IC) of the different bonds we have obtained that the O-Al bond has little charge density between the aluminum and oxygen atoms only, but the O-P bond has a much larger bond charge between the phosphorous and oxygen atoms and the ionic character of the P-O bond is 32.33% and Al-O bond are 56.7%. Therefore the P-O bonds are more covalent whereas the bonds between Al-O are more of ionic character. Consid-

ering eq.1 and using the Barry phase method we computed the elastic constants and the direct and inverse piezoelectric coefficients of Berlinite. The obtained data are in good agreement with theoretical and experimental results published in literature.

Acknowledgments

This work has been done with financial support of after Ph.D innovation project Pdoc07/2014 of Ministry of Education, Culture and Sciences in Mongolia.

[1] K. Kosten and H. Arnol., Z. Kristallogr. 152, 119 (1980).

[2] H. Ribes, J. C. Giuntini, A. Goiffon, and E. Philippot., Eur. J. Solid State Inorg. Chem. 25, 201 (1988).

[3] A. Meissner. Z. techn. Phys. **2**, 74 (1927).

[4] G.V. Gibbs K.M, Rosso, Teter D.M, Jr.M.B. Boisen and M.S.T.Bukowinski J. Mol. Struct. **13**, 485-486 (1999).

[5] R.A. Young and B. Post, Acta Cryst. **15**, 337 (1962).

[6] H. D'Amour, W. Denner and H. Schultz, Acta Cryst. **B35**, 550 (1979).

[7] U.Pietsch, J. Stahn, J.Davaasambuu, A.Pucher J. Phys. Chem. Sol. **62**, 2129 (2001).

[8] J.Davaasambuu, A.Pucher, V.Kochin and U.Pietsch . Europhys. Lett. **62(6)**, 834-840 (2003).

[9] N.Tuvjargal, J.Davaasambuu, et, al HASYLAB/DESY annual report in Germany, (2004).

[10] J. Davaasambuu, N.Tuvjargal, B.Burmaa and U.Pietsch, Physics Journal, National University of Mongolia 251 PHYSICS **(13)**, 78-83 (2005).

[11] R. Dovesi, R. Orlando, A. Erba, C. M. Zicovich-Wilson, B. Civalleri, S. Casassa, L. Maschio, M. Ferrabone, M. De La Pierre, P. DArco, Y. Noel, M. Causa, M. Rerat, B. Kirtman. Int. J. Quantum Chem. 114, 1287 (2014).

[12] A. D. Becke ., J. Chem. Phys. 98, 5648 (1993).

[13] C. Lee, W. Yang, and R. G. Parr ., Phys. Rev. B 37, 785 (1988).

[14] Pauling, L ., Nature of the Chemical Bond. Cornell University Press. pp. 88107. ISBN 0-8014-0333-2.

[15] P. Labequerie, M. Harb, et.al., PHYS. REV. B. **81**, 045107 (2010)

[16] E. Philippot, D.Palmier, et.al., Journal of Solid State Chemistry. **123**, 1-13 (1996)

[17] R. Dovesi, V. R. Saunders, C. Roetti, R. Orlando, C. M. Zicovich-Wilson, F. Pascale,

B. Civalleri, K. Doll, N. M. Harrison, I. J. Bush, P. DArco, M. Llunell, M. Caus and Y. Noll., CRYSTAL14 User's Manual (University of Torino, Torino, 2014).

[18] Z. P. Chang., IEEE Trans. Sonics Ultrason. SU-23, 127 (1976)

[19] 65H. Wang, B. Xu, X. Liu, J. Han, S. Shan, and H. Li, J., Cryst.Growth **79**, 227 (1986).

[20] H.A.A.Sedik, G.A.Saunders, et.al., PHYS. REV. B. **36**, 7612 (1987)